Investigations on the electron bunch distribution in the longitudinal phase space at a laser driven RF electron source for the European X-FEL

Dissertation

zur Erlangung des Doktorgrades

des Department Physik

der Universität Hamburg

vorgelegt von

Juliane Rönsch

aus Berlin

Hamburg

2009

Gutachter der Dissertation:	Prof. Dr. Jörg Rossbach PD Dr. Bernhard Schmidt
Gutachter der Disputation:	Prof. Dr. Jörg Rossbach Dr. Siegfried Schreiber
Datum der Disputation:	27. Mai 2009
Vorsitzende des Prüfungsausschusses:	Prof. Dr. Caren Hagner
Vorsitzender des Promotionsausschusses:	Prof. Dr. Robert Klanner
Leiter des Departments Physik:	Prof. Dr. Joachim Bartels
Dekan der MIN-Fakultät:	Prof. Dr. Heinrich Graener

Abstract

The Photoinjector Test facility at DESY, Zeuthen site, (PITZ) is aiming for the optimization of electron guns for SASE-FELs. For this it is necessary to investigate the characteristics of the six dimensional phase space of the bunch produced by a photoinjector. This thesis is focused on the analysis of the longitudinal properties of the electron bunch distribution, this means the temporal current distribution and the momentum distribution as well as the correlation of both properties. The complete distribution of the electron bunch in longitudinal phase space of a photoinjector was measured directly for the first time at a beam momentum of about 5 MeV/c, using an existing apparatus. This system had been designed for an accelerating gradient of 40 MV/m. Its subcomponents were analysed to understand sources of uncertainties of the measurement system. The usage of higher accelerating gradients in the gun (60 MV/m, resulting in a beam momentum of about 6.8 MeV/c) demands major modifications of the existing measurement system for the longitudinal phase space distribution. An upgrade of the facility by an additional accelerating cavity required the design of further longitudinal diagnostics systems for the analysis at higher momenta (up to 40 MeV/c). Measurements of the longitudinal beam properties to determine the influence of different operation parameters, like RF launch phase, charge, accelerating field gradient and laser distribution were performed and compared to simulations.

Kurzdarstellung

Ziel des Photoinjector Teststandes am DESY, Standort Zeuthen, (PITZ) ist die Optimierung von Elektronenquellen für SASE-FELs. Dafür müssen die Merkmale des sechs dimensionalen Phasenraums des vom Photoinjektor erzeugten Elektronenstrahls untersucht werden. Die vorliegende Dissertation konzentriert sich auf die Analyse der longitudinalen Eigenschaften der Elektronenpakete, das heisst sowohl die zeitliche Ladungsverteilung als auch die Impulsverteilung sowie die Korrelation beider. Die Elektronenverteilung im longitudinalen Phasenraum des Photoinjektors wurde zunächst am bestehenden System erstmals vollständig bei einem Impuls von 5 MeV/c gemessen. Dieses System war für einen Beschleunigungsgradienten von 40 MV/m entworfen worden. Die Subkomponenten des Messsystems wurden untersucht, um Quellen für Unsicherheiten zu verstehen. Ein höherer Beschleunigungsgradient in der Kavität (60 MV/m, der einen Strahlimpuls von etwa 6.8 MeV/c ergibt) erfordert umfassende Modifikationen am bestehenden System zur Messung der Elektronenverteilung im longitudinalen Phasenraum. Ein Ausbau der Anlage mit einer zusätzlichen Beschleunigungskavität machte den Entwurf von weiteren longitudinalen Messsystemen für die Analyse der Strahleigenschaften bei höheren Impulsen (bis zu 40 MeV/c) notwendig. Messungen der longitudinalen Strahleigenschaften zur Bestimmung des Einflusses verschiedener Eingangsparameter, wie die Lage der HF-Startphase, die Ladung, die Beschleunigungsspannung und des Laserprofils wurden durchgeführt und mit Simulationen verglichen.

Contents

Chapter 1

Introduction

Most scientific cognitions are based on observations of the environs. Light is an important tool to observe nature and materials. To resolve microscopic structures the wavelength of the light has to be smaller than the structure to be analyzed. Hence, to observe smaller and smaller structures, shorter and shorter wavelengths are needed. Even more demanding is the observation of fast processes of such small structures. In order to observe fast processes short and highly brilliant pulses with a high repetition rate are mandatory. Coherent waves offer the opportunity to determine the three-dimensional spatial information of an object.

A *F*ree-*E*lectron *L*aser (FEL) fulfills all these requirements, as it produces extremely brilliant, coherent light with very short pulse lengths. Wavelengths in the range from microwaves down to X-rays can be achieved. A major advantage is the tunability of the wavelength. The laser pulses of an X-ray FEL are ideal for imaging and to resolve atomic structures or even individual protein molecules and observe changes on the femtosecond scale during chemical or biological reactions. Besides chemistry and biology, X-ray FELs open new possibilities for science in pharmacy, materials research, nanotechnology, plasma physics and many other fields. An overview about existing an planned FELs can be found under [FEL08].

FLASH, the *F*ree-Electron *LAS*er in *H*amburg [FLASH08], is the first (and up to now only) Free-Electron Laser in the world that produces femtosecond pulses of soft X-rays. In October 2007, lasing at 6.5 nm with an electron beam of about 1 GeV was demonstrated at FLASH [FLASH08]. Figure 1.1 shows a schematic of the FLASH setup.

The European XFEL [XFEL06] is designed to reach wavelengths from $\lambda = 6\,\text{nm}$ down to 0.085 nm with a pulse duration shorter than 100 fs. Pulse trains of up to 650 μs duration with 10 Hz repetition rate and a bunch repetition rate of up to 5 MHz will be produced.

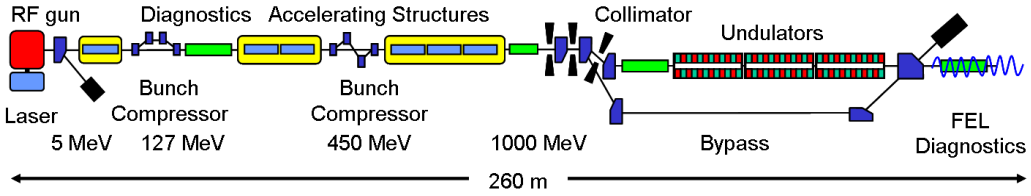

Figure 1.1: *Schematic of the FLASH setup [FLASH08]. It consists of the electron source, further accelerating cavities, two bunch compressors, several electron beam diagnostics, magnets, the undulator section the beam dump and the section for photon diagnostics and application.*

Unlike a conventional laser, which consists usually of a laser medium with at least three energy levels, an energy pump, and an optical resonator, the relativistic electrons of a Free-Electron Laser are not bound to atomic, molecular or solid-state levels but are moving freely in vacuum (hence the name: free). An electron beam, accelerated to high energies in a linear accelerator replaces the active laser medium and the energy pump as well. The high energetic electron beam is forced onto a sinusoidal path by an undulator, which consists of a periodic magnetic structure with alternating polarity. The electron beam on the curved trajectory is superimposed with an electromagnetic wave. Hence, at every half period along the undulator the direction of propagation has a finite component parallel to the electric field, but the light wave will slip forward with respect to the beam [Mad70]. The condition for an effective energy transfer to the light wave is an advance of the light wave of half a wavelength ($\lambda_r/2$) per undulator half-period with respect to the electron beam. Thus the relation between the wavelength (λ_r) and the undulator period (λ_u) is given by the resonance condition:

$$\lambda_r = \frac{\lambda_u}{2\gamma^2}\left(1 + \frac{K^2}{2}\right). \tag{1.1}$$

γ is the Lorentz factor and $K = \frac{eB_0\lambda_u}{2\pi m_0 c}$ the undulator parameter, which depends on the peak magnetic field B_0 and the undulator period, c is the velocity of light, m_0 is the electron rest mass and e the charge of an electron. This wavelength is identical to the wavelength of spontaneous undulator radiation. The wavelength can be tuned by varying the beam momentum (or the magnetic field).

The initial wave to be amplified is either an already existing light wave, e.g. from a (conventional) optical laser (called seeding), or spontaneously emitted undulator radiation. For X-rays no optical lasers exist, so spontaneous emission has to be used. Furthermore, for wavelengths smaller than

150 nm no mirrors are available, so the use of optical resonators is impossible and the amplification of the light wave has to be achieved in one pass.

The spontaneously emitted undulator radiation starts the *S*elf-*A*mplified *S*pontaneous *E*mission (SASE) process [KS80]. The radiation interacts with the highly energetic electron beam, resulting in a density modulation of the longitudinal electron beam distribution. The density modulations, called microbunching, are caused by the deceleration of the electrons due to the energy transfer to the electromagnetic wave and thus the bunch is divided in several slices. Since the emission of spontaneous undulator radiation is a stochastic process, the SASE process is characterized by fluctuations in wavelength (by up to $\pm 1\,\%$) and pulse energy. The power of the coherently emitted wave at the resonant wavelength grows exponentially with the distance z along the undulator during the process of microbunching until the micro-bunches are fully developed and saturation is reached. The characteristic length of exponential growth is called gain length L_g, and depends critically on the electron beam parameters [SSY04]:

$$L_g = L_{g0}\,(1+\delta)\,, \tag{1.2}$$

with

$$L_{g0} = 1.67 \left(\frac{I_A}{I}\right)^{1/2} \frac{(\varepsilon_n \cdot \lambda_u)^{5/6}}{\lambda_r^{2/3}} \frac{(1+K^2)^{1/3}}{K A_{JJ}} \tag{1.3}$$

and

$$\delta = 131 \frac{I_A}{I} \frac{\varepsilon_n^{5/4}}{\lambda_r^{1/8}\lambda_u^{9/8}} \frac{\sigma_\gamma^2}{(1+K^2)^{1/8} + (K A_{JJ})^2}. \tag{1.4}$$

In this formula I_A is the Alfven current[1]. σ_γ is the rms energy spread (in units of the rest energy), $A_{JJ} = (J_0 - J_1)(K^2/2(1+K^2))$ for a planar undulator, J_0 and J_1 are Bessel functions of the first kind. A small gain length can be reached with a high peak current I and a small normalized transverse rms emittance ε. The transverse beam emittance is a measure of the area occupied by the particles of the beam in transverse phase, which is a coordinate system spanned by the canonical variables: the position and the momentum orthogonal to the design orbit. When the bunch is accelerated, the emittance decreases inversely proportional to the momentum. Thus the normalized emittance was introduced as[2]: $\varepsilon_n = \frac{p_0}{m_0 c}\,\varepsilon$.

Furthermore, the radiation power grows quadratically with the number of particles that participate in the lasing process. To realize this, a good overlap

[1]The Alfven current is a soft limit on the amount of charge that can be transported in a non-relativistic beam (for electrons: $I_A = 17\,\mathrm{kA}$.)

[2]In section 2.2.3 more details can be found.

of photon and electron beam over the whole undulator length is needed. Hence a very high peak current, a small beam size and divergence, which means a small geometrical transverse emittance are major beam parameters.

This means that to obtain a short gain length and a highly brilliant X-ray light pulse a high energetic electron beam with the following properties is required for the SASE-principle:

- a small transverse emittance, to reach a good overlap of the electron beam with the photon beam over the whole undulator length,
- a high peak current, to reach a high radiation power within a small gain length,
- a small energy spread, to have many particles within the lasing bandwidth.

The goal electron beam parameters at the entrance of the undulator for the European XFEL are an electron beam energy of 17.5 GeV[3] with an uncorrelated (rms) energy spread of 2.5 MeV, a normalized slice emittance of $\varepsilon_n = 1.4\,\mathrm{mm\,mrad}$, a charge of 1 nC and a peak current of 5 kA [XFEL06, XFEL07].

It is impossible to reach these conditions in a storage ring, because such a short beam circulating in a ring would be destroyed. Therefore a *LIN*ear *AC*celerator (LINAC) is essential for short wavelength FELs. There are also strong requirements on the stability of beam position and energy.

Since the beam quality can only degrade during propagation along the accelerator[4] up to the undulator (for example due to space charge forces, wakefields and *c*oherent *s*ynchrotron *r*adiation(CSR)), the demands on the injector are very challenging. According to beam dynamics simulations taking into account the effects mentioned before, a normalized slice emittance of $\varepsilon_n = 1.4\,\mathrm{mm\,mrad}$ at the undulator requires a normalized projected emittance of $\varepsilon_n = 0.9\,\mathrm{mm\,mrad}$ at the exit of the injector.

The geometrical emittance could be decreased by increasing the energy, but the accelerator would become larger. Therefore the development of an electron source with a low emittance is of great importance for reducing size and cost of SASE-FELs [Kim04].

The energy gain in the electron source is of the order of a few MeV. At low energy, e.g. during emission, for an electron bunch of a charge of about

[3] the maximum design energy is 20 GeV for an accelering gradient of 23.6 MV/m in 104 modules

[4] The Liouville Theorem demands the normalized emittance of the accelerated beams to stay constant if the accerated particles of the beam do not interact. See chapter 2.2.3

1 nC, space charge forces are the main source of emittance growth. To minimize the influence of space charge forces in order to conserve the transverse emittance, a peak current in the kA range should not be produced directly in the electron gun. Therefore the initial bunch length is chosen several orders of magnitude longer (about 6 mm FWHM[5]) than required for FELs to give a moderate peak current of about 50 A in the injector. When the energy of the accelerated electron beam is high enough that space charge forces can be neglected[6], the bunch length can be reduced in order to increase the peak current by using a bunch compressor (BC). A bunch compressor is a magnetic chicane consisting of several (typically four) dipole magnets which introduces a deviation from a linear path. The first step of the compression

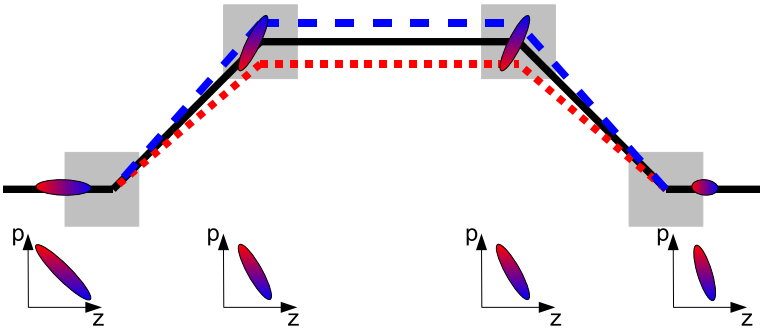

Figure 1.2: *Working principle of a bunch compressor. The higher energetic electrons at the tail of the bunch travel a shorter distance in the chicane, they catch up with the leading particles and the bunch is compressed.*

is to accelerate the bunch on the falling slope of the RF wave in the cavity upstream the BC in order to produce an energy slope (chirp) such that particles at the head of the bunch receive a smaller energy gain than those at the tail. In the magnetic chicane (see figure 1.2) the higher energetic electrons at the tail of the bunch travel a shorter distance, since they are deflected less from the initial path by the dipole magnets. Thus they catch up with the leading particles at lower energy and the bunch is compressed. At FLASH two magnetic chicanes are installed at about 127 MeV and 450 MeV, which typically compress the bunch by a factor 8 in the first and 5 in the second bunch compressor. An optimum compression of the bunch can be reached only for a linear position-energy relationship of the particles inside the bunch

[5]Since the bunches are moving relativistically, $\Delta z = 6$ mm bunch length corresponds to a bunch duration of about $\Delta t = \frac{\Delta z}{c} = 20$ ps FWHM. Due to the constant ratio between bunch length and duration for relativistic particle both values are often mixed.

[6]space charge forces decrease with the beam energy, see section2.2.4

(linear distribution of the electrons in the longitudinal phase space), but due to the sinusoidal-shape of the RF fields and coherent synchrotron radiation effects in the magnetic chicane non-linearities appear. The bunch resulting from these non-linearities consists of a leading spike with a duration of less than 100 fs and a tail of several picoseconds. The spike contains about 10 to 20 % of the total bunch charge, this means the peak current strongly exceeds 1 kA, which is needed for lasing in the high-gain FEL process. In contrast the current in the tail is too low to expect any significant FEL gain. A sinusoidal shape can be linearized in the vicinity of a given phase by adding its odd harmonics. Therefore a third harmonic cavity is planned to be installed before the first bunch compressor in order to linearize the electron bunch distribution in the longitudinal phase space. Then, the entire bunch charge can take part in the lasing process. Thus, the knowledge of the shape of the electron bunch distribution in the longitudinal phase space before the third harmonic cavity and the understanding of the beam dynamics in the injector is of particular interest and has to be studied in detail. Special attention is also paid to the possibility of amplification of high frequency modulations in the current density due to plasma oscillations[7]. These modulations create microstructures in the bunch distribution in the longitudinal phase space, which can prevent operation of the FEL. Microbunching instabilities are driven by CSR effects, wakefields and particularly *l*ongitudinal *s*pace *c*harge (LSC) effects [SSY]. Modulations on top of the longitudinal laser profile of the photocathode laser in the photoinjector might initiate the perturbations in the current distribution. Very small uncorrelated energy spread[8] is a major reason for the developments of the LSC instability and of the micro-bunching instability due to CSR, which can occur when energy modulations are converted to current modulations during the compression.

Furthermore different observations with the *o*ptical *t*ransition *r*adiation (OTR) diagnostics at LCLS indicate the presence of coherent OTR for both uncompressed and compressed electron bunches, which compromise the use of OTR as a reliable beam diagnostics beyond the injector [Dow07, Los08]. While for the uncompressed beam only a small fraction of the beam radiates coherently, highly compressed bunches show a large coherent enhancement. For uncompressed bunches the phenomena could be explained by the amplification of shot-noise in the beam due to a micro-bunching instabilities. The effect for compressed bunches could be dedicated to a shift of long wavelength

[7]Plasma oscillations describe the transformation of beam current modulations into energy modulation due to longitudinal space charge forces, which transform into current modulations again, at low energy.

[8]The uncorrelated energy spread describes the energy spread at a certain longitudinal position of the bunch, also called local or slice energy spread.

micro-structure into the visible and the generation of micron-length spikes in the compression process [Los08].

The Photoinjector Test facility at DESY, Zeuthen site (PITZ) [FS99] was built for research and development on sources of high brightness electron beams for Free-Electron Lasers and linear colliders. PITZ will be introduced in chapter 2. The main challenge is to produce an electron beam with a very small transverse emittance, small momentum spread and a peak current of about 50 A. The operation of PITZ includes a continuous conditioning[9], characterization of RF photoinjectors [Fra86], test of new components and optimization. FLASH is already running with a gun prepared and characterized at PITZ, but to fulfill the high requirements for the European X-ray Free-Electron Laser (XFEL) an extension of the PITZ facility and its research program is necessary. For a successful optimization a second accelerating cavity was installed downstream the gun to understand the process of conserving small transverse emittance beams during further acceleration. To reach the demanding requirements, high-resolution diagnostic instruments are essential for a detailed understanding of the physical principles of beam production, beam dynamics and emittance preservation.

In various facilities all over the world, working with electron guns, a high effort has been spent on measuring the transverse emittance [Sta07, Sch01, Cia08, Park05, Loe06], since its minimum value significantly depends on effects at the cathode and inside the gun.

But a small transverse emittance is only meaningful when a small momentum spread and moderate peak current (e.g. 50 A for an L-band RF photoinjector) is reached and the corresponding longitudinal phase space distribution allows an optimized compression of the bunch. Therefore simultaneous measurements of transverse and longitudinal emittance are mandatory. Since most measurement methods at medium peak current and low energy are destructive, the measurements have to be done successively under similar operation conditions.

In this thesis the focus is on the measurements of the beam distribution in longitudinal phase space performed at PITZ. In chapter 2 the properties of the electron bunch in the longitudinal phase space of an L-band RF photoinjector are introduced with the help of an example. A special emphasis of the thesis lies on the development and analysis of the diagnostics to determine the longitudinal phase space distribution (chapter 4). Measurements of the longitudinal density distribution, including bunch length and momentum distribution for different conditions were made. The first measurements of the

[9]Improvement of the outgassing and surface roughness of the cavity material. Smoother surfaces emit less dark current, which destroys the cathode and diagnostics.

momentum and the longitudinal distribution at PITZ were presented by D. Lipka in [Lip04, Lip03-2, Lip03-1]. After these measurements the accelerating field amplitude in the gun was increased from 42 MV/m to 60 MV/m and a booster cavity was included in the setup to demonstrate the conservation of the transverse emittance towards higher beam energies. These changes necessitate a change of the existing longitudinal diagnostics and the design of new devices. For the first time the full longitudinal phase space distribution of a gun was measured directly at about 5 MeV. The influence on various machine parameters like RF launch phase, beam charge, accelerating gradient and photocathode laser distribution were analyzed. The results of measurements and beam dynamics simulations using the ASTRA code[10] are compared and presented in this work in chapter 5.

[10] *A Space charge TRacking Algorithm* is a code which tracks particles through user defined external fields, based on fourth order Runge-Kutta integration. It contains a space charge algorithm based on a rotational symmetric mesh [Flo]. This code is using macro-particles instead of single particles in order to reduce the time of the simulation.

Chapter 2

Production of electrons and the setup of PITZ

2.1 Electron sources for FELs

As pointed out in the introduction there are strong requirements on the entire phase space of the electron bunch used for a SASE-FEL. The electron source defines the minimum of the transverse emittance and major properties of the longitudinal phase space. During the last decades different types of electron sources were developed and are still under development. A short overview is presented in this section.

2.1.1 DC electron gun

In DC guns a static voltage is applied for the acceleration to energies of a few hundreds of keV. The static DC scalar potential is provided by a drive voltage pulse, means the direct current voltage supplied only for a certain time. The advantages of DC guns are the high operating experience, the high voltage stability and the good vacuum conditions. A big disadvantage of DC guns is the low accelerating gradient, which causes strong space charge forces in the bunch for moderate peak currents. There are two methods used to extract the electrons to be accelerated: thermal electron emission and photo-electron emission.

In a thermionic gun electrons are emitted by heating the cathode material. This means continuously emission of electrons during the HV pulse of static (DC) voltage. Because of the limited switching speed of the driver circuits the bunch duration in a thermionic DC gun is generally more than 1 ns, therefore the use of a buncher cavity is necessary. However, thermionic cathodes are robust and have a long lifetime. In 2006 the *S*Pring-8 *C*ompact *S*ASE *S*ource

(SCSS), a prototype accelerator for the Japanese XFEL project, demonstrated first lasing at 49 nm using a thermionic DC gun combined with a beam deflector and subsequent velocity bunching [Shi06].

In a photo-cathode gun a laser beam releases electrons due to the photoelectric effect. The temporal structure of the beam is basically defined by the temporal laser distribution and the cathode response. The emittance of the beam is limited by the thermal emittance, a property of the cathode in combination with the laser. Typically GaAs is preferred as cathode material due to its low achievable thermal emittance by using a proper laser system. The disadvantage of GaAs cathodes are their sensitivity to vacuum contamination. A successful operation of photocathode DC guns was shown for example in the Jefferson Lab IR FEL [Her05]. In JAEA (Japan Atomic Energy Agency) a photocathode DC gun is under development for a high-power FEL in an energy-recovery LINAC (ERL)[Haj07].

2.1.2 Normal conducting RF gun

The application of an RF field for acceleration has the advantage of a much higher usable gradient compared to DC guns. The field is typically several tens of MV/m. The high field gradient accelerates the beam immediately up to several MeVs. Also for RF guns both thermionic and photocathode guns exist.

Using a combination of an RF gun with a thermionic cathode leads to an emission of electron beams with a huge energy spread. An α-magnet with a slit is often used to choose a certain energy range and to compress the bunch. Back bombarding induces a heating of the cathode and limits it usage. The longitudinal bunch distribution can be controlled by the gun design and choosing the energy range. The advantage of a thermionic RF gun is a low-cost and simple system, which does not need to be synchronized. Thermionic RF guns are used for example in the *S*tanford *S*ynchrotron *R*adiation *L*aboratory (SSRL) [Bor] and the *A*dvanced *P*hoton *S*ource (APS) [APS08].

In an RF gun based on photoelectron emission, also called RF photoinjector, the bunch length is predefined by the laser pulse length, which is typically on the order of picoseconds. The properties of the bunch depend on the phase of the RF cycle at which the electrons are released. With the appropriate phase, a high accelerating gradient and optimized laser pulse properties the effects of space charge forces can be reduced. The operating experience with RF photoinjectors is high. The lowest transverse emittance for a bunch charge of 1 nC and a peak current of several tens of Amperes was measured up to now with RF photoinjectors. The disadvantages are medium

vacuum conditions and the limited average power due to the water cooling and of course the higher costs compared to other conventional gun types. An RF S-band (2.856 GHz) photoinjector is in use at the *L*inac *C*oherent *L*ight *S*ource (LCLS) [LCLS04]. The RF frequency of normal conducting photoinjector of PITZ (schematically shown in 2.1), FLASH and the European XFEL was chosen according to the superconducting main linac with 1.3 GHz (L-band), which was optimized to reach low costs, small surface resistance and reduced wakefieds [TESLA01].

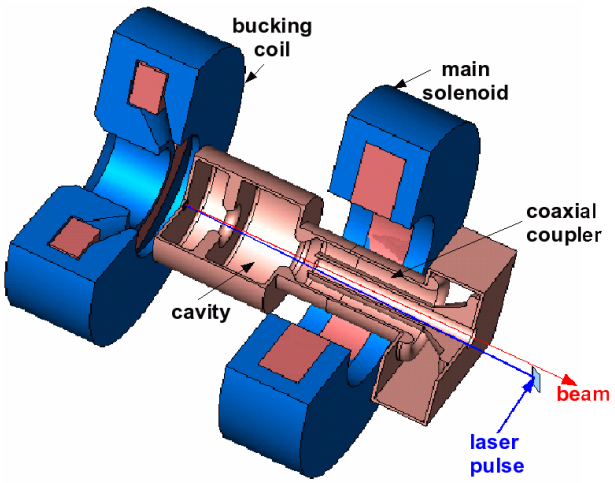

Figure 2.1: *Schematics of the RF gun with the coaxial coupler used at PITZ: a 1.6 cell, standing wave, copper cavity with a Cs_2Te photocathode.*

2.1.3 Superconducting RF gun

A superconducting gun allows continuous operation and thus high average currents. Superconducting cavities provide good vacuum conditions and a rather high accelerating gradient[1], but the possibility of space charge compensation is more difficult since the magnetic field may cause degradation in the performance of the superconducting cavity. Therefore the emittance compensating solenoid (see section 2.2.5) has to be placed at a different location than the superconducting cavity (also called: slit injector) to reach a charge comparable to normal conducting cavities. Another challenge is the choice of

[1]The maximum accelerating gradient of a superconducting cavity is determined by the rf critical magnetic field (Niobium cavities for electron accelerators are hence limited to about 50 MV/m), but the common limiting mechanisms are electron field emission and thermal breakdown [Kno99].

the cathode material. Superconducting cathodes have a moderate quantum efficiency that requires a high cathode laser pulse energy, but the integration of a non-superconducting cathode (with a higher quantum efficiency) has to be done in a way that preserves the original high intrinsic quality factor of the cavity [Sek07]. A superconducting RF photo injector is under development at the research center Dresden-Rossendorf with the ELBE source (*E*lectron *L*inac for beams with high *B*rilliance and low *E*mittance) [ELBE08].

2.1.4 Plasma acceleration

The technique to accelerate charged particles using an electric field associated with a plasma wave, was proposed in 1985 [Che85]. The wave is generated when a short laser or electron pulse passes through a plasma. The main advantage is the very high energy gain over a small distance. The main problem of plasma acceleration is the limited stability and the large energy spread [Lee02] and the missing experience. So-called table-top-FELs are investigated for example at Ludwig-Maximilians University Munich [Gru99] and at Lawrence Berkeley National Laboratory [LBL09].

2.1.5 Field-Emission cathodes

Low emittance guns based on a Field-Emission Array or a Needle Cathode Field Emitter are under investigation at the Vanderbilt University [LB03] and the Paul Scherrer Institut (PSI) [PSI08]. With a larger surface field, the potential barrier to the vacuum is lowered. Field-Emission cathodes are expected to have a small thermal emittance. The small initial beam size induces strong space charge forces, therefore a very high acceleration field is needed to keep the emittance small. To avoid discharges due to the high field, which can destroy the emitter, good vacuum conditions are mandatory. The peak current of field emitters is still limited due to the generation of vacuum arcs, that may destroy the emitters because of local heating. Field-Emission cathodes for FELs are still in the stage of development.

2.2 PITZ

Since normal conducting photocathode RF guns have been proven to produce beams with a peak current of several tens of Amperes, a small momentum spread and up to now the smallest transverse emittances for 1 nC bunch charge, they are used or planned to be used as electron source for several FELs, especially for those which aim at wavelengths in the X-ray range (like

LCLS and the XFEL). Since FLASH is a user facility and the possibility for research and development is limited, the Photoinjector Test facility at DESY in Zeuthen was founded with the goal to prepare, test and optimize photocathode electron RF guns and diagnostics for superconducting linear accelerator driven FELs like FLASH and the European XFEL at DESY in Hamburg.

Since the European XFEL should be able to produce long pulse trains superconducting accelerating cavities are required for the acceleration of the long bunch trains in the main linear accelerator. The heart of the PITZ facility is a 1.6 cell, standing wave, copper cavity (see figure 2.1) with a Cs_2Te photocathode, which allows the production and initial acceleration of long bunch trains. Its performance is studied by numerous diagnostics elements.

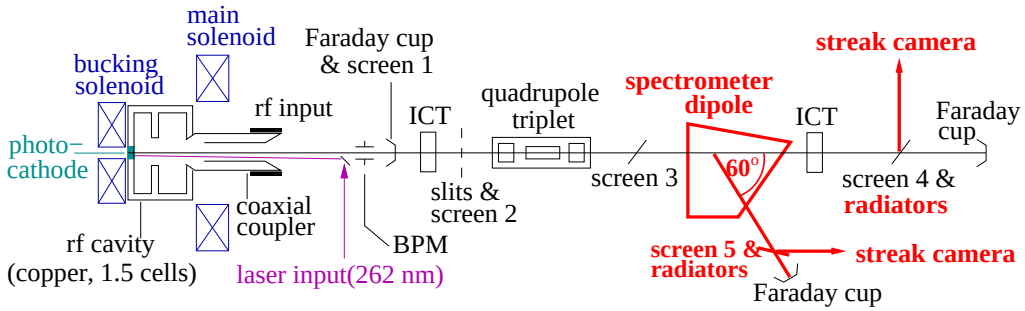

Figure 2.2: *The PITZ1-setup had a length of about 5 m. The longitudinal phase space diagnostics is marked (fat/red).*

During the compilation of this thesis, the facility was stepwise extended from "PITZ-1" (Figure 2.2) to the current state, the so called "PITZ-1.7" setup (Figure 2.3). The extension of the facility was initiated by the installation of a further accelerating structure (booster cavity) in 2005. The "TESLA booster"[2] is a nine-cell copper cavity. Its water cooling channels are limiting the usable RF power. The diagnostics section had to be adapted to the new setup and further diagnostics systems were developed. A further upgrade towards the so called "PITZ-2" status (Figure 2.4) is still under development. This includes a replacement of the "TESLA" booster by the 14-cell, *C*ut *D*isk *S*tructure (CDS) booster cavity, specially designed for PITZ, which should be able to reach about 30 MeV and allows an RF pulse length of 900 μs. For completeness in Appendix A the setup of the intermediate phases of the facility PITZ1.5 and PITZ1.6 are presented.

[2]The TESLA booster was initially constructed in 1992 as a prototype for a superconducting TESLA accelerating cavity and afterwards used at Fermilab as capture cavity.

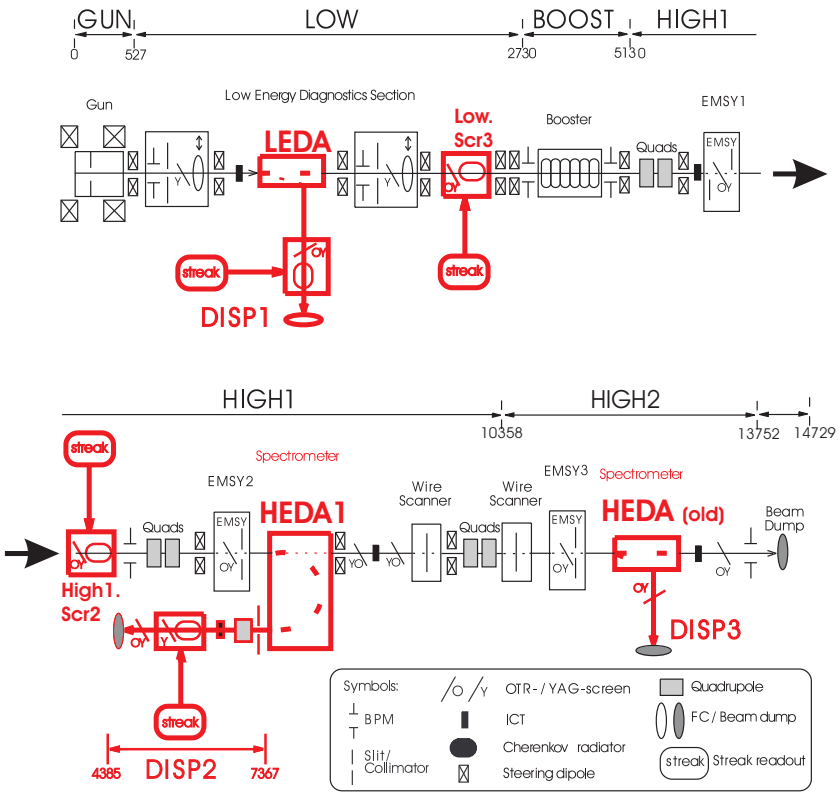

Figure 2.3: *The PITZ-1.7 setup displays the status of the facility in the running period started in summer 2008, with a length of 15 m. The longitudinal phase space diagnostics is marked.*

Within the last years several gun cavities were conditioned and characterized at PITZ. They are summarized in table B.1 in Appendix B.

2.2.1 The drive laser system

The PITZ cathode laser system was developed by the Max-Born-Institute [Wil05]. The system used until the end of 2007 contained a diode pumped Nd:YLF oscillator, which was synchronized with the RF frequency. It was followed by a pulse shaper, which transformed the initial gaussian temporal shape to a flat-top with about 20 ps FWHM and about 7 ps rise and fall times. A typical temporal distribution is shown in figure 5.17 (b). Several amplifiers increased the IR (1047 nm) pulse energy. Afterwards two non-linear optical crystals transform the wavelength to the fourth harmonic (262 nm). The laser light is transported by an optical system onto the cathode. A diaphragm with adjustable diameter called the *b*eam *s*haping *a*perture (BSA) is placed

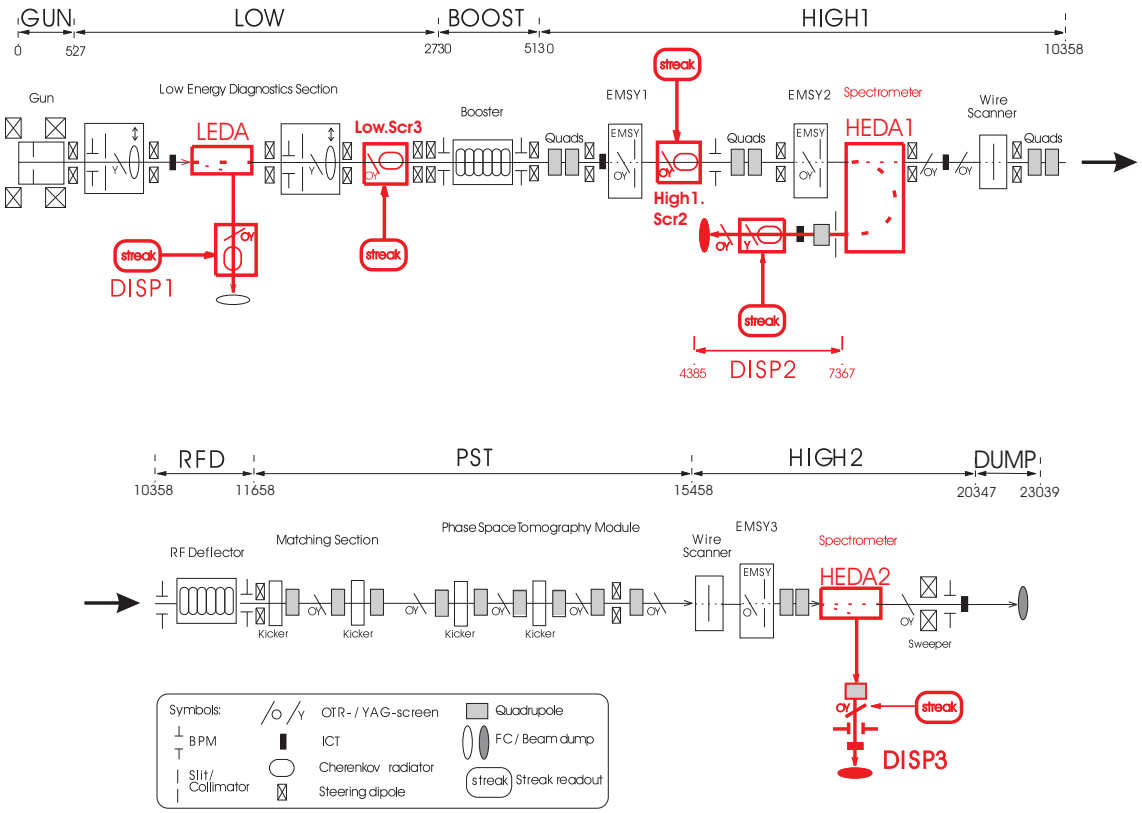

Figure 2.4: *The PITZ 2 setup shows the plans for the further development of PITZ. The longitudinal diagnostics discussed in this thesis is marked. The RF deflector is counting to the longitudinal diagnostics, but not discussed in this thesis.*

in the optical system to shape a flat-top transverse laser distribution and it is imaged onto the cathode. A laser beam with a radially and longitudinally uniform photon density is aimed at to keep transverse space charge forces within the bunch linear (see section 2.2.4). Therefore, a new laser system was installation in 2008 which should provide shorter rise times (2 ps) and less residual modulations. The gaussian pulse with a FWHM of about 2 ps enterning the pulse shaper is split into mutually delayed replicas due to the birefringence of the crystals. All replicas interfere at the output polarizer of the filter and form the shaped output pulse a duration of about 20 ps with rise times of about 2 ps, in a phase-coherent manner [MBI08]. The laser system produces a pulse train with variable length of up to 800μs (800 pulses) at a repetition rate of 1 to 10 Hz.

2.2.2 Electron beam production

The photocathode plugs used at PITZ and FLASH for electron beam production are made of molybdenum and coated with a thin (few tens of nanometers) cesium telluride Cs_2Te [CERN94] layer. The cathodes are produced at INFN (Istituto Nazionale di Fisica Nucleare) in Milano [Ser05]. With such a cathode a quantum efficiency (QE)[3] for photoelectron emission of about 0.5 to 10% and a lifetime of several months is typical. Cs_2Te cathodes provide a homogenous QE over the cathode area to transfer the properties of the laser beam to the electron beam, but the QE depends on the field at the cathode, since it causes a bending of the band and increases the probability of tunneling. The QE is generally defined without field at the cathode. In ASTRA the dependence of the emitted charge from the actual accelerating field strength (RF + space charge) in the center of the cathode $E_{acc}(t)$ can be described by:

$$Q_{macroparticle} = \frac{Q_0 + E_{acc}(t) \cdot Q_{SL} + \sqrt{E_{acc}(t)} \cdot Q_{SQ}}{N_{macroparticles}}, \tag{2.1}$$

with $Q_{macroparticle}$ the charge of a macroparticle (which contains several electrons) and $N_{macroparticles}$ the number of macroparticles. Q_0, Q_{SL} and Q_{SQ} have to be adjusted by the user. Since these parameter vary between different cathodes and there exits no standard values for our setup this is often neglected in simulations not base on a certain measurement. This means only the pure photo emission is considered: $Q_{SL} = Q_{SQ} = 0$.

Analyses of thermal emittance of the cathodes as well as surface properties, before and after usage, are ongoing to get a better understanding of the emission process [Led07]. The cathode is located at the backplane of the half cell of a 1.6 cell copper cavity, operated in the π-mode with a resonance frequency of 1.3 GHz. The cavity has a cylindrical symmetry. The electron bunches are produced using the photo-effect by illumination of the cathode with short, high power UV laser pulses. The generated electrons are immediately accelerated by the RF field of the gun. The accelerating field is delivered by either a 5 MW (TH2104-C, Thales) or 10 MW (TH1801-MBK, Thales) klystron [Cho07] through a coaxial RF coupler avoiding emittance growth by field asymmetries. The reached peak electric field E_0 is proportional to the square-root of the power in the gun cavity P. This relation depends on the shunt impedance and the field balance (FB)[4]. Since there

[3] $QE = \frac{n_e}{n_p}$, with n_e the number of emitted electrons and n_p the number of incident photons.

[4] The field balance (FB) describes the ratio of the field amplitude at the cathode E_z^{cath} to the one at the full cell E_z^{full}, $FB = \left|\frac{E_z^{cath}}{E_z^{full}}\right|$.

are losses of power in the waveguides, not the full klystron power is available in the gun. A high accelerating gradient directly at the cathode is of high importance, because the transverse space charge forces are inversely proportional to the square of the relativistic factor of the electrons ($F_{r-SC} \propto \frac{1}{\gamma^2}$) (as shown in section 2.2.4).

2.2.3 The phase space and transport matrix

The orbits of the charged particles depend on electric (E) and magnetic fields (B). The forces influencing the beam dynamics of the electron bunch, like acceleration, focussing and space charge, can be described by the the Lorentz force:

$$F_L = \frac{dp}{dt} = m_e \frac{d}{dt}(\gamma \vec{v}) = q(\vec{E} + \vec{v} \times \vec{B_\vartheta}), \tag{2.2}$$

with q the particle charge, v the velocity of the particle and m_e the electron mass.

The evolution of many physical systems after a time t depends only on their state at that time. This is determined by the values of r coordinates $q_i = (i = 1, .., r)$ and their time derivatives $\dot{q_i}$, with the integer r being the number of degrees of freedom. The canonical phase space is the 2r-dimensional space with the conjugate coordinates q_i, p_i, thus for $r = 3$ the kinematic properties of a particle relative to the design orbit can be described by a 6-dimensional vector (x, p_x, y, p_y, z, p_z). The phase space coordinates of the electrons are given in a frame Σ' which moves with the reference particle relative to the laboratory frame Σ_L along the reference trajectory. In general z describes the longitudinal position, the position in the direction of motion. x describes the horizontal and y the vertical displacement from the design orbit, they are summarized as transverse positions. The three spatial coordinates and their momenta of all particles within a bunch span the six dimensional phase space. The phase space volume occupied by the beam is called its emittance. In general the six dimensional phase space is subdivided into two transverse $(x - p_x, y - p_y)$ and the longitudinal phase space $(z - p_z)$, since the longitudinal motion usually is decoupled from the motion along the beam axis. The longitudinal phase space describes the position and the momentum of all particles in the bunch and their correlation.

Usually the transverse components of the momentum p_x and p_y are normalized to the longitudinal momentum component p_z and presented as angular divergence ($x' = p_x/p_z, y' = p_y/p_z$).

It is important to have a measure of the quality of a bunch in terms of their ability to be transported over long distances. To describe the electron bunch quality for electron accelerators typically the rms emittance is used.

It is described for the longitudinal direction by:

$$\varepsilon_z = \sqrt{< l^2 >< \Delta p_z^2 > - < l\Delta p_z >^2}, \tag{2.3}$$

where $< .. >$ describes the average value of the particle distribution, l is the longitudinal distance to the reference particle and Δp is the difference from the design momentum $< p >$.

Liouville's theorem is a conservation law for volumes in canonical phase spaces. If a system of non-interacting particles evolves under the influence of conservative forces, then the local density of particles in the phase space is preserved throughout the evolution of the particle collection. The Liouville's theorem still applies for the longitudinal emittance, because time and energy are canonically conjugate variables. Liouville's theorem applies only to particles guided by external fields, if interactions of a particle than with its closes neighbours can be neglected the theorem of Liouville is still a good approximation. A coupling of longitudinal and transverse particle motions can be caused by focussing elements whose forces are energy-dependent.

The transformation of an electron with the initial phase space coordinates (x_0, x_0', y_0, y_0', l_0, δ_0) passing a component like a magnetic lens, can be determined by multiplication of the 6 dimensional phase space vector with the first order transport matrix R [Bro92]:

$$\begin{pmatrix} x \\ x' \\ y \\ y' \\ l \\ \delta \end{pmatrix} = R \begin{pmatrix} x_0 \\ x_0' \\ y_0 \\ y_0' \\ l_0 \\ \delta_0 \end{pmatrix}, \tag{2.4}$$

with $\delta = \frac{\Delta p}{<p>}$ the normalized momentum difference from the design momentum $< p >$.

2.2.4 Space charge forces

Space charge forces are Coulomb interactions in a multi-particle system. They can be generate by binary collisions caused by close particle encounters or by the self field produced by the particle distribution. At low energies the space charge forces affect the longitudinal dynamics as well as the transverse one.

In the moving frame of the bunch Σ' the electric $\vec{E}'$ and magnetic field $\vec{B}'$ of a point charge with uniform motion can be described by:

$$\vec{E}' = \frac{e}{4\pi\varepsilon_0}\frac{\vec{r}'}{r'^3}, \tag{2.5}$$

$$\vec{B}' = 0, \tag{2.6}$$

with e the electron charge.

By transformation to the laboratory frame Σ_L the fields become:

$$\vec{E} = \frac{e}{4\pi\varepsilon_0} \frac{\gamma\vec{r}}{(x^2 + y^2 + \gamma^2 z^2)^{3/2}}, \tag{2.7}$$

$$\vec{B}_\perp = \frac{\vec{v} \times \vec{E}}{c^2}. \tag{2.8}$$

.

These fields exert a transverse force $\vec{F_r}$ on the particles at radius r in a cylindrically symmetric bunch with a homogeneous charge distribution, calculated by the Lorentz force [Pal05]:

$$\vec{F_r} = e(E_r - vB_\vartheta) = e(E_r - \beta^2 E_r) = \frac{eE_r}{\gamma^2} = \frac{eIr}{2\pi\varepsilon_0 c\beta\gamma^2 a^2}, \tag{2.9}$$

with a total current of I. It is a linear function of the transverse coordinate r. The attractive magnetic force, which becomes significant at high velocities, tends to compensate for the repulsive electric force. Therefore, space charge defocusing is primarily a non-relativistic effect. For a cylindrically symmetric bunch the space charge force is linear to the transverse bunch radius and inversely proportional to the square of the relativistic factor of the electrons.

The longitudinal space charge force for a uniform, cylindrical bunch distribution is given by [Pal05]:

$$F_z(r,z) = \frac{eE_s(z)}{m_e c^2} = \frac{-e}{4\pi\varepsilon_0\gamma^2}(1 - \frac{r^2}{a^2} + ln\frac{b}{a})\frac{\delta\lambda(z)}{\delta z}, \tag{2.10}$$

where E_s is the longitudinal space charge electric field, a is the transverse beam size radius (assumed uniform disk), b is the pipe radius (assumed cylindrical and perfectly conducting).

The equations for longitudinal and transverse space charge forces are considered independent here, but actually they are coupled.

2.2.5 Emittance compensation and conservation

The phase dependent focussing forces in the RF field result in an RF induced emittance growth, therefore the bunch dimensions have to be chosen small. On the other hand the increased particle density causes a significant emittance dilution by the space-charge forces within the electron bunch. The space charge acts to the first order as a defocussing lens, this means the

strength of these space charge forces depends on the longitudinal position in the bunch, they are stronger in the cental longitudinal slice of the bunch than in its tails. Consequently the radial momentum of the center slices is higher. Thus a fan-like structure of the bunch in the transverse phase space is introduced, since the relation the transverse position (x) and the divergence (x') depend on the longitudinal position in the electron bunch. Therefore the projected emittance grows due to the different divergence. B. Carlsten introduced the idea to use an external solenoid magnet that counteracts the defocussing caused by linear space charge forces to compensate this emittance dilution [Car89]. The solenoid applies a focusing kick which changes the relation between the transverse position (x) and the divergence (x') depending on the longitudinal position in the electron bunch, just opposite to the space charge forces. Thus the space charge forces act against the beam divergence which partially realigns the longitudinal slices in the transverse phase space in the following drift space until a minimum transverse emittance is reached. Nonlinear space charge forces can not be corrected, therefore only a partial realignment is possible. The evolution of the distribution of a longitudinal slice in the transverse phase space depends on the current of the slice, therefore the analysis of the temporal current distribution combined with the (slice) emittance measurement is of major interest. A bucking coil installed upstream the gun cavity is used to compensate the field of the main solenoid at the photocathode, which would increase the emittance as well. For a radially uniform beam distribution emittance contribution is [Fer01/1]: $\varepsilon_{mag} = \frac{e}{2m_e c} \cdot B_z^{pc} \sigma_r^2$, with σ_r the radial rms beam size and B_z^{pc} the longitudinal magnetic field at the photocathode.

The emittance compensation process of the solenoids is only optimized for a certain position downstream the cavity were a further acceleration cavity has to be placed in order to shift the minimum emittance to a higher energy where the space charge force is sufficiently suppressed, to avoid the following emittance growth. Therefore a booster cavity was installed at PITZ in 2005 in order to study the emittance conservation during acceleration to higher energies. The so-called "invariant envelope" conditions [Fer01/1, Fer01/2] describe the proper matching condition between the properties of the electron bunch and the following accelerating cavity (booster) to reach a minimum emittance at the booster exit. It requires the booster cavity entrance at the position of the laminar waist of the beam and the local emittance maximum of the so called "double minimum". To shift the second emittance minimum to the booster exit, the energy gain in the booster (due to the applied accelerating field E_{acc}) $\gamma'_{booster}$ should be related to the transverse rms beam size

σ_w, the initial beam energy γ and the peak current I by:

$$\gamma'_{booster} = \frac{2}{\sigma_w}\sqrt{\frac{I}{3I_A\gamma}}, \tag{2.11}$$

with I_A the Alfven current. This condition guarantees the damping of the normalized emittance oscillations, that are caused by slice envelope oscillations produced by mismatches between the space charge correlated forces and the external focusing gradient for a bunch in the space charge dominated regime [LCLS02].

2.2.6 Diagnostics devices at PITZ

In order to analyze the properties of the electron beam (like transverse beam size, position and emittance as well as bunch charge, longitudinal phase space distribution and its projections) and the photo-cathode laser beam, numerous diagnostic devices are or will be installed at PITZ as major parts of the beamline, as one can see in figures 2.2, 2.3 and 2.4. To get an overview, all installed and planned diagnostic devices (for laser and electron beam) are summarized in Appendix C.

Screen stations

A major part of electron diagnostics devices used at PITZ are based on view screens, which allows to monitor the transverse electron beam distribution. In order to analyse the electron beam, light produced by the interaction of the particles with matter is observed. At PITZ YAG (yttrium aluminium garnet) and OTR (optical transmission radiation) screens are in use, mostly Si-wavers with a thickness of about 300 μm coated with YAG:Tb powder or aluminium. An OTR screen delivers an excellent spatial resolution, but the light efficiency is low at low energies. The resolution of YAG and OTR is discussed for example in [Mur01]. Each screen is combined with a lens, mirrors and a CCD camera. The resolution of the beam distribution measurement is determined by the optical focusing system and the camera properties. This is discussed in detail in [Spe07] and design considerations for certain screens are discussed in section 4.2.

2.2.7 Essential technical systems

In addition to the systems used for electron beam production, acceleration, guidance (steerer and quadrupole magnets) and diagnostics, there are several

auxiliary systems that are essential for a successful operation. These systems are the vacuum system, since the photoinjector operates in the ultra high vacuum range (to avoid degradation of the beam quality and mainly to protect the cathode), the RF system, the cooling system of the gun, booster and further components (like magnets), the temperature and humidity control of tunnel, laser hutch and racks, electronics including timing and interlock system, and the control system (to control the machine and for data acquisition). They are described in detail in [PITZ08].

2.3 Special features of the electron bunch distribution in the longitudinal phase space at PITZ

In figure 2.5 an example for a simulated electron distribution in the longitudinal phase space and its projections (temporal distribution and momentum distribution) as well as the slice momentum spread for the PITZ photoinjector is shown. Using this example, special features of the electron distribution in the longitudinal phase space of an RF photoinjector will be pointed out.

Figure 2.6 shows the maximum RF field and the longitudinal laser shape used for the simulation.

The accelerating field is described by:

$$E(z,t) = E(z)sin(\omega t + \phi), \tag{2.12}$$

with t the time after emission of a central particle within the bunch and $E(z)$ the maximum accelerating field along the cavity. An example for $E(z)$ for a field balance of $FB = \left|\frac{E_z^{cath}}{E_z^{full}}\right| = 1.03$ and a gradient of 60 MV/m at the cathode is shown in figure 2.6. ϕ is the emission phase (also called launch phase), which describes the phase of the RF field when the laser pulse hits the cathode and the electrons are emitted. It is an important optimization parameter. The emission phase which produces electrons with the highest momenta is also called "optimum phase". This optimum phase was chosen for the example in figure 2.5. The laser pulse has a length of 20 ps FWHM with rise and fall times of 2 ps and the electron bunch has a total charge of 1 nC. The resulting longitudinal beam properties are summarized in table 2.1.

The longitudinal electron bunch distribution differs from the distribution of the laser pulse. The peak current in the head of the bunch (left) is smaller than in its tail. This shape of the temporal distribution can be explained by effects of space and mirror charge. The electrons emitted from the cathode

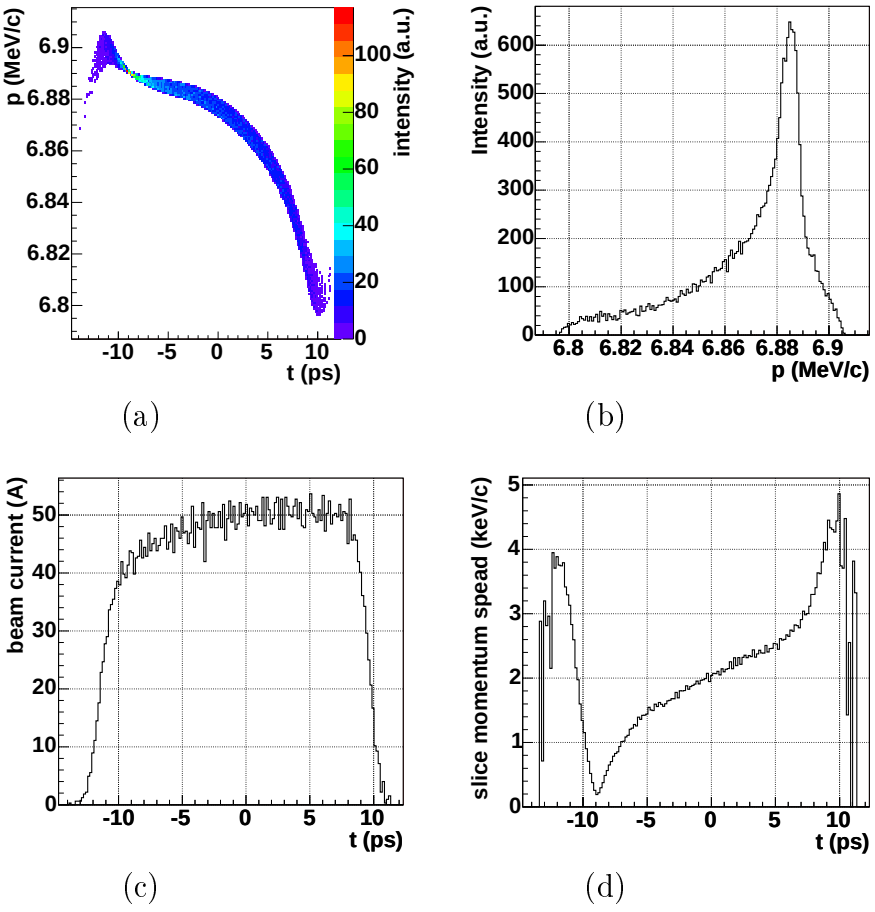

Figure 2.5: *Simulated longitudinal phase space distribution (a), momentum distribution (b), charge density distribution (c) and rms slice momentum spread (d) half a meter downstream the photocathode for the phase of maximum mean momentum gain. The simulation conditions applied to ASTRA were: 60 MV/m at the cathode, 1 nC bunch charge, a maximum main solenoid field of 176 mT, a flat top longitudinal laser distribution of 20 ps with rise- and falltime 2 ps and a transverse laser diameter of the beam of 2 mm. The head of the bunch is at about t = -10 ps.*

see the mirror image inside the cathode material with the same distance to the surface and a charge of opposite polarity (mirror charge), which acts against the force of the accelerating field. The influence of the dependance of the quantum efficiency on the gradient is not taken into account for this simulation. A peak current of about 50 A can be reached with this conditions. The particles in the temporal distribution from about -9 ps to about

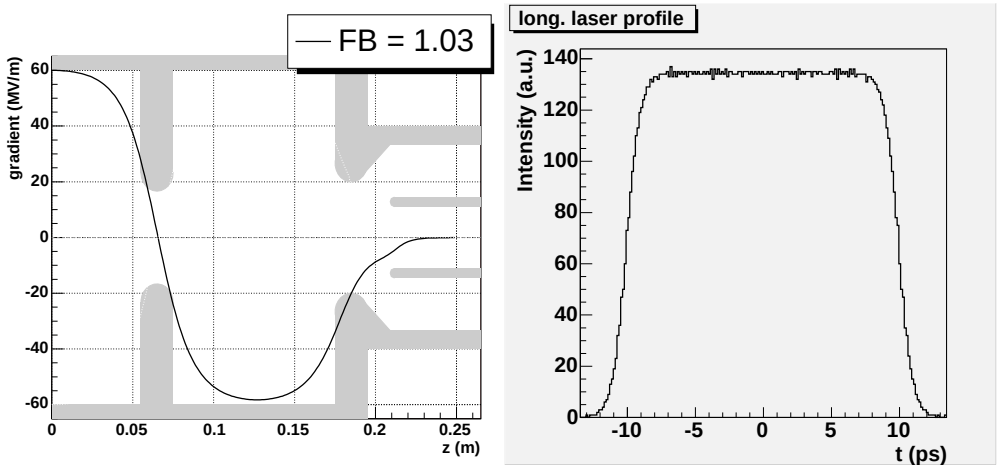

(a) (b)

Figure 2.6: *An example for the accelerating field $E(z)$ with a field balance (FB) = 1.03 (a) and a longitudinal laser distribution with a duration of 20 ps and 2 ps rise and fall times (b) used in simulations.*

parameter	symbol	value	unit
mean momentum	$< p >$	6.87	MeV/c
momentum spread	p_{rms}	23.1	keV/c
bunch length	z_{rms}	1.79	mm
bunch duration	t_{FWHM}	20.4	ps
longitudinal emittance	ε_z	5.99	π keV/c mm

Table 2.1: *Properties of the longitudinal phase space shown in figure 2.5*

3 ps belong to a small momentum range from 6.87 to 6.89 MeV/c. They produce the peak in the momentum distribution, due to the non-linearity in the longitudinal phase space. At about -9 ps there is a momentum spread minimum in the longitudinal phase space of the beam corresponding to a slice momentum spread smaller than 1 keV/c. For the measurement it is of major interest to prove this minimum in the uncorrelated momentum spread obtained in simulations and to understand the corresponding beam dynamics. This example shows the requirements to the resolution of the longitudinal phase space measurement system. The maximum slice momentum spread is around 5 keV/c, the minimum is below 0.2 keV/c in this example, where the width of a slice was chosen to be 0.16 ps. The minimum in the momentum spread is developing directly after the emission process and is caused

by effects of mirror charge and space charge forces. For certain momenta

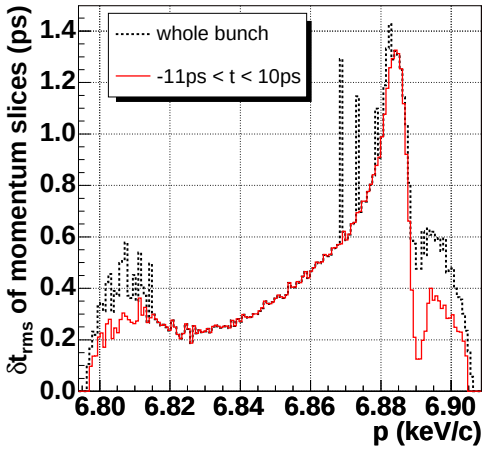

Figure 2.7: *The rms value of the duration for particles with equal momentum.*

within the bunch the duration is below a ps. In figure 2.7 the rms duration is shown as a function of the momentum for the longitudinal phase space shown in figure 2.5. The momentum slice used for this calculation has a width of 0.8 keV/c. The longitudinal phase space of the gun for the phase of maximum momentum gain is not linear. For the solid red curve the head and tail particles of the bunch have not been taken into account, but only the particles for $t = $-11 ps to $t = 10$ ps have been considered. This was done, because two separate longitudinal slices (for example for a momentum of 6.89 MeV/c at about -12 ps and -8 ps) contain particles with this momentum, which would lead to a strong overestimate of the duration. The graph gives an idea about the needed temporal resolution for longitudinal phase space measurement. To measure these properties is a very demanding task as it will be shown in chapter 4. Only when a temporal resolution in the sub-picosecond range and a momentum resolution of about a keV/c is reached the longitudinal emittance can be determined correctly.

Figure 2.8 shows the simulated distribution of the electron bunch in the longitudinal phase space for the same conditions as in figure 2.5, but a charge of 100 pC. The reduction of the charge by a factor of ten reduces the influence of space charge forces and thus the momentum spread, the slice momentum spread as well as the bunch length. Along the whole bunch the slice momentum spread is below 1 keV/c, in the minimum it is 0.1 keV/c. The shape of the longitudinal phase space is mainly defined by the RF field. The peak current is clearly decreased compared to the 1 nC case.

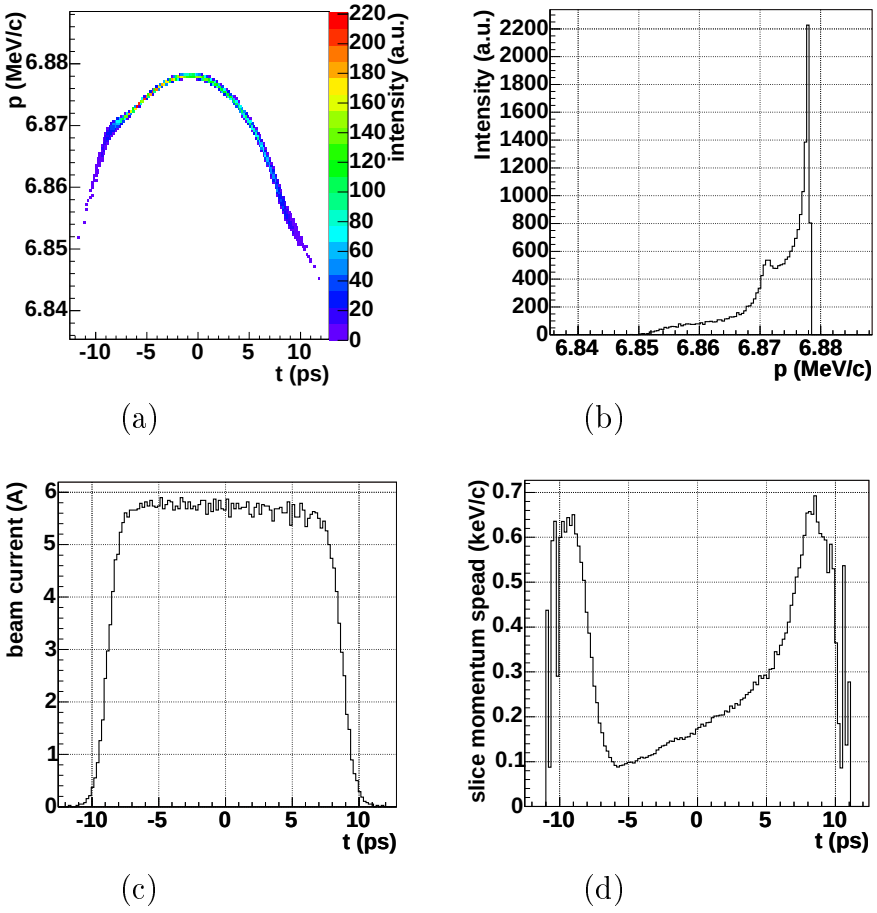

Figure 2.8: *Simulated longitudinal phase space distribution (a), momentum distribution (b), charge density distribution (c) and rms slice momentum spread (d) half a meter downstream the photocathode for the phase of maximum mean momentum gain. The simulation conditions applied to ASTRA were: 60 MV/m at the cathode, 100 pC bunch charge, a maximum main solenoid field of 176 mT, a flat top longitudinal laser distribution of 20 ps with rise- and falltime 2 ps and a transverse laser diameter of the beam of 2 mm.*

Chapter 3

Typical methods of longitudinal phase space measurements

In this section typical methods to measure the longitudinal phase space and its projections, momentum distribution and temporal distribution, are described.

3.1 Measurement of the momentum distribution

3.1.1 Spectrometer dipole magnet

A spectrometer dipole magnet is a standard device in accelerator physics for the measurement of the mean momentum and momentum distribution of the beam. Charged particles with different momenta (p) passing the dipole magnet are deflected onto different curves, electrons with lower momentum are deflected more strongly, according to:

$$r = \frac{p}{eB_0}, \tag{3.1}$$

with r the deflection radius, c the velocity of light, e the elementary charge and B_0 the magnetic field strength. Thus the momentum can be determined by: $p = \frac{e}{\alpha} \int B(l) dl$, with α the deflection angle and $B(l)$ the magnetic field along the orbit. Also at PITZ spectrometer dipole magnets are used to measure the beam momentum distribution. For an optimized setup a high resolution can be reached, as discussed in more detail in section 4.1.1. Since at PITZ dipole magnets are only used for measurement purposes the degree

of freedom for the optimization of the measurement is higher than for example at FLASH, where the dipoles of the bunch compressors are used as spectrometer.

3.2 Measurement of the longitudinal bunch distribution

The measurement of the longitudinal beam distribution is a critical issue for FELs, therefore different measurement procedures with a resolution down to about 100 fs exist. This resolution in the sub-picosecond range is mandatory for the compressed beams. A distinction is drawn between direct measurements in the time domain and measurements in the frequency domain.

3.2.1 Spectral techniques

Spectral bunch length measurement techniques use coherent radiation (like coherent transition, diffraction or synchrotron radiation) or Smith-Purcell radiation. The spectral distribution produced by these radiators can be measured by various instruments, like Martin-Puplett interferometer [Fro05] or grating spectrometers. A big drawback of the spectral techniques is the ambiguity of the inversion process which makes the reconstruction of the complete temporal distribution impossible in the general case. In [Del08] was shown that the spectroscopy of *c*oherent *t*ransition *r*adiation (CTR) is capable to detect the presence of structures in the bunch down to optical wavelength. In this indirect method CTR is produced on an off-axis screen by a single electron bunch kicked out of the bunch train by a fast kicker. The radiation is dispersed by a sequence of reflecting blazed gratings and detected by pyroelectric line arrays with a fast readout. Measurements in the range from $3\,\mu\text{m} < \lambda < 65\,\mu\text{m}$ have been presented in [Sch08].

3.2.2 Electro-optical sampling

The electro-optical sampling (EOS) is used to measure the longitudinal charge distribution with a resolution in the order of about 100 fs [Casa05]. It is a non-invasive method and single-shot measurements of individual bunches are possible.

A linear polarized laser pulse is sent through an electro optical crystal. The electric field of the relativistic bunch induces an optical birefringence in the non-linear crystal (e.g. gallium-phosphide). In the crystal the linear polarization of the laser pulse is transformed to an elliptical one. The ellipticity

of the polarization is proportional to the electric field of the electron bunch. The elliptical polarization can be converted into an intensity modulation for example by a polarizer.

For an application at low energies one has to take into account that, in general, the transverse electric field is collapsed into a transverse angle of $\frac{1}{\gamma}$. For a non-linear crystal at a distance x from the beam, the temporal resolution is limited by the time it takes the transverse field to pass the detector $\delta t \approx \frac{2x}{\gamma\beta c}$. For 7 MeV/c and a distance of $x = 10$ mm a resolution of approximately 4.9 ps is reached. To overcome this problem one could place the non-linear crystal directly into the electron beam and eliminate the resolution limiting distance x [Dow]. Of course, the method becomes destructive for this case. A major problem of this approach is the small peak current in the injector compared to the compressed beam used for the FEL process. In order to reach a measurable change the thickness of the crystal has to be increased. A thick crystal on the other hand will absorb the beam and thus change the temporal structure and dilute the temporal resolution.

3.2.3 Transform charge to light and use a streak camera

One of the most well-known techniques of bunch length measurements in the time domain is to measure the temporal distribution of light pulses induced by the electron bunch using a streak camera. For this technique one has to ensure that the response time of the applied radiator is significantly shorter than the electron bunch, meaning the temporal information has to be conserved during the transformation of the electron bunch into a light pulse. So, the response of the transformation effect and tranformation material has to be fast. This means, to be able to measure a bunch durration of about 20 ps and analyse the longitudinal distribution of such a bunch in detail, a responds time of the material clearly below a picosecond is required. This is mainly not the case for fluorescence-materials like YAG screens, whose response time is in the order of several tens of ns[Gra98]. In storage rings, CSR is used to analyse the bunch profile. Optical transition radiators (OTRs) are commonly used as screens to measure the transverse beam size. Since optical transition radiation is a surface effect its temporal resolution is high. But the number of photons is small, especially at low energies. Therefore at PITZ it was decided to use Cherenkov radiators, where the number of emitted photons at low electron energies is much higher than for OTR screens. The created light pulse has to be imaged onto a narrow entrance slit of the streak camera.

Streak camera

A streak camera is a device used to measure the temporal distribution of light pulses and is typically used in laser labs. Different types of streak cameras are available with a resolution down to about 500 fs over a large wavelength range. Beside the possibility to measure the temporal distribution, a spatial distribution in one dimension (matching through a small slit) could be measured simultaneously. The working principle is shown in figure 3.1. The

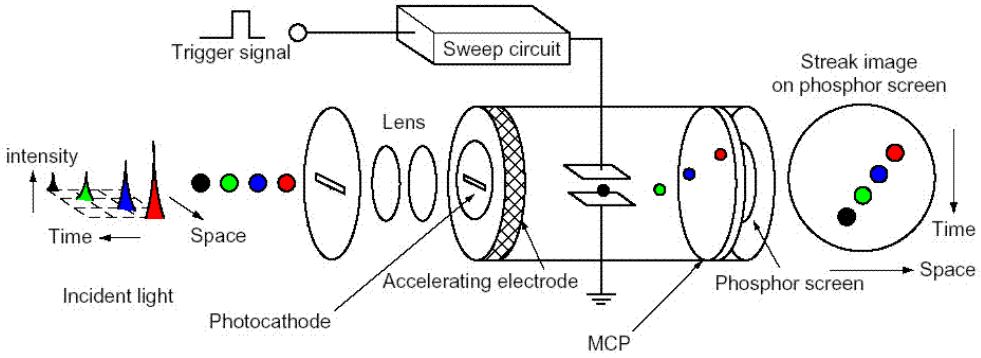

Figure 3.1: *Working principle of a streak camera. Source: [Ham04]*

light entering through the adjustable, narrow slit is imaged by an internal optics onto a photocathode. The generated electrons are accelerated, and in the streak tube they are deflected transversely depending on their arrival time. Thus the temporal distribution is converted into a spatial one. The number of electrons is amplified by a multi-channel plate (MCP) before they are transformed to light by a phosphor screen, which is observed by a CCD camera. At PITZ the HAMAMATSU streak camera C5680 [Ham04] is used. It delivers a temporal resolution of 2 ps.

3.2.4 RF deflector

The RF deflector is a high resolution device to measure the longitudinal distribution of the bunch. A transverse RF mode in the cavity deflects the bunch in transverse direction such that a different field strength is applied to the electrons arriving at different times and thus they are deflected differently. Consequently the longitudinal beam distribution is transformed into a transverse one, which is observed on a subsequent screen. The RF deflector used at FLASH reaches a resolution of down to 30 fs [Röh08]. The initial transverse distribution in the deflection direction influences the resolution of

this measurement. A strong decrease of the beam size in order to improve the measurement may cause strong space charge effects, especially for small energies. In the PITZ2 design an RF deflector is foreseen [Kor07]. The RF deflector is a destructive measurement method, but since there are long pulse trains used at PITZ and the European XFEL, a few pulses out of the train can be used for the measurement with the RF deflector. To avoid disturbance of the bunch before and afterwards a filling time smaller than the bunch separation is required. Using a kicker magnet these pulses can be kicked onto an off-axis screen, while the others pass undisturbed. In combination with other diagnostics the RF deflector offers also the possibility to measure slice parameters of the bunch, like slice emittance.

3.3 Measurement of the longitudinal phase space

In order to measure the longitudinal phase space, a combination of the measurement systems for momentum measurement with the system to measure the longitudinal distribution is required. The combination of the RF deflector and spectrometer dipole magnet would mean: the RF deflector transforms the longitudinal distribution into a transverse one and the spectrometer transforms afterwards the momentum distribution in a transverse distribution in the orthogonal plane.

The spectrometer can also be combined with the streak method by placing the radiator in the dispersive section after the magnet. The momentum distribution is then imaged onto the entrance slit of the streak camera as spatial distribution. Both methods will be discussed in the next chapter.

Chapter 4

Development and analysis of diagnostics to determine the longitudinal phase space distribution of the bunch at PITZ

4.1 Overview of longitudinal diagnostics at PITZ

4.1.1 Momentum measurement system

In the PITZ2-setup (Figure 2.4) three spectrometer dipoles and their corresponding dispersive arms are foreseen. The first spectrometer is situated downstream the gun (the so-called Low-Energy-Dispersive-Arm (LEDA)) and two further dipole magnets are located downstream the booster cavity. The design of the two High-Energy-Dispersive-Arms (HEDAs) differs in the number of allowed pulses. In the first High-Energy-Dispersive-Arm (HEDA1) the number of pulses is limited to 960 pulses per second for a beam energy of 40 MeV/c. In contrast the second one (HEDA2) has to allow running with the full number of pulses which are 72000 pulses per second (7200 pulse per train with a repetition rate of 10 Hz). A fourth dipole magnet (a modified HERA corrector magnet), was used as a spectrometer magnet in the PITZ beamline for a long time. In PITZ1 it was used as a gun spectrometer until the real dipole arrived and in PITZ1.5, 1.6 and 1.7 it was and is used as High-Energy-Dispersive-Arm until HEDA2 is ready, but the maximum measurable momentum is limited to 16 MeV/c.

The motion of an electron with the initial coordinates $x_0, x'_0, y_0, y'_0, l_0, \delta_0$ (described in section 2.2.3) through a dipole magnet can be described by

equation 2.4, with

$$R = \begin{pmatrix} R_{11} & R_{12} & 0 & 0 & 0 & R_{16} \\ R_{21} & R_{22} & 0 & 0 & 0 & R_{26} \\ 0 & 0 & R_{33} & R_{34} & 0 & 0 \\ 0 & 0 & R_{43} & R_{44} & 0 & 0 \\ R_{51} & R_{52} & 0 & 0 & 1 & R_{56} \\ 0 & 0 & 0 & 0 & 0 & 1 \end{pmatrix}, \tag{4.1}$$

with x being the dispersive direction. Matrix elements equal to zero denote that the device (in this case the dipole magnet) does not cause a correlation between the corresponding axes in the phase space, to first order. This means for example that the momentum of the particle passing the dipole stays unchanged, to first order.The electron position in dispersion direction at a screen in the dispersive arm (DA) is given by:

$$x_{DA} = R_{11}x_0 + R_{12}x'_0 + R_{16}\delta. \tag{4.2}$$

This means the position (displacement from the design orbit) of a particle on a screen in the dispersive section (x_{DA}) depends on the initial position (displacement from the design orbit) x_0, angular divergence x'_0 and momentum deviation δ of this particle. The influence of the three parameters is defined by the matrix elements (R_{11}, R_{12} and R_{16}). In order to measure the momentum of one or several particles, the influence of the initial position and divergence should be small compared to the momentum contribution:

$$R_{11}x_0 + R_{12}x'_0 \ll R_{16}\delta. \tag{4.3}$$

For a dipole magnet with a drift space upstream (before) the dipole magnet and in the dispersive arm (DA) (with the lengths L_{before} and L_{DA}) the matrix elements have been determined by the multiplication of the corre-

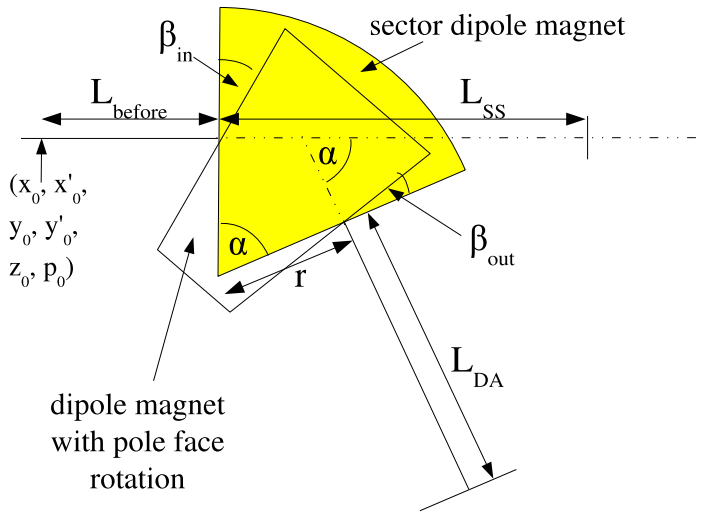

Figure 4.1: *Important parameters of a a dipole spectrometer.*

sponding transport matrices [BR98]:

$$
\begin{aligned}
R_{11} &= \cos\alpha(1+\tan\beta_{out}\cdot\frac{L_{DA}}{r}+\tan\beta_{in}\cdot\frac{L_{DA}}{r}) \\
&\quad +\sin\alpha(\tan\beta_{in}+\tan\beta_{out}\cdot\tan\beta_{in}\cdot\frac{L_{DA}}{r}-\frac{L_{DA}}{r}), \\
R_{12} &= L_{before}\cdot R_{11}+\cos\alpha\cdot L_{DA}+\sin\alpha(r+\tan\beta_{out}\cdot L_{DA}) \\
&= \cos\alpha(L_{before}+\tan\beta_{out}\cdot L_{before}\cdot\frac{L_{DA}}{r}+L_{DA}+L_{before}\cdot\tan\beta_{in}\cdot\frac{L_{DA}}{r}) \\
&\quad +\sin\alpha(r+\tan\beta_{in}\cdot L_{before}+\tan\beta_{out}\cdot L_{DA} \\
&\qquad +\tan\beta_{out}\cdot\tan\beta_{in}\cdot L_{before}\cdot\frac{L_{DA}}{r}-L_{before}\cdot\frac{L_{DA}}{r}), \\
R_{16} &= r\cdot(1-\cos\alpha)+L_{DA}\cdot(\sin\alpha+\tan\beta_{out}-\tan\beta_{out}\cdot\cos\alpha),
\end{aligned}
\tag{4.4}
$$

whereα is the bending angle, β_{in} and β_{out} are the entrance and exit pole face rotating angles and r is the bending radius of the design trajectory through the dipole. According equation 3.1 the momentum of the particle($p=\frac{reB_0}{c}$) along the design orbit with a fixed bending radius depends on the magnetic field of the dipole magnet.

The variables describing the dipole magnet are shown in figure 4.1. Equation 4.2 describes the behavior of a single particle. For a bunch of particles the distribution on the screen $f(x_{DA})$ can be described by the convolution of

the functions $g(x_0, x_0')$ and $h(\delta)$:

$$f(x_{DA}) = g(x_0, x_0') * h(\delta), \tag{4.5}$$

where $g(x_0, x_0')$ describes the influence of the initial transverse distribution and divergence distribution (in x-plane, the dispersion direction) on the distribution on the screen in the dispersive section. In case of a mono-energetic beam the distribution on the screen would be $f(x_{DA}) = g(x_0, x_0')$. The function $h(\delta)$ describes the influence of the momentum distribution of the electron bunch on the resulting distribution on the screen in the dispersive section. For a beam with zero size and divergence (in dispersion direction) the distribution on the screen would correspond exactly to the momentum distribution.

It should be pointed out, that a proper design of a high resolution spectrometer dipole magnet defines a reference position, where the beam has to be focused or cut (by a slit) in order to reach a high resolution. This means the spectrometer can only reach a high resolution with a proper usage. The reference position can be defined assuming the magnet is turned off. The electron position at a certain position in the straight section (SS) is: $x_{SS} = 1 \cdot x_0 + (L_{before} + L_{SS}) \cdot x_0'$. To induce a relation between the beam size on the screen in the straight section and the influence of the transverse beam size and divergence in the dispersive section the following condition has to be fulfilled:

$$\begin{aligned} R_{11} \cdot x_0 + R_{12} \cdot x_0' &= n \cdot x_{SS} \\ R_{11} \left(x_0 + \frac{R_{12}}{R_{11}} \cdot x_0' \right) &= n \left(x_0 + (L_{before} + L_{SS}) \cdot x_0' \right) \end{aligned} \tag{4.6}$$

For a mono-energetic beam the beam size (in dispersive direction) in the dispersive section is n times larger than on the reference screen in the straight section. This magnification factor is given by R_{11} ($n = R_{11}$). This means the distance from the initial position (z_0) to the reference position is:

$$L_{before} + L_{SS} = \frac{R_{12}}{R_{11}} \tag{4.7}$$

The beam distribution on the reference screen defines the impulse response [1] of the dipole magnet spectrometer.

[1] The impulse response of a system describes the output signal for very short input signal (a Kronecker delta), in our case this would correspond to a mono-energetic beam.

4.1.2 Bunch length measurement system

In the PITZ2-setup (Figure 2.4) an RF deflector is foreseen for a highly resolved measurement of the longitudinal distribution. It could also be used to determine slice parameters like slice emittance. The transverse RF cavity and measurements planned will not be discussed in detail in this thesis. Some design considerations are summarized in [Kor07].

In the current setup (PITZ 1.7 (Figure 2.3)) there are two screen stations used for the measurement of the longitudinal bunch distribution: LOW.Scr3 downstream the gun and HIGH1.Scr2 downstream the booster. The screen stations contain different radiators transforming the electron bunch into a light pulse with similar temporal distribution. These radiators are either OTR screens or Cherenkov radiators, typically silica aerogel. Cherenkov light is emitted at a certain angle, depending on the electron energy and the refractive index of the radiator. The light will leave the radiator as a cone, according to the Cherenkov angle and Snell's Law, under the angle α:

$$\alpha = arcsin\left(\sqrt{n^2 - \frac{1}{\beta^2}}\right), \tag{4.8}$$

for a particle traveling perpendicular to the exit surface. The light distribution is imaged onto a streak camera, which measures the longitudinal distribution of the pulse. When the optical system is designed such that the complete cone is collected (this requires a high aperture input optics) and transported to the streak camera, it is called a full cone scheme. To determine the resolution of the system, the three parts:

- the radiator (discussed in section 4.2),
- the optical transmission line (discussed in section 4.4) and
- the streak camera (discussed in section 4.5)

are analysed independently.

4.1.3 System for measurements of the longitudinal phase space distribution

As mentioned already in section 3.3 the combination of the measurement system for longitudinal and momentum distributions allows the measurement of the correlation between both axes, the distribution of the electron bunch in the longitudinal phase space. These kind of measurements are realized at PITZ by including a Cherenkov radiator or an OTR screen in the beam orbit

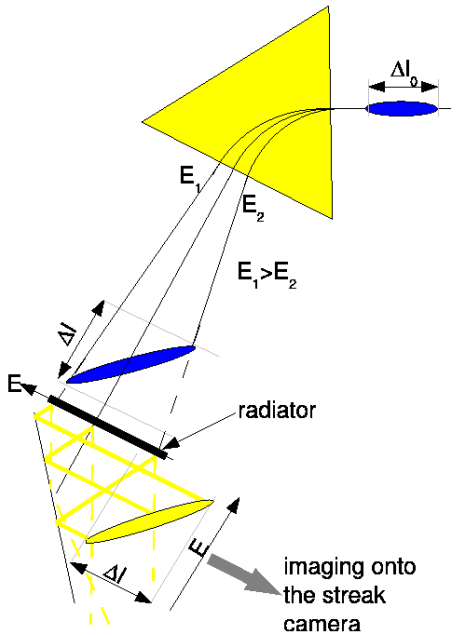

Figure 4.2: *The measurement of the longitudinal phase space distribution realized at PITZ uses a dipole spectrometer and a Cherenkov radiator in the dispersive arm.*

in the dispersive arms (as shown in figure 4.2). This means the spectrometer dipole generates a transverse distribution corresponding to the momentum distribution, which is transformed into a light pulse with similar longitudinal and transverse properties. This light distribution is imaged onto the streak camera entrance slit. The transverse distribution corresponding to the momentum distribution is imaged along the entrance slit of the streak camera. The streak camera transforms the temporal distribution into a transverse distributions, which is orthogonal to the entrance slit, which restores the momentum distribution. For an extended object like the momentum spectra, it is not possible to transport light under large angles without remarkable light losses for the off-axis points. Therefore at PITZ the "partial cone"-approach was introduced, this means only a small segment of the Cherenkov cone [Lip04] is imaged onto the streak camera.

For this method it has to be taken into account that the longitudinal distribution will change when the bunch passes the dipole magnet. The longitudinal distance of a particle to the reference particle of the bunch changes from l_0 the initial position before the dipole spectrometer to l_{DA} at the screen in the dispersive arm. The difference of l_{DA} and l_0 depends on the initial transverse position of the electron, its divergence and its longitudinal momentum

and can be determined according to equation 2.4 by:

$$l_{DA} = R_{51}x_0 + R_{52}x'_0 + l_0 + R_{56}\delta, \tag{4.9}$$

with the matrix elements received from the multiplication of the transport matrices that describes the drift before dipole magnet, the entrance pole face rotation, a sector magnet, the exit pole face rotation and the drift in the dispersive arm [BR98]:

$$\begin{aligned} R_{51} &= \sin\alpha + \tan\beta_{in} - \cos\alpha \cdot \tan\beta_{in}, \\ R_{52} &= L_{before} \cdot R_{51} + r(1 - \cos\alpha), \\ R_{56} &= -r \cdot \alpha + r\sin\alpha + \frac{r \cdot \alpha + L_{before} + L_{DA}}{\gamma^2}, \end{aligned} \tag{4.10}$$

where γ is the Lorentz factor. Equivalent to equation 4.3, the condition:

$$R_{51}x_0 + R_{52}x'_0 \ll l_0. \tag{4.11}$$

has to be fulfilled to measure a highly resolved longitudinal distribution in the dispersive arm. Also here a reference position in the straight section can be defined. R_{56} is the momentum compaction factor which describes the change of the longitudinal position of a particle within the bunch due to the difference in the path length through the dipole caused by the difference in momentum. It causes a shearing of the longitudinal phase space distribution (which describes the correlation of momentum and longitudinal position in the bunch). It does not influence the resolution of the measurement, since it can be corrected simply by shearing the distribution back.

Another approach to determine the distribution of the bunch in the longitudinal phase space is the transformation of the longitudinal distribution into a transverse one by using an RF deflector and deflect the beam afterwards in the other transverse direction (perpendicular) by the spectrometer dipole (as shown in figure 4.3). This measurement is foreseen in the HEDA2. Since the longitudinal distribution was transformed into a transverse one before the beam enters the spectrometer, the change of the longitudinal distribution in the magnet is irrelevant for this method. Instead the development in the non-dispersive direction has to be considered. Thus the transverse position of a particle on the screen in the dispersive arm in non-dispersive direction is defined by: $y_{DA} = R_{33} \cdot y_0 + R_{34} \cdot y'_0$, with the transport matrix

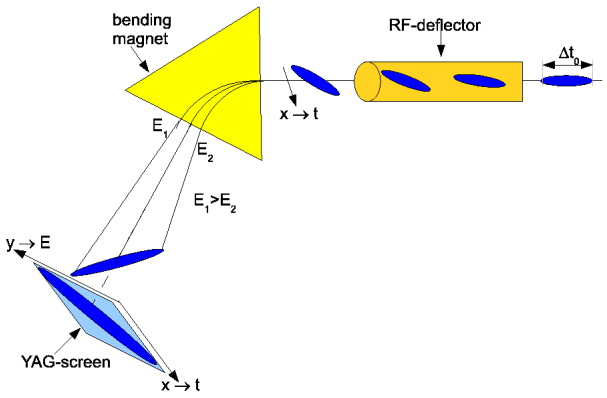

Figure 4.3: *Measurement of the longitudinal phase space distribution using an RF deflector and a spectrometer dipole.*

elements [BR98]:

$$\begin{aligned} R_{33} &= 1 + \frac{\alpha \cdot L_{DA}}{r} \tan(\beta_{in} - \psi_{in}) \tan(\beta_{out} - \psi_{out}) - \frac{L_{DA}}{r} \tan(\beta_{out} - \psi_{out}) \\ &\quad - \tan(\beta_{in} - \psi_{in}) \cdot (\frac{L_{DA}}{r} + \alpha), \\ R_{34} &= L_{before} + \frac{\alpha \cdot L_{DA} \cdot L_{before}}{r} \tan(\beta_{in} - \psi_{in}) \tan(\beta_{out} - \psi_{out}) \\ &\quad - \frac{L_{DA} \cdot L_{before}}{r} \tan(\beta_{out} - \psi_{out}) - \frac{L_{DA} \cdot L_{before}}{r} \tan(\beta_{in} - \psi_{in}) \\ &\quad - \alpha \cdot L_{before} \tan(\beta_{in} - \psi_{in}) + \alpha \cdot r - L_{DA} \cdot \alpha \tan(\beta_{out} - \psi_{out}) + L_{DA}, \end{aligned} \tag{4.12}$$

with ψ being the correction term resulting from the spatial extent of fringe fields [BR98]:

$$\psi = \kappa_1 \frac{h}{r} \cdot \frac{1 + \sin(2\beta)}{\cos\beta} \cdot (1 - \kappa_1 \kappa_2 \frac{h}{r} \tan\beta), \tag{4.13}$$

where κ_1 and κ_2 are fringe field integrals and h is the total gap of the magnets. The transverse shift in the reference trajectory is given by [BR98]:

$$\Delta x = \frac{1}{cos^2\beta} \frac{h^2}{r} \kappa_0, \tag{4.14}$$

where κ_0 is an integral used to calculate the reference orbit displacement by the fringe field.

4.1.4 Overview of screen stations with optical readout for streak camera measurements at PITZ

Table 4.1 gives an overview of the existing and planned screen stations which are or will be equipped with radiators whose light is imaged onto the streak camera and whose main task is the measurement of the longitudinal phase space distribution and/or its projections. At all these screen stations the

screen station	momentum range (MeV/c)	measurement task	radiator	F/P
LOW. Scr3	4 - 7	long. distr. transverse distr.	aerogel/OTR YAG	F
DISP1. Scr1	4 - 7	momentum distr. long. phase space distr.	YAG aerogel	 P
HIGH1. Scr2	4 - 40	long. distr. transverse distribution slice emittance*	aerogel/OTR YAG/OTR aerogel/OTR	F P
DISP2. Scr1/2	4 - 40	momentum distr. long. phase space distr. slice emittance	YAG/OTR aerogel OTR YAG	 P F*
DISP3.* Scr1	4 - 40	momentum distr. long. phase space distr. slice emittance	YAG/OTR aerogel OTR YAG	 P F

Table 4.1: *Overview about the current and planned screen stations for the analysis of the properties of the distribution (distr.) of the bunch in the longitudinal (long.) phase space at PITZ. Their physical tasks, radiators and optical input schemes (F: full cone, P: partial cone) are shown. Everything marked with * is not realized in the current state (PITZ 1.7).*

electron beam diagnostics is based on light production by interaction of the particles with matter. In the table the radiators and related optical input schemes are shown for all screen stations in use or under development.

4.2 Screen stations for bunch length measurements

4.2.1 Analysis and modification of LOW.Scr3

The design considerations of LOW.Scr3 were discussed in [Lip04]. It contains a YAG screen to determine the transverse distribution of the bunch and three radiators for bunch length measurement: an OTR screen and two Cherenkov radiators (quartz and aerogel). Mainly the aerogel with an index of refraction of $n = 1.03$ and a thickness of $d = 2\,\mathrm{mm}$ was used for bunch length measurement, while the others were used mainly for methodical studies. During the design an electron momentum of 4-4.5 MeV/c was considered. Meanwhile the momentum of the injector has been increased up to about 6.5 MeV/c and even higher momentum is expected in the near future. The left graph in figure 4.4 shows the momentum dependence of the emission angle for aerogel with three different indices of refraction compared to the emission angle of OTR light (discussed in section 4.2.2).

The optical transmission line which images the distributions onto the streak camera limits the transportable angle. In section 4.4 the design of the optical transmission line from the radiator to the streak camera is discussed in detail, it contains a figure (4.41), which shows the imaging elements of the optical transmission. For LOW.Scr3 the first lens (Biotar) limits the emission angle. For an object point on the optical axis the maximum transportable emission angle is 13.4°, which corresponds to the Cherenkov angle of photons produced by electrons with a momentum of approximately 6 MeV/c (for $n = 1.03$). For an object point with only 1 mm distance to the optical axis the limiting angle to transport the whole Cherenkov cone reduces to about 12.5°. This means for a beam with 5 MeV/c and an off-set of 1 mm from the optical axis only a part of the cone would be transported to the streak camera. For momenta above 6 MeV/c only the partial cone from off-axis points can reach the streak camera, while light emitted from an object point on the optical axis cannot pass the entrance pupil. This already critical condition can only be reached for a perfect alignment. To overcome this undesired reduction of the collection efficiency of the light either the optical transmission line has to be modified or the index of refraction of the Cherenkov radiator has to be reduced. A refractive index of $n = 1.008$ is used to reduce the maximum emission angle of the radiator to 7.3°. With this Cherenkov radiator, the Biotar images the full cone of objects with a displacement from the optical axis of up to 7 mm. The drawback of the reduction of the refractive index to 1.008 is the increase of the threshold for the Cherenkov effect ($\beta > \frac{1}{n}$) to

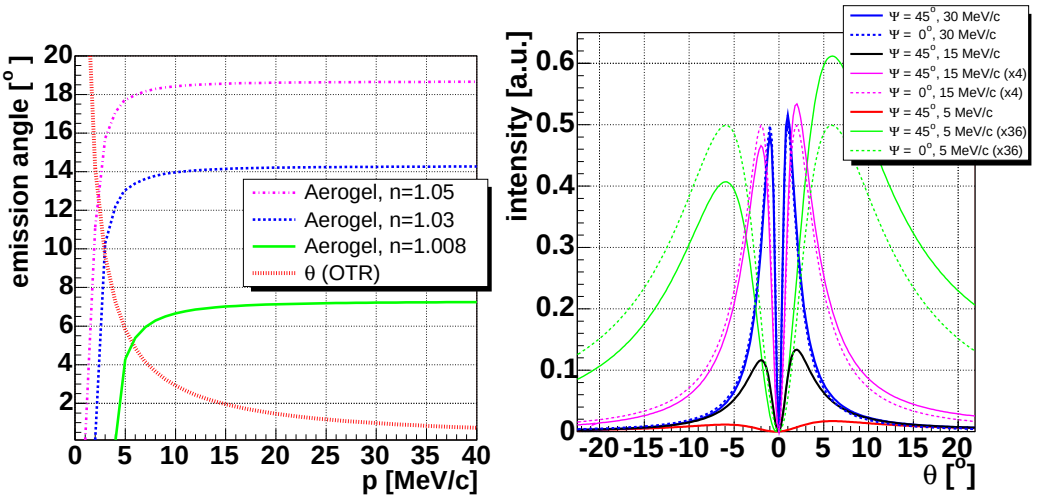

(a) (b)

Figure 4.4: *Emission angle of OTR and silica aerogel radiators with different refractive indices depending on the electron beam momentum (a). While the emission angle of photons produced by the Cherenkov effect is sharply peaked for a given momentum and a homogenous refractive index, for optical transition radiation an angular distribution (shown in graph (b) for electron momenta of 5 MeV/c, 15 MeV/c and 30 MeV/c and the angle of the electron beam design orbit to the normal of the boundary of the OTR $\psi = 0°$ (dotted line) and $\psi = 45°$ (solid line)) is produced.*

about 4 MeV/c.

The determination of the resolution of a Cherenkov radiator is described in detail in [Lip05-1]. The resolution depends mainly on the thickness and the index of refraction of the radiator. The calculation also considers a thin (10 μm) aluminium foil in front of the aerogel (to avoid particles of the aerogel in the vacuum tube). Figure 4.5(a) shows the rms value of the temporal resolution up to 10 MeV/c for aerogel with $n = 1.03$ with a thickness of 2 mm, as it was used in the PITZ1 setup. The thickness of the aerogel with $n = 1.008$ and 1.05 were adjusted such that all of them deliver about the same temporal resolution within the useable energy range (4-7 MeV/c). For silica aerogel with $n = 1.008$ a thickness of $d = 5$ mm is needed to reach a similar temporal resolution as for $n = 1.03$ with thickness of $d = 2$ mm. The number of photons within a wavelength range λ_1 and λ_2 emitted by an electron passing the Cherenkov radiator can be calculated by[Jel58]:

$$N_{Ch} = 2\pi \cdot \alpha_{QED} \cdot d \cdot \left(\frac{1}{\lambda_1} - \frac{1}{\lambda_2}\right) \cdot \left(1 - \frac{1}{\beta^2 n^2}\right), \qquad (4.15)$$

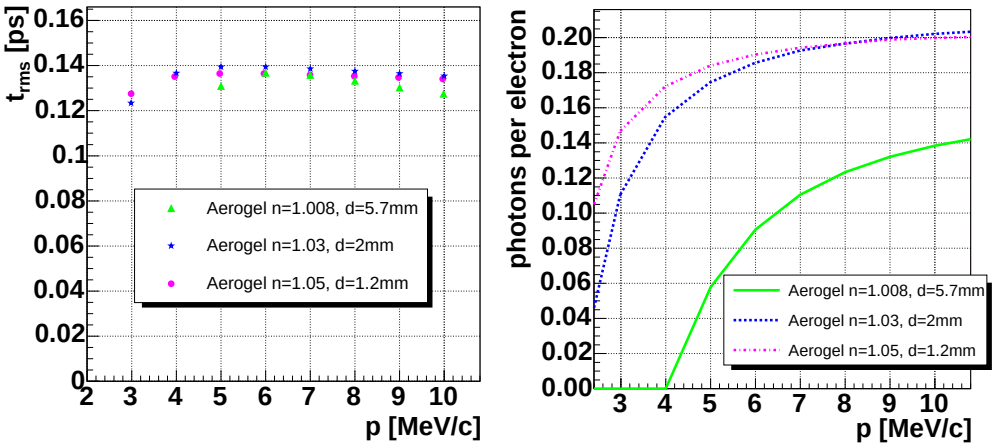

(a) (b)

Figure 4.5: *The rms value of the expected temporal resolution (a) and the number of emitted photons per electron (b) of different radiators depending on the electron beam momentum.*

where d is the thickness of the Cherenkov radiator and $\alpha_{QED} = \frac{e^2}{4\pi\epsilon_0 \hbar c} \approx 1/137$ is the fine structure constant. Equation 4.15 shows a linear relationship between the number of produced photons and the thickness of the material (as long as β stays constant during the passage). Thus the aerogel radiator should be thick, but on the other hand an increase of the thickness leads to a deterioration of the temporal resolution (as it will be shown in the next section in figure 4.7) and an increase of the deposited energy. Figure 4.5(b) shows the expected number of photons per electron for the radiator within a wavelength range from 400 to 750 nm as a function of the beam momentum. The number of the produced photons for $n = 1.008$ and $d = 5\,\text{mm}$ is smaller than for $n = 1.03$ and $d = 2\,\text{mm}$, but for $n = 1.008$ the whole cone of the Cherenkov light is transported compared to $n = 1.03$ and thus the effective illumination is higher. With the new setup a single electron bunch with a length of about 10 ps FWHM could be measured at an energy of 6.6 MeV/c for a streak camera slit width of 0.05 mm.

4.2.2 Design consideration of HIGH1.Scr2

The design of the screen station HIGH1.Scr2, which is located downstream the booster cavity is based on that of LOW.Scr3, but the usage of higher energies has to be taken into account. The bunch length behind the booster should be measurable with the booster on and off, to study the influence of

the acceleration process on the longitudinal distribution.

For bunch length measurements an OTR screen and silica aerogel will be discussed on their usability in the momentum range 4 to 40 MeV/c. Transition radiation was predicted by Ginzburg and Frank in 1946 [Gin46], and it occurs when a charged particle passes the boundary of two media of different dielectric constant.

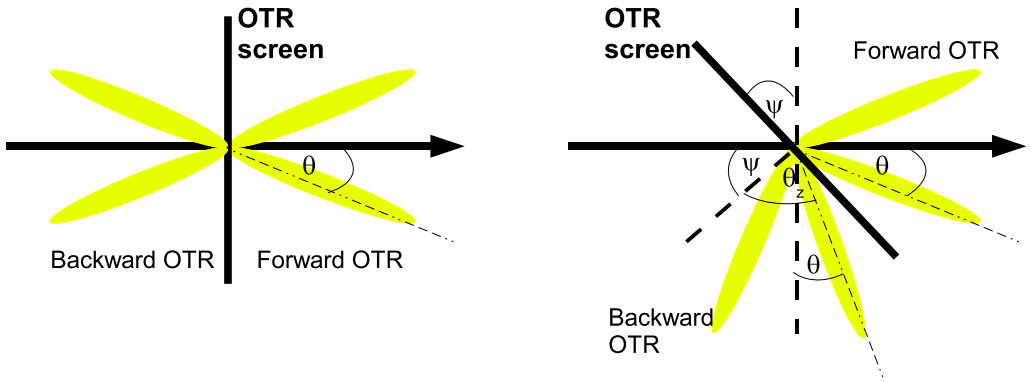

Figure 4.6: *Two possibilities of usage of OTR-screens*

OTR appears at the entrance and exit boundary the particle passes. Figure 4.6 shows the forward and backward radiation. The angle of the electron beam design orbit to the normal of the boundary of the OTR (ψ) is $\psi = 0°$ in the left graph and $\psi = 45°$ in the right one. The OTR light is emitted as an angular distribution, θ indecates a certain emission angle. In figure 4.4(a) the emission angle θ for optical transition radiation which is shown presents the angle of maximum light intensity. It can be determined by: $\theta_{peak} = \frac{1}{\gamma}$. For the comparison with Cherenkov light, it has to be taken into account that the optical transition radiation is not emitted at a fixed angle. This means that the angular distribution has a significant width and that also a significant part of the OTR is emitted at larger angles. The angular distribution of transition radiation depends on the particle energy and the angle of incidence ψ. In figure 4.4(b) the angular distribution for different electron energies within the wavelength range from $\lambda_1 = 400\,\text{nm}$ to $\lambda_2 = 750\,\text{nm}$ are shown. It was calculated by [Gin46, Hon00]:

$$\frac{dN}{d\Omega} = \frac{\alpha_{QED}}{\pi} \left(\frac{\beta cos\psi (sin\theta_z - \beta cos\varphi sin\psi)}{(1 - \beta sin\theta_z cos\varphi sin\psi)^2 - \beta^2 cos^2\theta_z cos^2\psi} \right)^2 ln\left(\frac{\lambda_2}{\lambda_1}\right), \tag{4.16}$$

where ψ is the incident angle of the electron with respect to the normal of the boundary, φ is the angle between the incident plane and the observation

plane and θ_z ($\theta_z = 90° + \theta - \psi$) is the angle at which the light intensity should be anaysed with respect to the normal of the boundary. In figure 4.4(b) the angular distribution for $\varphi = 0°$ and $\psi = 0°/45°$ is shown for different momenta. For an incident angle ($\psi \neq 0°$) the backward radiation is emitted asymmetrically around the direction of specular reflection. At high energies the radiation pattern is concentrated very narrowly and the asymmetry almost disappears.

The number of photons emitted by an OTR with perfectly reflecting metallic surface per electron within the wavelength range from λ_1 to λ_2 is [Gin46, Hon00]:

$$N_{OTR} = \frac{2 \cdot \alpha_{QED}}{\pi} \cdot ln\left(\frac{\lambda_2}{\lambda_1}\right) \int_0^{\theta_{max}} \frac{\beta^2 sin^3\theta}{(1-\beta^2 cos^2\theta)^2} d\theta. \tag{4.17}$$

For this equation a symmetrical distribution is assumed. θ_{max} is the angular acceptance.

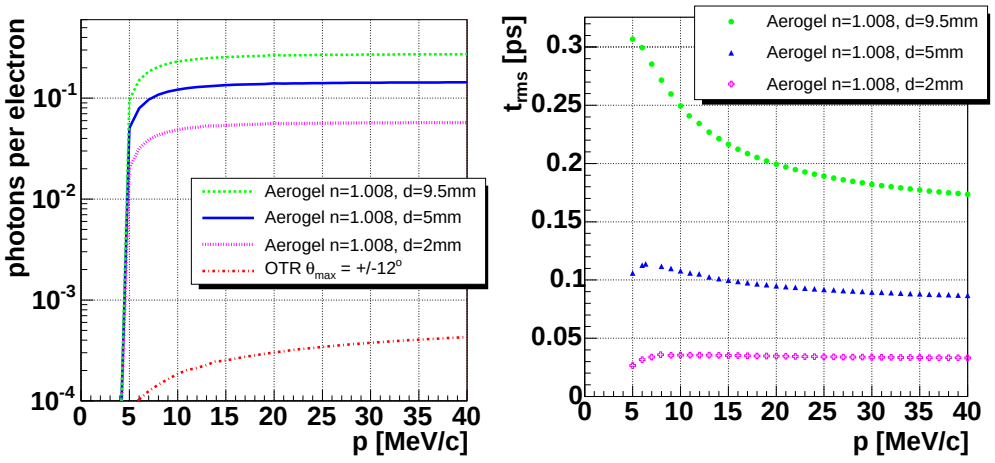

(a) (b)

Figure 4.7: *The number of photons per electron (a) and the rms value of the expected temporal resolution (b) for a aerogel with $n = 1.008$ for different thicknesses as a function of the beam momentum.*

Figure 4.7 (a) shows the number of photons produced by OTR within an acceptance angle of ±12° compared to Cherenkov radiation of silica aerogel (n = 1.008). For both radiators wavelengths from 400 nm to 750 nm were taken into account. As discussed for LOW.Scr3 the optical transmission line has a limited acceptance angle, therefore the aerogel with $n = 1.03$ and $n = 1.05$ are excluded. In the whole momentum range from 4 to 40 MeV/c the

number of photons produced by the Cherenkov radiators is about two to three orders of magnitude higher than for OTR screens. Figure 4.7(b) shows the resolution of silica aerogel $n = 1.008$ for different thicknesses as a function of the electron beam momentum. For higher energetic electrons the probability of electron multiple scattering in the aluminium foil and the radiator material is reduced and thus the temporal resolution improves towards higher energies, especially for thick radiators. As it will be pointed out in section 4.4.2 and 4.5 a rms resolution of $t_{rms} = 0.3\,\text{ps}$ does not limit the resolution of the whole system, therefore a thickness of 9.5 mm was chosen.

The OTR screen could be placed under an angle of $\psi = 45°$ to the incident electron beam, so that the backward optical transition radiation will be emitted around an angle of 90° to the electron trajectory, as shown in the right example of figure 4.6. Another possibility is to use the forward radiation of the OTR screen for the measurement of the longitudinal distribution by using a plane mirror after the OTR screen. This has the disadvantage that the beam has to pass first the OTR screen, which might cause distortions of the electron bunch, and that additional transition radiation is produced by the mirror, which influences the result. Therefore an OTR screen with an incident angle of $\psi = 45°$ is used. Due to this orientation the electrons with

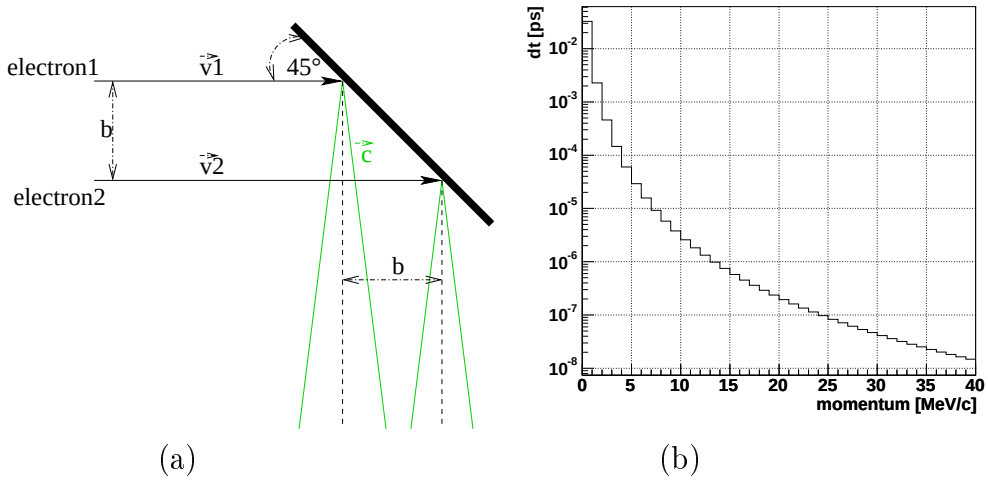

Figure 4.8: *The 45° orientation of the OTR screen produces a temporal delay between the photons produced by electrons with different horizontal positions. In graph (b) the delay was determined for b = 1 mm as a function of the beam momentum.*

different horizontal positions deliver a temporal spread (see Figure 4.8(a)) caused by the difference between the electron velocity and the speed of light

and the difference of the emission angle θ of the measured photons from the optical axis (90°): $\Delta t = \frac{b}{c}(\frac{1}{cos\theta} - \frac{1}{\beta})$, where b is the horizontal distance between two particles. In figure 4.8(b) Δt was calculated by using a distance in the horizontal position of $b = 1\,\mathrm{mm}$. The angle of maximum intensity was used in this calculation ($\theta = \theta_{peak}$). It can be seen that this effect can be neglected.

In 2007 first measurements using this screen station have been performed with (at about 16 MeV/c) and without (at about 6.5 MeV/c) usage of the booster cavity.

Since at the location of HIGH1.Scr2 the slice emittance is expected to be very small, an update of this screen station for slice emittance measurements using the streak camera [Gie99] is under consideration. This technique places special demands on the radiator and the optical transmission line, which are discussed in detail in [Spe08].

4.3 Screen stations and dipole spectrometers for measurements of momentum and longitudinal phase space distribution

4.3.1 Low energy dispersive arm (LEDA)

The low energy dispersive arm is a 60° bending magnet. In the PITZ1 setup (Fig. 2.2) the dipole entrance was located about 3.3 m downstream the gun, almost at the end of the beamline. When the booster cavity was included into the PITZ setup the spectrometer was shifted closer to the gun. The distance between cathode and dipole entrance was reduced to about 1 m. The new position has some drawbacks which demand a modification of the magnet.

Initial dipole magnet

A high resolution momentum measurement is only possible with a small beam width in the dispersion direction at a certain position corresponding to the dipole. This reference position (L_{SS}, according to equation 4.7), which was about 170 mm before the dipole entrance ($L_{SS} = -170\,\mathrm{mm}$), shifted together with the dipole spectrometer about 2.3 m upstream. Figure 4.9 shows the development of the beam size along the trajectory for different solenoid currents. One can see that in the new position a much higher main solenoid current is needed to focus the beam at the reference position. For the dipole

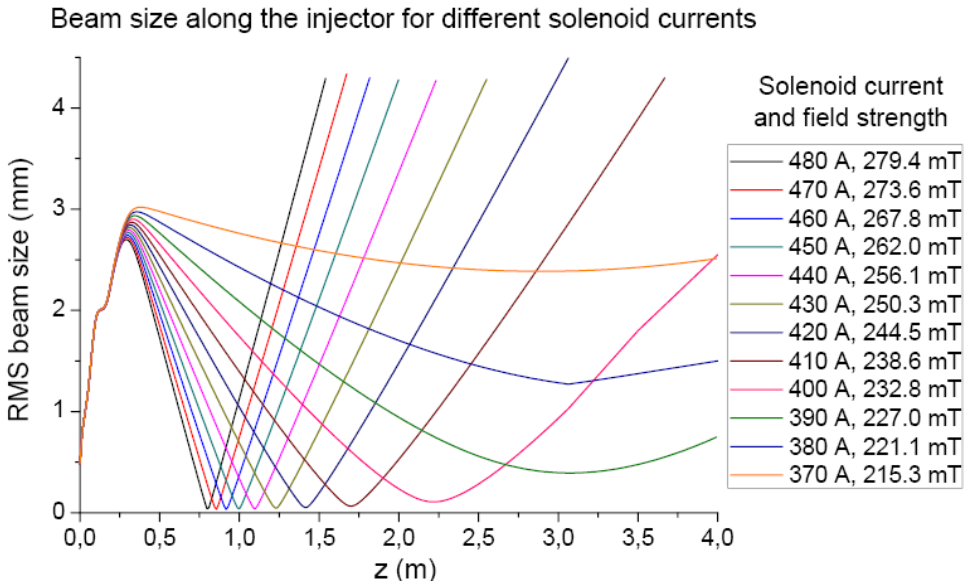

Figure 4.9: *Simulated beam size along the beamline for different solenoid currents, for 60 MV/m at the cathode, a charge of 1 nC and launch phase of maximum momentum gain.*

magnet position in the PITZ1 setup at $z_0 \approx 3.3\,\mathrm{m}$ a solenoid current of about 390 A (solenoid peak field of about 227 mT) was needed to focus a beam (of 1 nC and a momentum of about 6.8 MeV/c) at the reference position ($z_{SS} = z_0 - 0.17\,\mathrm{m} \approx 3.1\,\mathrm{m}$). For the new position at $z_0 \approx 1.0\,\mathrm{m}$ the focus of the beam with same properties at the reference position ($z_{SS} \approx 0.8\,\mathrm{m}$) requires a solenoid current of about 470 A (about 274 mT peak field strength). The maximum useable current of the main solenoid ($I_{main,max} = 500\,A$) is almost reached. For the direction perpendicular to the dispersion (non-dispersive) the change of the distribution from the dipole entrance to the screen in the dispersive arm can be described by: $y_{DA} = R_{33}y_0 + R_{34}y'_0$ (according to equation 4.1). Neglecting the influence of the fringe fields this describes a pure drift from the spectrometer entrance through the dipole magnet and the dispersive section up to the screen of about 660 mm. Due to the closeness to the photocathode only the solenoid magnet can be used to focus the beam for a high resolution momentum measurement and thus the beam size is similar in both directions.

For the PITZ1 case, were with a solenoid current of about 390 A the highest momentum resolution could be reached, the beam size at $z \approx 4\,m$ (660 mm downstream the former dipole entrance) the beam size is still comparable to the one in the focus at about 3.1 m. For the spectrometer situated

at $z = 1\,\mathrm{m}$, the application of a solenoid current of about 470 A causes a drastic growth of the beam size at $z = 1.7\,\mathrm{m}$. Thus the best momentum resolution is assumed for this case, but a large fraction of the particles miss the screen in the dispersive arm, since the beam size perpendicular to the dispersion direction is much larger than the screen.

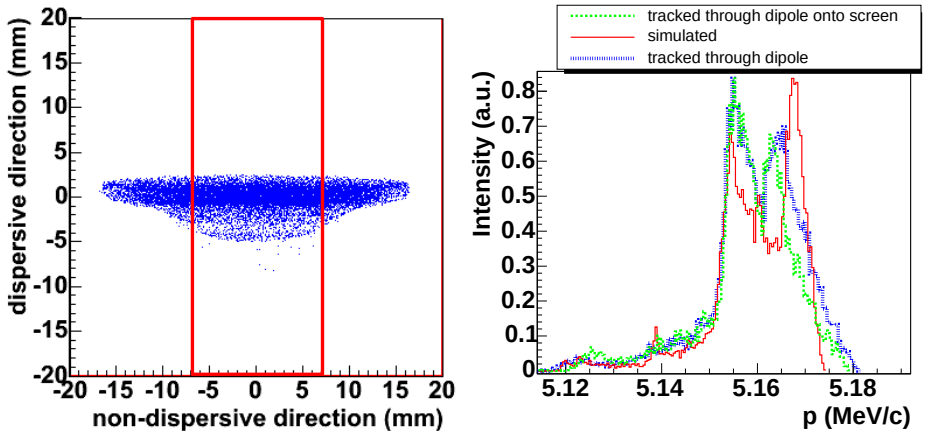

(a) (b)

Figure 4.10: *Using a focussing optimized for high momentum resolution, parts of the beam are lost beside the screen, which is drawn in red (a). Lost particles correspond mainly to the higher beam momentum and thus the measured momentum distribution (b) differs from the original one.*

Figure 4.10 (a) shows the simulated bunch distribution that was tracked through the dipole onto the screen (marked in red) in the low-energy dispersive arm for a focus on the reference position for high momentum resolution. This simulation was done for the launch phase of maximum mean momentum gain. The distribution on the screen should be compared to the initial simulated momentum distribution to judge the reproducibility. The distribution is too large in non-dispersive direction that parts of the distribution are cut by the limited screen size. This is unproblematic as long as the losses are equal for each momentum, but the solenoid focussing strength depends on the momentum. Especially at higher momentum the beam size is large. The reproduced momentum distribution, by tracing the particles though the dipole (blue) and removing all particles that do not hit the screen (green), shows a stronger reduction at higher momentum caused by the initial beam size, the initial beam divergence and the cut. This leads to an underestimation of the momentum spread. In reality most of the users choose the solenoid current too low in order to focus the whole distribution in non-dispersive direction

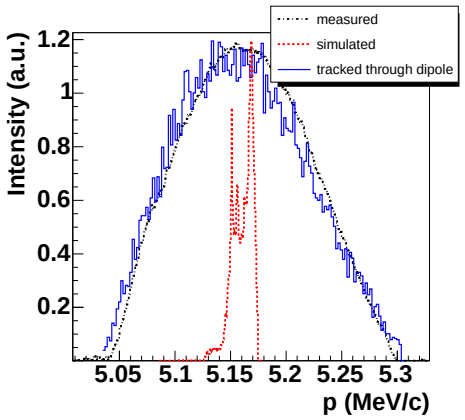

Figure 4.11: *An example for momentum measurement for an inadequate focussing. The corresponding simulated momentum distribution differs strongly from the measurement due to the influence of the initial beam size and divergence. By tracing the simulated electron beam through the dipole magnet to reproduce the measurement, the measured distribution could be reproduced rather well.*

on the screen. Figure 4.11 shows an example for such a measurement. The beam size at the reference position is too large and the momentum spread cannot be determined reliably. A slit in front of the dipole magnet would improve the situation. Also for the measurement of the longitudinal phase space distribution a slit can improve the resolution as one can conclude from figure 4.12. It shows the simulated longitudinal phase space distribution for the same conditions as in figure 4.10 and the measurable distribution in the dispersive arm. The condition 4.3 is fulfilled, but the condition 4.11 cannot be fulfilled at the same time, since a focus about 55 mm downstream the dipole entrance is required for a good temporal resolution. In figure 4.9 it is shown that for a focus at 0.8 m the beam size has strongly grown 225 mm downstream the focus point.

Another problem was the small distance between the pole shoes. It is only 20 mm and the inner size of the vacuum chamber is thus only 12 mm. For certain solenoid currents the beam size at the position of the dipole magnet exceeds the vacuum chamber. This is the case especially for those settings were the smallest transverse emittance is expected at locations significantly downstream the booster cavity. Thus it was impossible to measure the transverse emittance under these conditions. Figure 4.13 shows the total beam size as a function of the main solenoid current at the entrance of the booster and in the center of the LEDA dipole for a gradient of 60 MV/m at the cath-

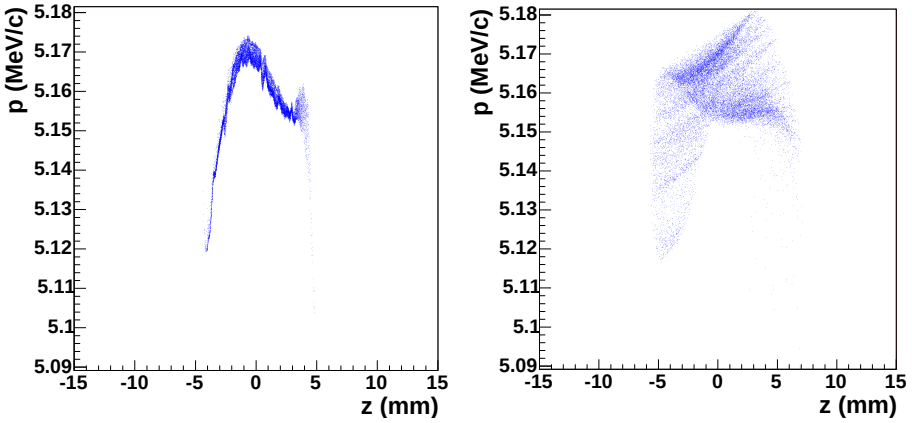

(a) (b)

Figure 4.12: *Simulated longitudinal phase space (a) and simulated measurement reach after tracing the simulation electron beam through the dipole magnet (b) for a focus at the point of best momentum resolution. The simulated measurement includes only effects of the dipole magnets, the influence of the initial beam size and divergence on the transverse distribution in the dispersive arm which represents the momentum axes and the temporal distribution.*

ode, a phase of maximum mean momentum gain and and a laser pulse with a duration of 20 ps and a transverse rms size of 0.45 mm. The 35 mm diameter of the beam tube at the entrance of the booster cavity defines the usable range of solenoid currents. In the example it is limited from a solenoid current of about 325 to 440 A (corresponding to a peak field of 190 to 250 mT). This range was further limited for smaller solenoid currents due to the dipole chamber. In the example the lower limit of the solenoid current, allowing the transmission of the beam, increases to about 377 A (220 mT). Therefore the dipole magnet was redesigned, as described in the next section.

Design considerations

As visible from figure 4.13 an increase of the inner chamber size to at least 20 mm is required to avoid limitations by the dipole. Since a misalignment in the beamline or a displacement from the design orbit has to be considered a chamber size wider than 20 mm is preferable. The typical diameter of vacuum components in that region is 35 mm. The dipole gap width has to be 8 mm wider than the inner chamber size.

The magnetic field B_0 within the flat, ferromagnetic pole shoes can be calculated by $B_0 = \frac{\mu_0 n I}{h}$, where μ_0 is the magnetic constant, n the number

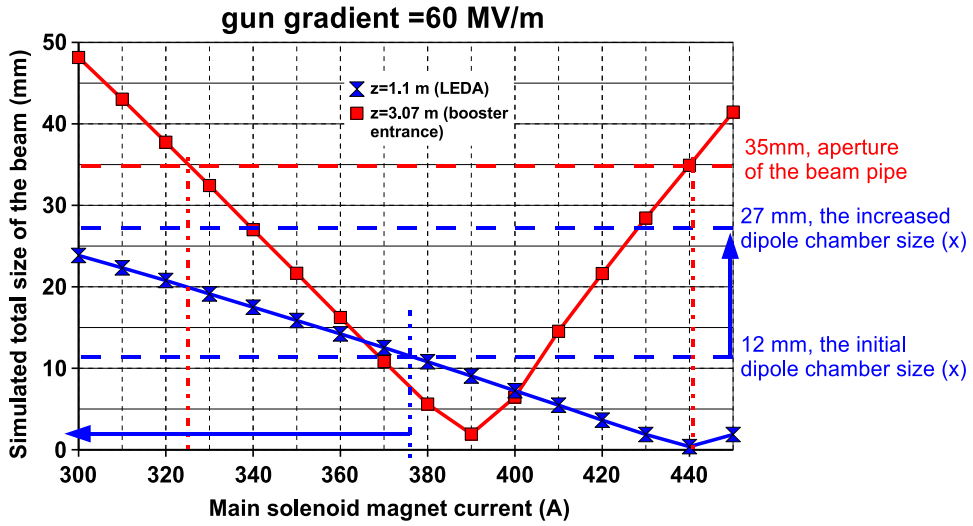

Figure 4.13: *Simulated size of the complete beam (edge to edge) at the booster entrance and inside the LEDA dipole magnet for different solenoid currents. Simulations were done for a maximum gradient of 60 MV/m at the cathode and phase of maximum mean momentum gain. Limitations due to the vacuum chamber at the booster entrance and within the LEDA dipole are shown.*

of windings of the coil, I the applied current and h the gap width. This formula can be used only as a very rough approximation, since it takes into account neither fringe fields nor the saturation of the pole shoes. But since the magnetic field $B_i(I)$ of the dipole for a gap width of $h_i = 20\,\text{mm}$ (before the the modification) is known, the magnetic field $B_f(I)$ of a magnet with a larger gap width h_f can be estimated. The larger the gap, the lower the field, and thus also saturation starts at a higher current. A possible estimation could be: $B_f(I) = B_i(\frac{h_i}{h_f}I)$, but since the material of the old pole shoes is not completely identifiable and the material of the new ones may differ, the estimation of expected field was underestimated by using: $B_f(I) = \frac{h_i}{h_f}B_i(I)$ to gain some safety margin.

Figure 4.14 shows the maximum magnetic field in the center of the dipole as a function of the current for gap width $h_i = 20\,\text{mm}$ and the estimations for larger gap widths. For a dipole magnet with an enlarged distance between the pole shoes of 35 mm (instead of 20 mm) but similar shape of the shoes, a 1.75 times higher current is needed to reach the same magnetic field.

Figure 4.15 shows the measurable momentum for the estimated fields. The left graph shows the results for an unchanged shape of the pole shoes. In this case for a chamber size of 35 mm (gap width: $h = 43\,\text{mm}$) a momentum

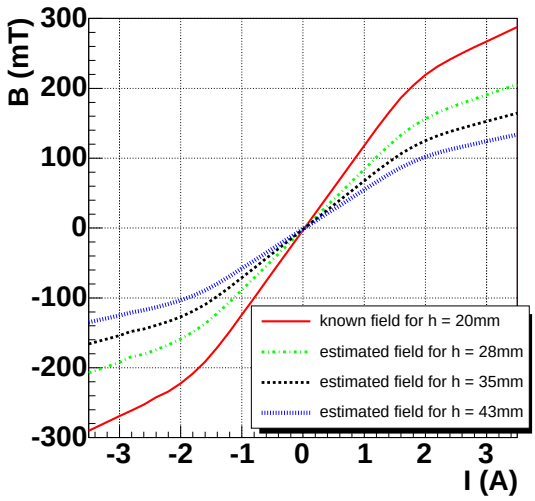

Figure 4.14: *Dependence of the magnetic field in the center of the dipole magnet for a gap width of 20 mm and the estimation of the curve for larger dipole gap widths.*

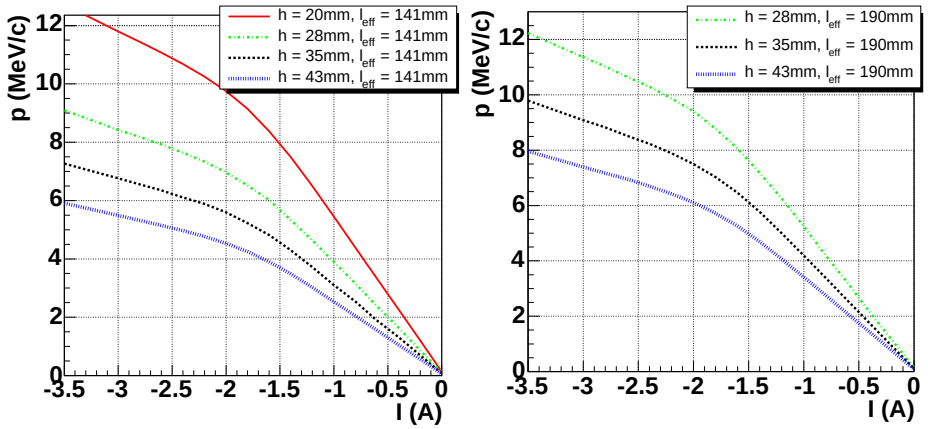

Figure 4.15: *Estimation of the measurable momentum for an increased dipole gap width. The left graph assumes an unchanged shape of the pole shoes, while in the right one an increase of the effective orbit length within the magnetic field (from 141 mm to 190 mm) was assumed, which can be reached by increasing the deflection radius of the dipole magnet.*

of 7 MeV/c is not measurable, for a maximum dipole current of $\pm 3.5\,\mathrm{A}$[2] and for a gap width of $h = 35\,\mathrm{mm}$ about 7 MeV/c is the upper limit of measurable

[2]The dipole current is limited to avoid destruction by high temperatures since the magnet is only cooled by air.

momentum. The space along the beamline is very limited but due to the change of other components in that section an elongation of the effective orbit (l_{eff}) within the dipole magnet from 141 mm to about 190 mm is possible by a redesign of the pole shoes, which was applied in the right graph of figure 4.15. In this case even with a gap width of 43 mm an electron beam momentum of 7 MeV/c is measurable. The increase of the effective orbit length of the dipole magnet (from 141 mm to about 190 mm) with a fixed deflecting angle, requires a modification of the pole shoes. It also leads to an increase of the homogenous part of the field and thus to a reduction of influence of the fringe fields. As a compromise between a maximum reachable momentum and a maximum inner chamber size a gap width of 35 mm (this means inner chamber size of 27 mm) was chosen.

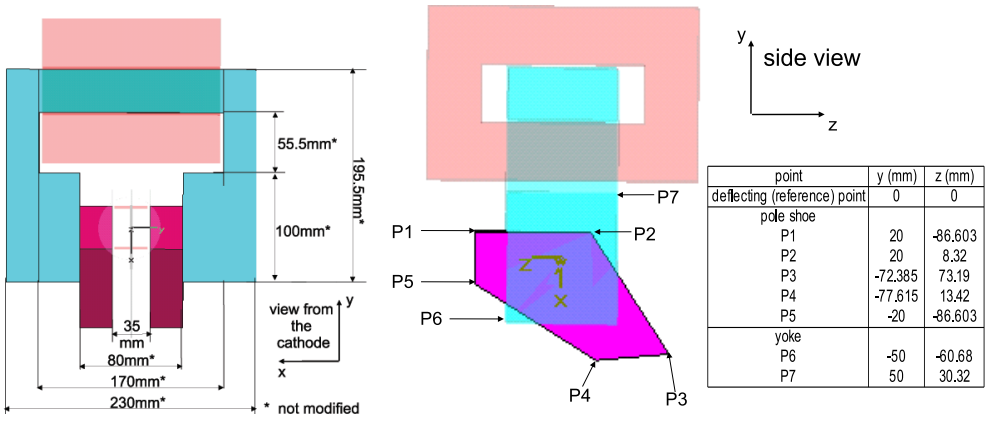

point	y (mm)	z (mm)
deflecting (reference) point	0	0
pole shoe		
P1	20	-86.603
P2	20	8.32
P3	-72.385	73.19
P4	-77.615	13.42
P5	-20	-86.603
yoke		
P6	-50	-60.68
P7	50	30.32

Figure 4.16: *Spermatical layout of the modified dipole spectrometer.*

Since the pole shoes of this magnet (with an effective length of about 190 mm) are small compared to the gap width (of 35 mm), fringe fields have a significant influence on the field distribution and have to be taken into account. This means the matrix formalism does not deliver a sufficient accuracy for the redesign. Therefore the magnetic fields for different entrance and exit pole face rotation and deflection radii were simulated[3] and typical electron bunches with different solenoid focussing (obtained from ASTRA[Flo] simulations) were traced through the field. The position of the screen station in the dispersive section was kept fix for mechanical reasons.

The optimization was done for measurements without using a slit. Figure 4.17 shows the relative error of the simulated momentum spread measurement for an entrance pole face rotation $\beta_{in} = 0°$ and a deflection radius

[3]using CST (*C*omputer *S*imulation *T*echnology), a software package for electromagnetic field simulations.

$r = 150\,\mathrm{mm}$, for an electron beam with a momentum of $6.6\,\mathrm{MeV/c}$. The source of the error is the initial transverse beam size and divergence of the bunch, which can be controlled only by the main solenoid. It was tried to

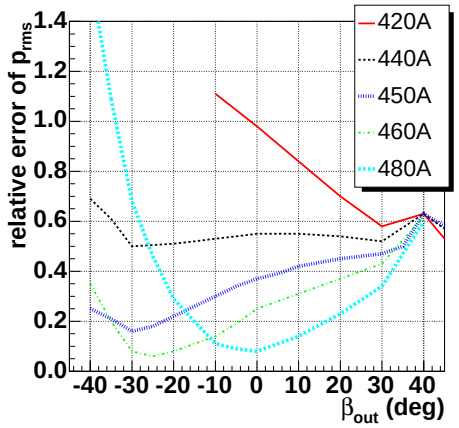

Figure 4.17: *Relative error of the simulated momentum spread measurement for an entrance pole face rotation $\beta_{in} = 0°$ and a deflection radius $r = 150\,mm$.*

move the focus point for a high resolution momentum measurement as much as possible downstream, to avoid the problem, that the beam does not fit to the screen in the non-dispersive direction (as it is was shown in figure 4.10). Figure 4.17 shows that for solenoid currents below 460 A ($B_{peak} = 268\,\mathrm{mT}$) the resolution of the measurement becomes worse. Also a change of the entrance pole face rotation does not improve the situation. A pole shoe with $\beta_{in} = 0°$, $\beta_{out} = -25°$ and $r = 150\,\mathrm{mm}$ was chosen. A $6.6\,\mathrm{MeV/c}$ electron beam is focused at about $z = 0.9\,\mathrm{m}$ for 460 A (see figure 4.9). It was not possible within the limited parameter range (fixed drift length in the dispersive section, fixed deflecting angle, limited variation of the radius) to move the reference point further downstream without losses in resolution. Figure 4.18 shows three examples of simulated momentum measurements using the chosen pole shoe design for beams with different foci (at about $z = 1.4\,\mathrm{m}$ $z = 1.0\,\mathrm{m}$ and $z = 0.9\,\mathrm{m}$). This should point out that the momentum distribution can only be reproduced with a proper focussing.

A slit of $100\,\mu\mathrm{m}$ at $z = 0.776\,\mathrm{mm}$ allows a high resolution measurement independent from the main solenoid. The simulation shown in figure 4.18 for a focus at $z = 1.4\,\mathrm{m}$ was repeated, but including this slit. The expected distribution at the screen compared to the initial distribution is shown in figure 4.19. In the graph the simulated measurement overestimates the number of particles at lower bunch energies since the focus for lower energies is

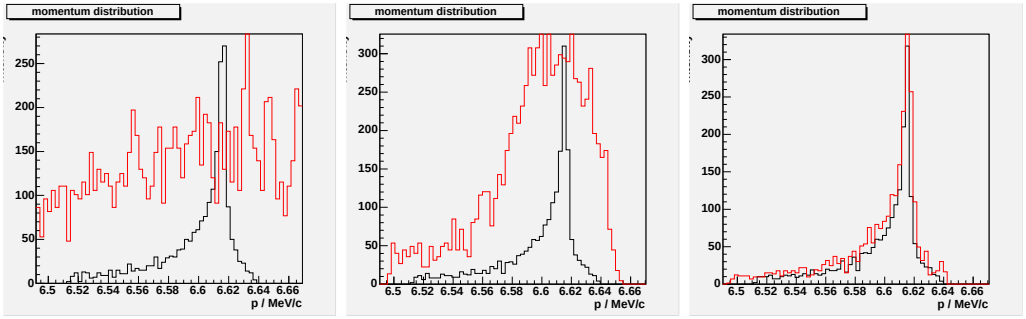

Figure 4.18: *Simulated momentum distribution (black) compared to the distribution expected at the screen after tracing though the simulated field (red) for beams with different foci at about $z = 1.4\,m$ ($I_{main} = 420\,A$ / $B_{peak} = 245\,mT$) $z = 1.0\,m$ ($I_{main} = 450\,A$ / $B_{peak} = 262\,mT$) and $z = 0.9\,m$ ($I_{main} = 460\,A$ / $B_{peak} = 268\,mT$), from left to right.*

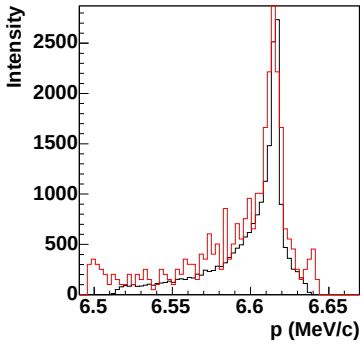

Figure 4.19: *Simulated momentum distribution (black) compared to the distribution expected at the screen after applying a 0.1 mm slit and tracing though the simulated field (red) for a beam focused at about $z = 1.4\,m$ ($I_{main} = 420\,A$ / $B_{peak} = 245\,mT$)*

closer to the slit position and thus the fraction of lower energetic electrons passing the slit is a little higher. A slit width of 100 μm (and 200 μm as a replacement) where chosen.

As a conclusion, it can be said that the gap width of the low-energy dipole magnet, could be modified with a very low technical effort. It was tried to optimize the reachable momentum resolution with the limited number of variable parameters. For an appropriate alignment and focussing of the beam (without using the slit), at optimum phase a resolution of the momentum spread of about 5% is realistic.

Results from field measurement

Field measurements of the modified dipole magnet have been performed. The left graph of figure 4.20 shows the measured magnetic field distribution in the dispersive plane. In the right graph the magnetic field strength along the

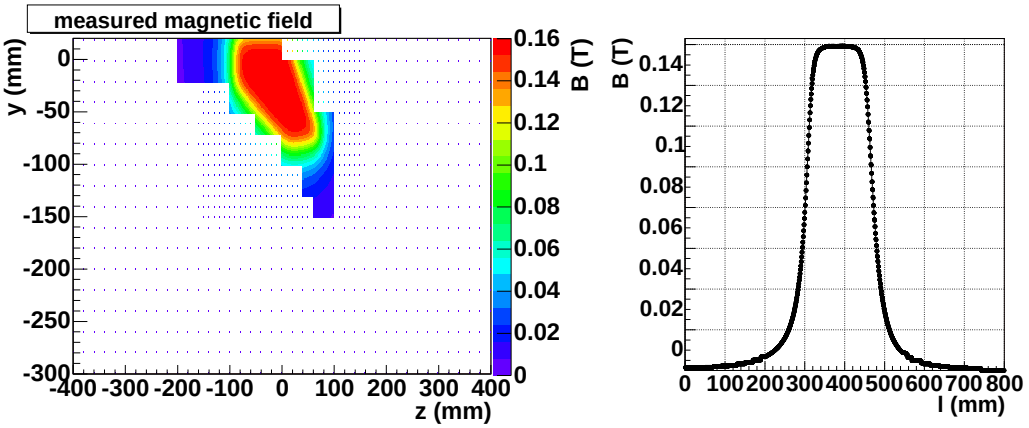

Figure 4.20: *Measured magnetic field distribution in the dispersive plane (left) for a dipole current of -3.5 A and the magnetic field strength along the design trajectory of a particle traveling through that field.*

design orbit is shown. The effective magnetic length along the design orbit can be determined from the curve with

$$l_{eff} = \frac{\int B(l)dl}{B_{peak}} = (193.7 \pm 0.5)\, mm. \tag{4.18}$$

Although the effective area of the pole shoes was enlarged as much as possible, the influence of fringe field is still rather strong. Figure 4.21(a) shows the relative discrepancy in the field strength of a plane with 10 mm offset from the gap center and the field in the symmetry plane (which was shown in figure 4.20). Figure 4.21(b) shows the change of the magnetic field along the gap at different positions. At the edges of the pole shoes the difference between the center of the gap and an offset position of 8 mm is about 5%. In the momentum measurement this results in an error in the momentum measurement of 22,5 keV/c, but the screen is not large enough to see a particle with such an offset. Since the influence of fringe fields scales quadratically with the distance to the center (according to equation 4.14) the effect is reduced to 8.8 keV/c for an offset of 5 mm.

Figure 4.22 (left) shows the magnetic field in the center of the dipole as a function of the dipole current. In order to determine the momentum

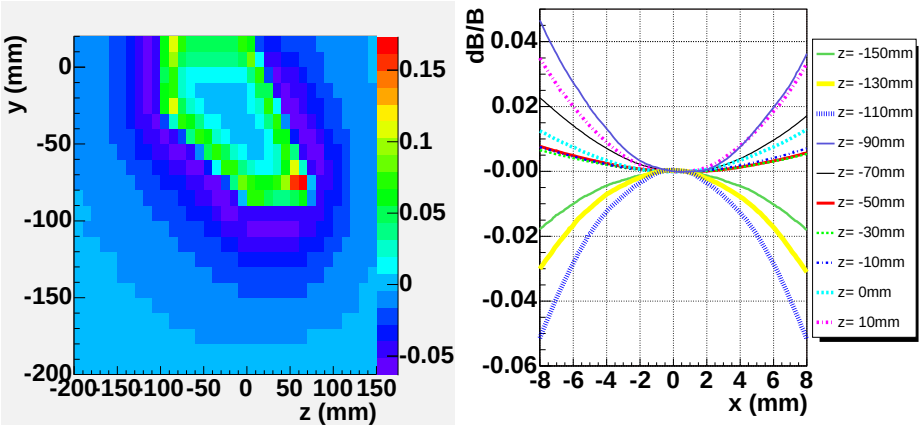

(a) (b)

Figure 4.21: *The relative field strength discrepancy between a non-central (10 mm) and a central gap position (a) and the relative field strength discrepancy from the central value along the gap (x-direction) for $y = 0$ in intervals of $\Delta z = 20\,mm$ (b).*

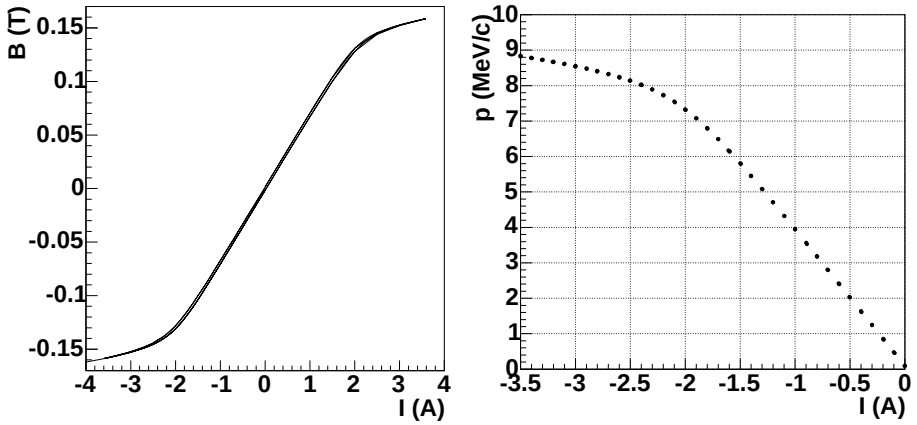

Figure 4.22: *Measured magnetic field strength in the center of the dipole magnet as a function of the dipole current (left). The whole hysteresis was measured, but the difference of rising and falling currents is hardly distinguishable. The right graph shows the resulting momentum dependence on the dipole current.*

at the center of the screen using: $p_c(I) = |eB(I)|\frac{l_{eff}}{\alpha}$ the magnetic field at this point has to be identical with the point where B_{peak} from equation 4.18 was determined, or has to be scaled. The resulting momentum dependence on the dipole current is shown in the right graph of figure 4.22. It roughly

agrees with the estimations (shown in figure 4.15) and to our requirements. The maximum measurable momentum is about 9 MeV/c, which is above the expected momentum for 60 MV/m of about 7 MeV/c, thus it fulfills the requirements. In [Lip04] it was proposed to fit the dependency of the magnetic field on the dipole current with the following exponential function of 3 variables (a, b, c):

$$B(I) = \frac{a \cdot (I - b)}{1 + e^{-c/(I-b)^2}}. \tag{4.19}$$

In the left graph of figure 4.23 the error in the determination of the central

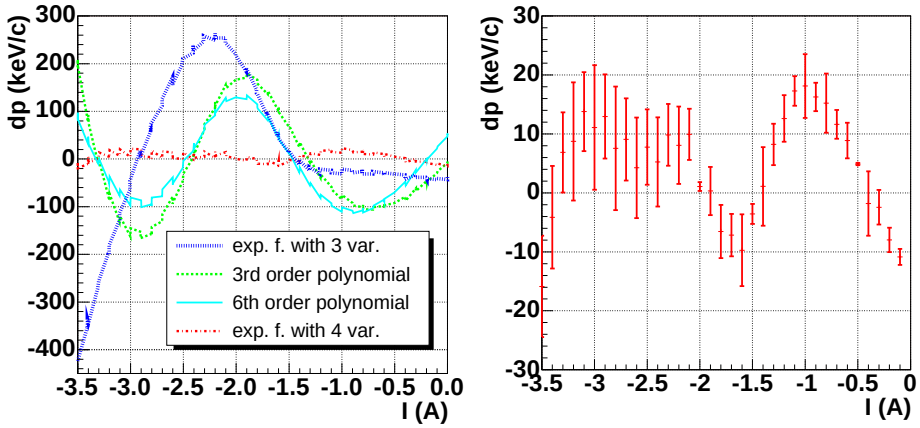

Figure 4.23: *Error in the determination of the mean momentum due to the discrepancy between the measured and fitted hysteresis curve. The left graph shows different fitting functions and the right one shows the best curve in more detail.*

momentum due to the discrepancy between the measured and fitted curve is shown. Since the discrepancy is quite large for the proposed function different fitting curves have been tested. A 3^{rd} order polynomial decreases the maximum errors slightly. Changing to higher order polynomials improves the result insignificantly. By applying a slight modification to equation 4.19 by introducing a fourth variable (d):

$$B(I) = \frac{a \cdot (I - b)}{d + e^{-c/(I-b)^2}}. \tag{4.20}$$

the error in the determination of the mean momentum can be reduced significantly. In the right graph of figure 4.23 the discrepancy for the fit with the exponential function of 4 variables is shown in more detail. In this case the error of the momentum determination using the exponential function of 4 variables is almost comparable to the precision of the field measurement and

is negligible compared to the total error taking into account orbit alignment errors.

Since the initial dipole magnet was constructed for a usage up to 2.4 A the temperature of the coil was observed during the field measurements. An increase of the coil temperature with time was observed. Applying a current of $|\ I\ | = 3.5$ A for 8 hours to the magnet the coil temperature increased from 12 to about 45° C. It causes also a change in the field that causes an error in the momentum measurement of about 30 keV/c. In the measurement the magnet will typically be used at a current of 2 A, therefore a smaller effect is expected. During the first usage of the magnet at the PITZ facility a temperature increase from typically 22 to 35° C was observed, thus a maximum difference of about 12 keV/c is expected, which is smaller than the energy jitter of the beam.

Results from beam momentum measurement

A first measurement using the modified spectrometer dipole magnet was done. The slit of 100 μm width in front of the dipole was used during the measurement in order to improve the resolution. To reach a sufficient signal to noise ratio 50 pulses have been taken. Figure 4.24 shows measurements of the momentum distribution compared to ASTRA simulations of the beam. The measurement was performed for a Gaussian longitudinal laser distribu-

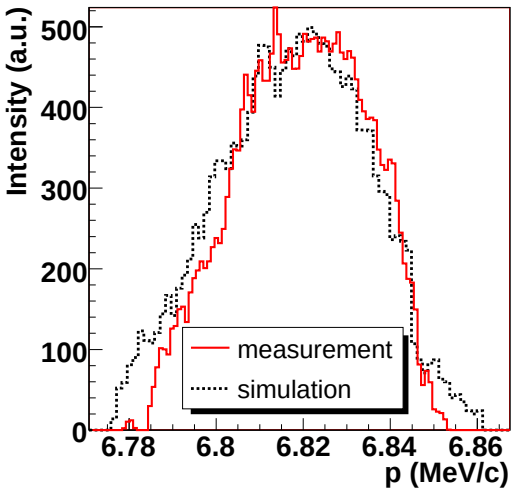

Figure 4.24: *Measured momentum distribution of the gun using the redesigned dipole spectrometer compared to ASTRA simulations of the beam.*

tion with a FWHM of 2 ps, a gradient of 60 MV/m at the cathode, the phase

of maximum mean momentum gain, an rms transverse laser beam size of 0.58 mm and a peak solenoid field of about 270 mT. The simulated momentum distribution at the position of the slit could be reproduced with good agreement. The high and the low energy part of the bunch are underestimated in the measurement, since the focussing on the slit and thus the number of particles passing the slit are energy dependent.

4.3.2 High energy dispersive arm 1

The first High- Energy- Dispersive- Arm (HEDA1) is located about 4 m downstream the center of the booster cavity and it will be used for measurements of:

- the beam momentum distribution,
- the slice emittance [4] and
- the longitudinal phase space distribution using the streak camera.

For the determination of the momentum and the longitudinal phase space distribution of the bunch a precise measurement for gun and booster phases close to the phase of minimum momentum spread and maximum momentum gain ($\phi_{p(max)}$) is of high importance, which desires a large dispersion. On the other hand for slice emittance measurement it is essential to measure at booster phases which deliver a linear distribution of the bunch in the longitudinal phase space (a bunch with a linear momentum chirp). This is the case for far off-crest booster phases, which is typically a phase of $\phi_{p(max)} + 70°$. It has to be taken into account, that at off-crest phases the momentum spread is very large, and for an adequate measurement a limited dispersion is required. These requirements are contradictory, and a compromise has to be found [Kho06].

In [Lip05-2] a 180° bending magnet was proposed as a spectrometer. The usage of a dipole magnet with a deflection angle of $\alpha = 180°$, without pole face rotation ($\beta_{in} = \beta_{out} = 0°$) and the assumption $L_{before} = 0$ simplifies

[4] The technique for the determination of the slice emittance in the dispersive arm is based on the following idea: For a linear longitudinal phase space distribution (also called a bunch with a linear chirp) a slice in momentum range corresponds to a slice in the temporal distribution. A slit in the dispersive arm is used to select a momentum range and thus a longitudinal slice of the bunch. The transverse emittance of this slice is measured by scanning the beam size in the plane orthogonal to the dispersive one using quadrupole focusing.

equation 4.4 and 4.10 to:

$$R_{11} = -1, R_{12} = -L_{DA}, R_{16} = 2r,$$
$$R_{51} = 0, R_{52} = 2r, R_{56} = -r \cdot \pi + \frac{r \cdot \pi + L_{DA}}{\gamma^2}. \tag{4.21}$$

The 180° bending magnet has the special property, that the dispersion function ($R_{16} = 2r$) is independent of the drift length in the dispersive section. Applying the matrix element of the 180° bending magnet (equation 4.21) to condition 4.7 the drift length in the dispersive arm should be equal to the drift from the dipole entrance to the reference screen in the straight section ($L_{SS} = L_{DA}$). The layout of the dispersive section of HEDA1 is schematically shown in figure 4.25. The deflection radius was chosen to be $r = 300$ mm

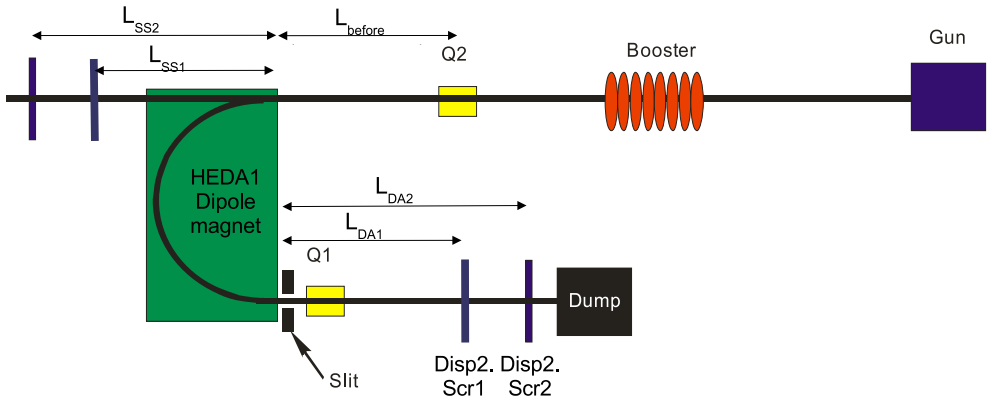

Figure 4.25: *Schematic of the layout of the first high energy dispersive arm in the PITZ beamline.*

as a compromise between space requirements, momentum resolution and the ability of the spectrometer to operate within a large range of gun and booster phase. In figure 4.26 the total beam size at the first screen in the dispersive section of the chosen dipole magnet is shown. The inner diameter of the quadrupole magnet Q1 is about 80 mm, thus a screen size of about 80 mm in dispersive direction was chosen. Within a booster phase range of about -35° to 35° the whole beam fits into the beam pipe and can be measured in a single shot. This range is marked with red lines in figure 4.26.

The quadrupole doublet upstream of the spectrometer (Q2) can be used to focus the beam on the reference screen (located in a distance L_{SS} downstream the dipole entrance).

Figure 4.27 (a) shows an ASTRA simulation of the longitudinal phase space distribution of the bunch (for gun and booster phase of maximum mean

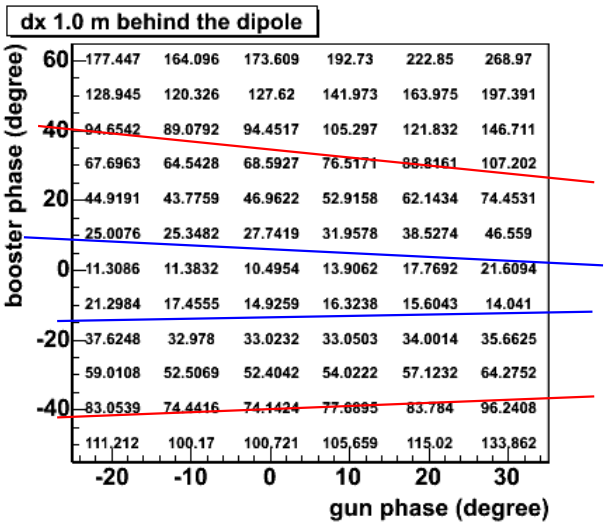

Figure 4.26: *Total beam size (mm) in the dispersive plane on the first screen as a function of gun and booster phase. The red lines mark the phase range within which the whole beam fits into the beam pipe and thus on the screen. The imaging of the whole distribution onto the camera requires an optical demagnification of 14. Additionally to the demagnification of 14 a demagnification of 4 has been realized for detailed measurements of the distributions with small momentum spread . The blue lines marks the phase range in which the whole distribution is visible applying the demagnification of 4.*

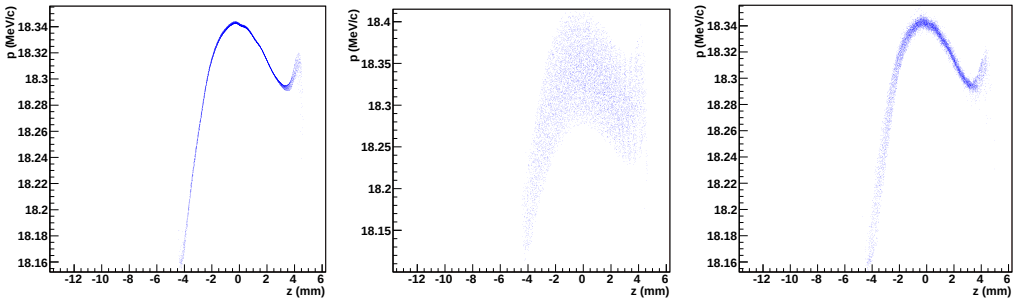

(a) (b) (c)

Figure 4.27: *Simulated (a) longitudinal phase space distribution at the entrance of HEDA1 compared to the expected measurement at Disp2.Scr1 by applying the matrix formalism, without (b) and with (c) focusing on the reference screen. The expected measurement takes only the influence of the dipole magnet into account.*

momentum gain) at the entrance of the HEDA1 dipole magnet. To analyse the dependency of the resolution on the focussing the particles were tracked through the dipole using the matrix formalism. Figure 4.27(b) and (c) show the expected measurable longitudinal phase space distribution applying the matrix formalism without (b) and with (c) focussing on the reference screen. A correction of the influence of the matrix element R_{56} (as discussed in section 4.1.3 a shearing of the distribution in the longitudinal phase space can be used to correct the effect) was already applied.

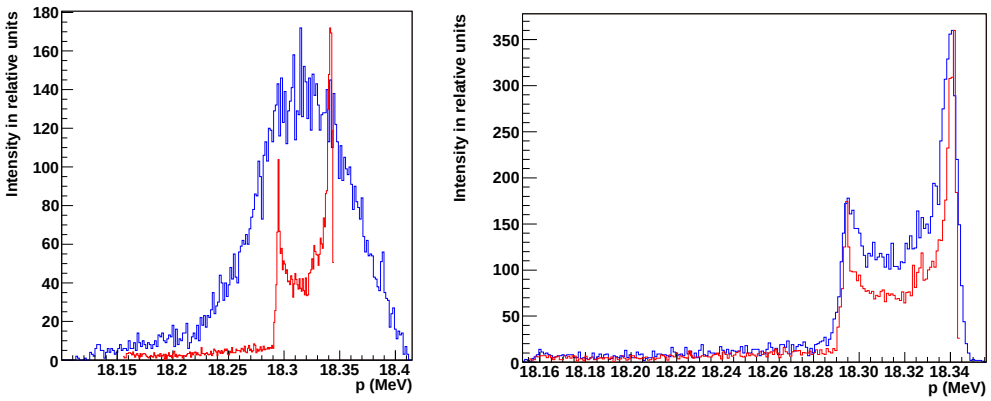

(a) (b)

Figure 4.28: *Expected reproduced momentum distribution at the screen at HEDA1 (blue) compared to the initial momentum distribution (red), without (left) and with (right) focusing on the reference screen.*

Figure 4.28 shows the resulting expected measurable momentum distribution for both cases (without (a) and with (b) quadrupole focussing) compared to the initial simulated momentum distribution.

The first row (a) of table 4.2 summarizes the absolute values of the mean momentum, momentum spread and longitudinal emittance of the simulated longitudinal phase space distribution presented in figure 4.27 (a). For the expected measurable distributions, for both cases without (b) and with (c) focussing on the reference screen (shown in figure 4.27 (b) and (c)), the relative deviations of the longitudinal properties from the initial values are listed.

The usage of a quadrupole magnet is mandatory to reach a highly resolved momentum distribution. If the beam is not focused on the reference screen, but the transverse distribution at this position is known, a deconvolution can be applied after the measurement. The distribution on the reference screen has been used as the point spread function to reconstruct the real momentum

	p_{mean} (MeV/c)	p_{rms} (keV/c)	ϵ_{long} (π keV/c mm)
(a) absolute value	18.3105	36.5348	75.7240
(b) relative deviation	−0.0009%	33.75%	38.29%
(c) relative deviation	−0.0005%	0.16%	0.50%

Table 4.2: *The row (a) lists the absolute values of the mean momentum, the momentum spread and the longitudinal emittance of the simulated longitudinal phase space distribution shown in figure 4.27 (a). The rows marked with (b) and (c) present the relative deviation from the simulated values for the reproduced distribution after tracing the bunch through the dipole without (b) and with (c) applying the focus on the reference screen.*

distribution, but a deconvolution is sensitive to noise (for example due to the camera) and should be avoided, if possible.

Due to limited space and the need of a long drift between the quadrupole in the dispersive arm (Q1) and the screen station for slice emittance measurements it was decided to include two screen stations in HEDA1. Table 4.3 gives an overview of their properties. Since the measurable momentum dis-

screen station	L_{DA} (mm)	radiator/ screen	camera	measurement goal	momentum range (MeV/c)
DISP2. Scr1	1375	aerogel	streak	long. phase space	4-40
		YAG	TV	momentum	4-30
DISP2. Scr2	1922	OTR	TV	momentum	30-40
			streak*	long. phase space	30-40
		YAG	TV	slice emittance	4-20

Table 4.3: *Summary of the screen stations and their task in the first high-energetic section. (* not realized in PITZ1.7)*

tribution can become up to 80 mm, the partial cone optics option of the silica aerogel is used. For the usage of the partial cone scheme the emission angle does not play a role, therefore $n = 1.05$ was chosen, because at lower energies it produces more photons for a similar resolution (see figure 4.5) and the energy threshold is lower. Two values of thicknesses of silica aerogel have been prepared: 2 mm and 5 mm. For a thickness of 2 mm an rms temporal resolution of $\delta t_{rms} = 0.21$ to 0.25 ps (depending on the energy) could be

reached. For a thickness of 5 mm, a temporal resolution of about 0.53 to 0.63 ps was estimated. Figure 4.29 shows the expected change of the longitudinal phase space distribution (a) due to the dipole (b) and the aerogel of 2 mm (c) or 5 mm (d) thickness. For figure 4.29 (b), (c) and (d) the momentum compaction factor (R_{56}) was corrected (as described in 4.1.3) to reach a better comparability. Already after tracing the bunch through the dipole the longitudinal emittance is increased, due to the residual influence of the beam size. The resolution degrades further with increasing thickness of the radiator, but the shape of the phase space is still comparable. Since the resolution is limited by the optical transmission line and streak camera to about Δt_{FWHM} =4 ps, for the first usage at PITZ 1.7 a thickness of 5 mm was chosen, in order to increase the usable number of photons. After an improvement of the optical transmission (see: section 4.4.3) the aerogel can be exchanged by the thinner one (2 mm). The OTR screen is planned to be used for momentum measurements at higher energies. The usage of the full cone optics of the OTR screen in the second screen station would be interesting especially for higher energies, since the emission angle of the optical transition radiation becomes very small at higher energies (see figure 4.4) and thus the complete angular distribution could be transported to the streak camera. The numbers of photons of the partial cone of silica aerogel and the full cone of an OTR screen are comparable for momenta larger than 30 MeV/c, but the resolution would be higher. Since at the moment the screen is not limiting the resolution and using the TESLA booster an electron beam momentum of 30 MeV/c is not reachable, the usage of the OTR screen for measurement of the longitudinal phase space distribution is currently not realized.

For the momentum measurement two optical systems are foreseen to image the distribution at the screen onto the TV-camera. The first system should demagnify the distribution by about a factor of 14. This factor images the whole screen of about 80 mm onto the CCD-camera chip. For this demagnification one pixel of the camera corresponds to a momentum width of 5.81 keV/c at 30 MeV/c. This is limiting the resolution of small details of the momentum distribution as figure 4.30 shows. The momentum distribution (for gun and booster phase of maximum mean momentum gain) shows a double spike in the momentum distribution, caused by space charge forces. These small details in the distribution cannot be resolved, when the whole screen is observed, due to the pixel limitation. Therefore, the second optical system provides a demagnification of about 4. In figure 4.26 the measurable range for a demagnification of 14 is shown in red and for 4 in blue. The

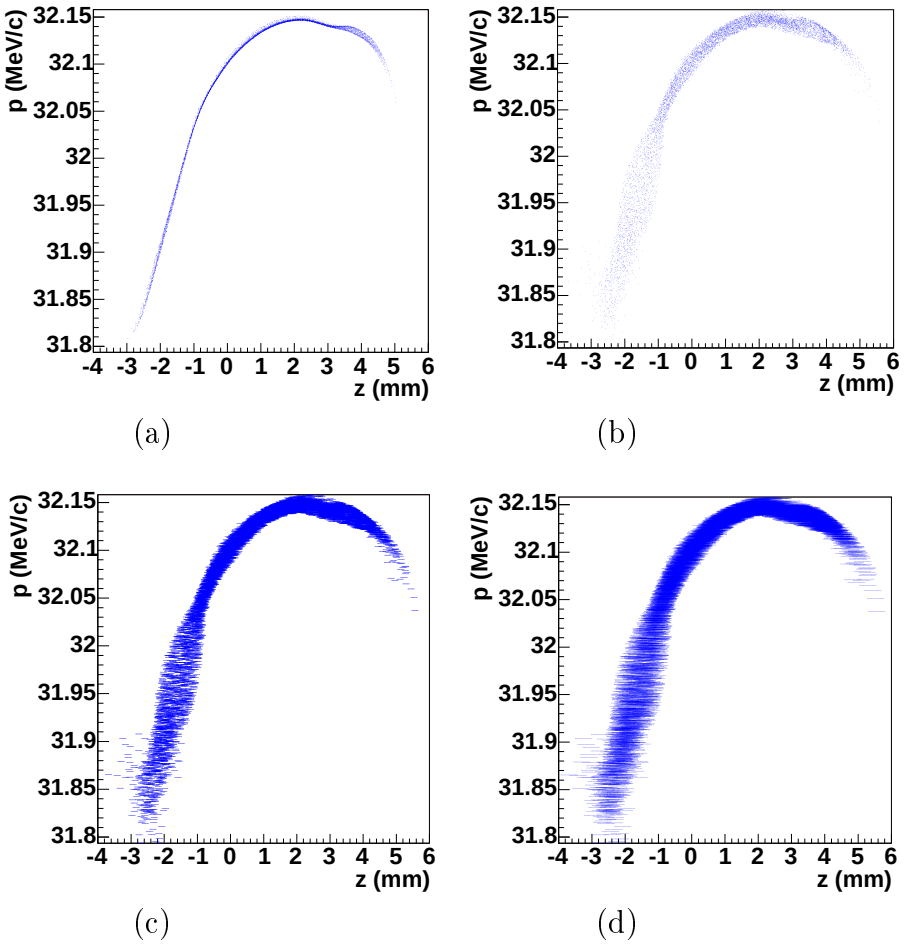

Figure 4.29: *The simulated longitudinal phase space (a) was traced through the HEDA1 dipole magnet. In figure (b) the longitudinal phase space is shown after tracing the beam through the dipole magnet and recalculating the transverse axis into momentum values. The electron bunch was transformed into a light pulse by an silica aerogel $n = 1.05$ with a thickness of 2 mm (c) or 5 mm (d).*

spatial resolution was simulated using ZEMAX [5] for both systems. For the demagnification of about 14 a spatial resolution of the object of 12 line pairs per mm (LP/mm) could be reached. This means structures larger than 42 μm can be resolved. This corresponds to about 3 μm in the image plane, which is smaller than the pixel size of the CCD camera (the cameras typically used at

[5] ZEMAX [ZEM09] is a software for the design and calculations of optical systems and their properties.

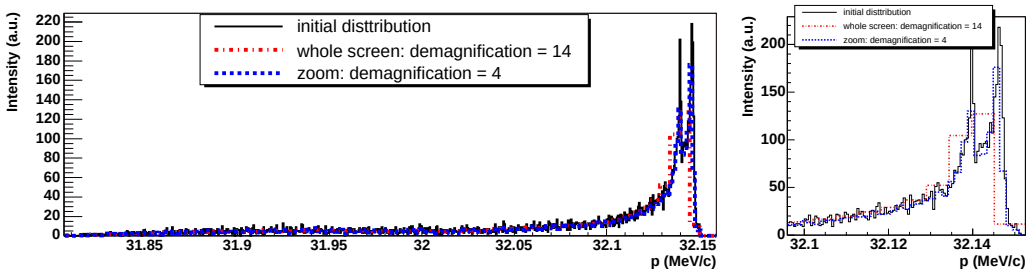

Figure 4.30: *Simulated momentum measurement in HEDA1 with two optical systems with different magnifications. (a) shows the whole momentum distribution and (b) shows the region around the maximum of the momentum distribution.*

PITZ have a pixel size from 4.7 to 8.3 μm). For the demagnification of about 4 a spatial resolution of about 30 LP/mm was determined in the simulation, this corresponds to about 4 μm in the image plane. This means the optical system is not expected to limit the resolution.

The field of the magnet was measured by the manufacturer. The left graph (a) in figure 4.31 shows the magnetic field map $\pm$40 mm around the design trajectory[6] and the right one (b) the magnetic field along the path of an electron traced trough the central trajectory. Compared to the magnetic field of the LEDA dipole magnet (see figure 4.20) the magnetic field is very homogenous along the trajectory, due to the larger deflecting radius and the larger deflecting angle. The measured effective length of the magnet is 941.7 mm. This agrees well with the geometrically determined effective length = 942.5 mm. The electron bunch was traced through the measured magnetic field. Figure 4.32 shows a simulated momentum distribution upstream the dipole magnet compared to the distribution obtained on the screen in the dispersive section after tracing the bunch with its remaining beam size at the reference screen at through the dipole. They show a good agreement.

4.3.3 High energy dispersive arm 2

Demands

The second high energetic dispersive arm will be used to measure several beam parameters:

- the momentum distribution

[6]Measured by Sigma Phi [Sp06].

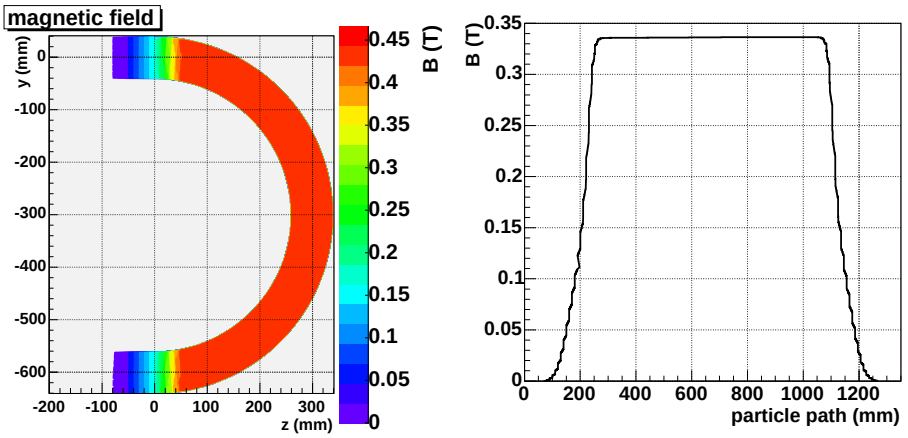

(a) (b)

Figure 4.31: *Measured magnetic field distribution of the HEDA1 dipole magnet for maximum dipole current (a) and the magnetic field along the trajectory of a 30 MeV/c particle traced trough the field of the dipole magnet along the design orbit (b).*

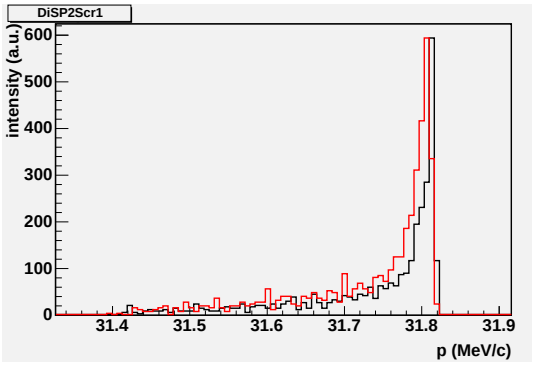

Figure 4.32: *Simulated momentum distribution at the HEDA1 entrance (black) traced through the magnetic field of the HEDA1 dipole magnet (red).*

- slice emittance (at an off-crest booster phase) and
- the longitudinal phase space distribution using:
  - a Cherenkov radiator and a streak camera or
  - the RF deflector.

As already discussed for HEDA1, it is a demanding task to fulfil the contradicting conditions for high-resolution measurements of slice emittance and

momentum distribution at the same time. The most important task for HEDA2 is the highly resolved longitudinal phase space measurement using the RF deflector, which includes a highly resolved momentum measurement. The measurement of the longitudinal phase space distribution using streak camera is expected to reach a much lower resolution than using the RF deflector (and thus has a lower priority). Also the slice emittance measurement is subordinated at HEDA2 since the position of minimum emittance is much closer to HEDA1 than HEDA2 and thus the expected slice emittances at HEDA1 are smaller than at HEDA2. A major design request is to allow the measurement of selected bunches from long bunch trains with 7200 pulses and a repetition rate of 10 Hz for a long time period. Single pulses within the long train should be studied to determine effects of pulse heating[7] and beam loading[8]. This requires a huge beam dump (2 m × 2 m

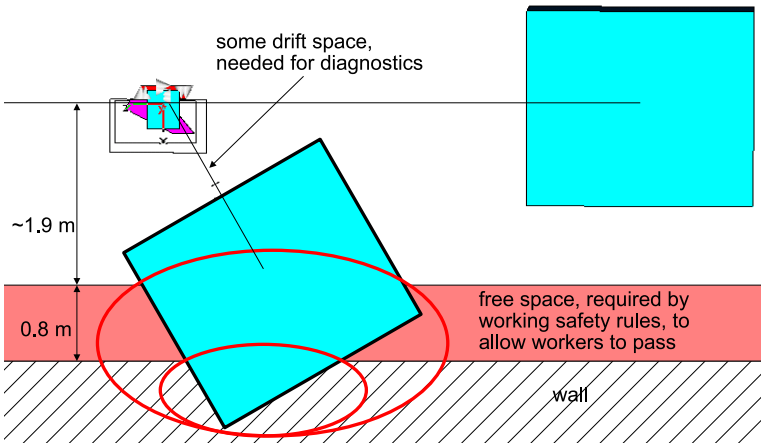

Figure 4.33: *The figure shows the final part of the main beamline in the PITZ-2 setup with the HEDA2 dipole and the main beam dump at the end. To be able to run HEDA2 with the full number of pulses a dump of the same size as the main dump would be needed in the dispersive section, but there is not sufficient space between the beam line and tunnel wall for a separated dump.*

× 2 m) downstream the dispersive section, but there is not enough place for a separate dump (see figure 4.33), so the beam has to be transported to the dump of the main beamline. It has to be ensured that the beam hitting the dump is neither too big nor too small, compared to the beam dump. The

[7] A change of the resonance conditions caused by detuning of the cavity during the long RF pulse results in a change of the phase.

[8] The electron beam interacts with the impedance of the RF structure. This induces a beam loading voltage that affects the following bunches.

stress limit of the dump material, aluminium, is about 50 K. The temperature rise of aluminium without cooling is about $244\,K\,\frac{mm^2}{nC}\frac{Q}{\sigma_x\sigma_y}$ [Rie05], for 7200 bunches with $\frac{Q}{\sigma_x\sigma_y}$ the bunch charge density. To stay below the stress limit the beam size at the dump has to be controlled using the dispersion of the spectrometer dipole combined with energy spread of the electron bunch and a quadrupole magnet. For long pulse trains special diagnostic devices or materials are needed because the standard screen used at PITZ would be destroyed for small beam sizes. Also the optical transition radiators used at PITZ are covered with aluminum and thus similar requirements as for the dump are valid. When long bunch trains are used it has to be ensured that the beam does not hit the beam pipe. Therefore, the beam size has to fit into the beam tube for booster phases within a range of at least $\pm 10°$.

Needed diagnostics elements

In order to fulfil the measurement tasks, the following devices have to be included in or before the dispersive section:

- for short bunch trains: at least one screen station containing YAG and OTR-screens to measure the momentum distribution, longitudinal phase space distribution (using RF deflector) and slice emittance as well as a Cherenkov radiator for the measurements of the longitudinal phase space distribution using the streak camera,

- a slit and a quadrupole at least 1 m upstream the screen for slice emittance measurements. The drift length is required to reach a proper focus and thus resolution of the slice emittance measurement,

- a large aperture BPM for the measurement of the mean position of the bunches in the dispersive arm and thus the mean momentum of different bunches in a long pulse train.

- a kicker before the spectrometer dipole magnet in order to kick out a single pulse out of a long pulse train to be analysed on a corresponding off-axis screen,

- an ICT in front of the dump to ensure that all particles reach the dump for the usage of long bunch trains.

Since the slit for slice emittance measurements should be placed at the position of highest momentum resolution, two screen stations are useful: one for

measurements of momentum and longitudinal phase space distribution, containing also the slit for slice emittance measurements, and a screen station for the slice emittance measurements.

Design options

The deflecting radius of the dipole magnet should be much bigger than the gap of the pole shoes which is expected to be about 45 mm, in order to reduce the influence of fringe fields. Different design options are shown in figure 4.34.

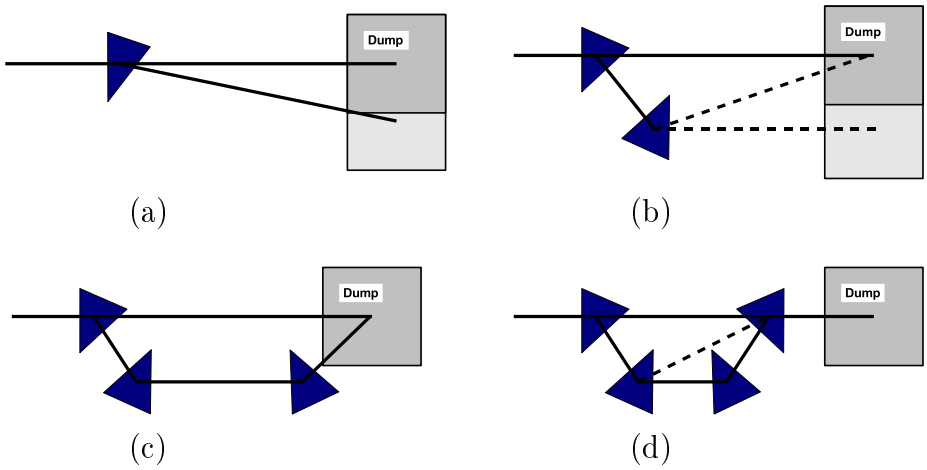

Figure 4.34: *Different design options of HEDA2 dispersive section in order to transport the beam from the spectrometer to the main beam dump.*

(a) A simple possibility to transport the beam to the main beam dump is to expand the dump by about a meter in horizontal direction and to use a dipole magnet with a small deflection angle. The main advantage is the large drift length in the dispersive section in order to place all foreseen diagnostic devices. Since the angle of such a layout is expected to be smaller than 15° due to the spatial circumstances in the facility, the components in the dispersive and the straight beamline would interfere, and additionally the momentum resolution is expected to be low. Consequently a simple setup containing only one magnet has been excluded.

(b) The use of a larger dispersion angle (30° - 90°) requires a second dipole magnet to deflect the beam to the dump in the main beamline. The second dipole needs to have at least the same deflection angle as the first

one, in order to deflect the beam to the main dump. The drift length after the first dipole magnet is limited, since all diagnostics components of the dispersive section have to be within 1.9 m in x-direction from the main beamline (see figure 4.33). With increasing deflecting angle, the drift after the first dipole becomes smaller. The second magnet should deliver a proper dispersion at the dump. The beam should be large enough to avoid a high temperature rise in order not to destroy the dump but it must be smaller than the allowed beam area at the dump. A quadrupole magnet can be used to reach the proper beam size. In the case that the drift length after the first dipole is too small, the slice emittance measurement can be performed downstream the second dipole. This has to be taken into account for the design of the second magnet.

(c) In order reduce the requirements to the second magnet a third dipole magnet could be included into the setup.

(d) There is also the idea to transport the beam back to the main beamline like in a bunch compressor.

Figure 4.35 shows a possible distribution of the diagnostic elements in the dispersive section, assuming two dipole magnets (case (b)). Also for the cases (c) and (d) the distribution of the components could be similar.

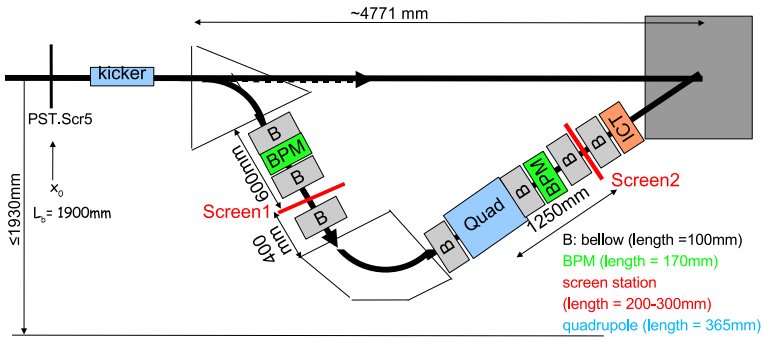

Figure 4.35: *A possible distribution of the diagnostic elements in the dispersive section, assuming two dipole magnets.*

Beam size in the dispersive section

Assuming condition 4.3 would be fulfilled in the whole dispersive section, the beam size in the x direction (x_{DA}) would depend only on R_{16} and the

relative momentum spread $\frac{\Delta p}{<p>}$. Since equation 4.3 is typically only fulfilled in a small section along the beamline, this is a lower limit of the beam size along the dispersive section. As shown for HEDA1 the momentum spread grows

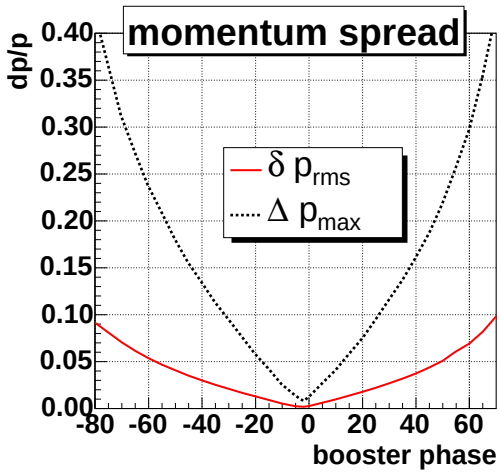

Figure 4.36: *Simulated rms (red, solid line) and total relative momentum spread including head and tail particle (black, dotted line) as a function of the booster phase, for the gun phase with maximum momentum gain.*

much stronger with the booster phase than with the gun phase, therefore the relative momentum spread is shown as a function of booster phase for the gun phase of maximum mean momentum gain in figure 4.36. When a total relative momentum spread including head and tail particle of $\frac{\Delta p}{<p>} = 0.05$ is tolerable for gun phase with maximum momentum gain, a booster phase range of $-17.5°$ to $13.0°$ is usable for long bunch trains at a momentum of about 32 MeV/c. Assuming that a maximum relative momentum spread of $\frac{\Delta p}{<p>} = 0.05$ should fit into a beam pipe of 100 mm, the maximum allowed dispersion along the whole beamline is 2000 mm. Taking into account the aperture of available BPMs or quadrupole magnets of about 80 mm this value is reduced to 1600 mm. Furthermore the influence of initial beam size and divergence is in reality not completely negligible, since it was only optimized for the screen position and for proper focussing conditions. Assuming an influence of beam size and divergence of about 10 mm the maximum allowed dispersion along the dispersive section becomes $D_{max} = 1400$ mm. But one has to take into account that for this dispersion the beam size at a booster phase of $65°$ and $-74°$ becomes about 0.5 m (or larger due to the influence of initial beam size and transverse divergence). This means that during the slice emittance measurement in the dispersive arm, where the application of an off-crest booster phase is required, most of the beam is dumped in the

vacuum chamber, and this means only a very limited number of bunches is allowed to be used. However, the number of electrons which hit the screen and thus the luminous intensity is rather small, and this would require a large number of bunches. A compromise has to be found.

Reference screen

As discussed in section 4.1.1 the usage of a reference screen simplifies the focussing during the momentum measurement to reach a high momentum resolution. There are three screen stations to be considered as a reference screen for HEDA2. There is one screen station downstream of the HEDA2 dipole (see figure 2.4), High2.Scr2. In case the reference screen is before the dipole magnet, L_{SS} becomes negative, assuming $L_{before} = 0$. The closest screen stations in front of HEDA2 are EMSY3 and PST.Scr5 (the last screen of the phase space tomography module). Table 4.4 gives an overview about the usability of each of these as a reference screen[9]. To reach a high

screen	PST.Scr5	EMSY3	High2.Scr2
z-position	15318 mm	16272 mm	18226 mm
L_{SS}	-1950 to -1700	-1028 to -746	926 to 1208
advantages	large ratio of $\frac{R_{16}}{R_{11}}$ → high resolution (but only with proper focussing)	slit available (but only 10μm)	simple focussing for RF deflector meas. - focus point after dipole → avoid space charge effects
dis-advantages	-focus before dipole → space charge forces appear - difficult to focus for RF deflector measurement		- ratio of $\frac{R_{16}}{R_{11}}$ is rather small - dipole has to be degaussed for focussing

Table 4.4: *Overview of possible reference screen stations and their useability.*

resolution for the measurement of longitudinal phase space distribution using the RF deflector, two requirements have to be fulfilled. A small beam size in the horizontal direction on the reference screen for a high resolution momentum measurement is necessary along with a small beam size in the vertical direction on the screen in the dispersive arm at the same time. In

[9]Since the PITZ2 setup is not completely finalized in the design, there is still some flexibility in the position of the dipole spectrometer magnet, therefore the possible values of L_{SS} have a certain range.

case the reference screen is downstream the dipole magnet, the setting of the quadrupole magnets can be adjusted such that a focussing on the reference screen in the straight section also corresponds to a high resolution of the RF deflector. Another possibility is the usage of a vertical opening (i.e. cut in x-direction) slit at the reference position, but of course only for a screen before the dipole. Then the operator has to adjust the beam only in the vertical direction on the screen in the dispersive arm for the highly resolved RF deflector measurements. The slit provides the momentum resolution. Using the existing slit in the EMSY has the main advantage that the focussing is simplified, especially when the RF deflector is used. Also a higher resolution is expected, but a slit width of 10μm is probably too small, meaning another slit width has to be added.

Detailed analysis of selected spectrometers

In this section the design of the first dipole magnet, to be used for measurements of the momentum and longitudinal phase space distribution will be discussed. The properties of the dipole (deflecting angle (α), deflecting radius (r) and entrance and exit pole face rotation (β_{in},β_{out})) have to be defined in dependence on the distance of the dipole to the reference screen in the straight section (L_{SS}) and the drift from the dipole exit to the screen in the dispersive arm. The dependency of these properties can be described applying a combination of equation 4.7 with the description of R_{11} and R_{12} given in equation 4.4:

$$\begin{aligned} L_{DA} =& (\sin\alpha \cdot r - L_{SS} \cdot \cos\alpha - L_{SS} \cdot \sin\alpha \cdot \tan\beta_{in})/ \\ & (\cos\alpha \cdot (\frac{L_{SS}}{r} \cdot \tan\beta_{out} + \frac{L_{SS}}{r} \cdot \tan\beta_{in} - 1) \\ & + \sin\alpha \cdot (\frac{L_{SS}}{r} \cdot \tan\beta_{out} \cdot \tan\beta_{in} - \tan\beta_{out} - \frac{L_{SS}}{r})) \end{aligned} \tag{4.22}$$

When this condition is fulfilled equation 4.2 turns to:

$$x_{DA} = R_{11} \cdot x_{SS} + R_{16}\frac{\Delta p}{p}. \tag{4.23}$$

and the ratio $|\frac{R_{16}}{R_{11}}|$ is the figure of merit for the momentum resolution of such a dispersive section.

In general, a large deflecting radius and angle are preferable, since the influence of fringe fields is smaller . Generally the ratio $|\frac{R_{16}}{R_{11}}|$ increases with the entrance pole face rotation β_{in}, but also with the distance of the dipole

to the reference screen $|L_{SS}|$ and the deflection angle α. For deflecting angles from 0 to 90° the highest values are reached for 90°, but in this case the drift length after the dipole L_{DA} becomes very short for the screen stations upstream the second dipole. A minimum distance of 200 to 250 mm between the dipole exit and the screen is required for technical reasons. In a sector magnet the ratio $|\frac{R_{16}}{R_{11}}| = |r \cdot (\cos\alpha - 1) + L_{SS} \cdot sin\alpha|$ is larger for a negative L_{SS} than for positive (for angles up to 90°) and also higher for PST.Scr5 than for EMSY3 as a reference screen.

Four promising candidates, two magnets with 60° and two with 90° deflecting angle, with a large ratio $|\frac{R_{16}}{R_{11}}|$ and a similar dispersion have been chosen for each reference screen, their properties are listed in table 4.5. The magnets for each reference screen are serially numbered (nr.: 1-4). This numbering is used in the following discussion. For HIGH2.Scr2 as reference screen

screen	nr.	α	β_{in}	β_{out}	L_{SS} (mm)	r (mm)	L_{DA} (mm)	R_{16} (mm)	$\|\frac{R_{16}}{R_{11}}\|$
PST.Scr5	1	60	0	0	-1950	600	645.74	859.2	1989
PST.Scr5	2	60	30	-30	-1950	750	865.87	874.9	2627
PST.Scr5	3	90	0	0	-1700	640	240.94	880.9	2340
PST.Scr5	4	90	30	-24.21	-1950	650	420	881.2	3724
EMSY3	1	60	0	0	-1000	490	729.33	876.6	1111
EMSY3	2	60	30	-29.57	-1000	600	800	765.8	1455
EMSY3	3	90	0	0	-1000	560	313.6	873.6	1560
EMSY3	4	90	30	-29.45	-1000	680	500	897.7	2257
HIGH2.Scr2	1	60	30	24.51	1200	550	624.04	957.7	1110
HIGH2.Scr2	2	60	30	21.14	1200	620	550.74	893.4	1076
HIGH2.Scr2	3	90	45	1.93	1200	570	304.65	884.9	1830
HIGH2.Scr2	4	90	45	17.92	1000	445	301	843.3	1555

Table 4.5: *Different possible spectrometer magnets optimized to use PST.Scr5, EMSY3 or HIGH2.Scr2 as a reference screen, which are analysed in more detail.*

no useful sector magnet could be found. An electron bunch at the entrance of the dipole obtained by ASTRA simulations was multiplied by all the corresponding transport matrices, to estimate the reachable resolution. The ASTRA simulation (1 nC, gun and booster phase of maximum mean momentum gain, flat-top longitudinal laser distribution with 2 ps rise times) was performed such that the focussing at L_{SS} was realized.

Figure 4.37 shows the initial momentum distribution and the expected

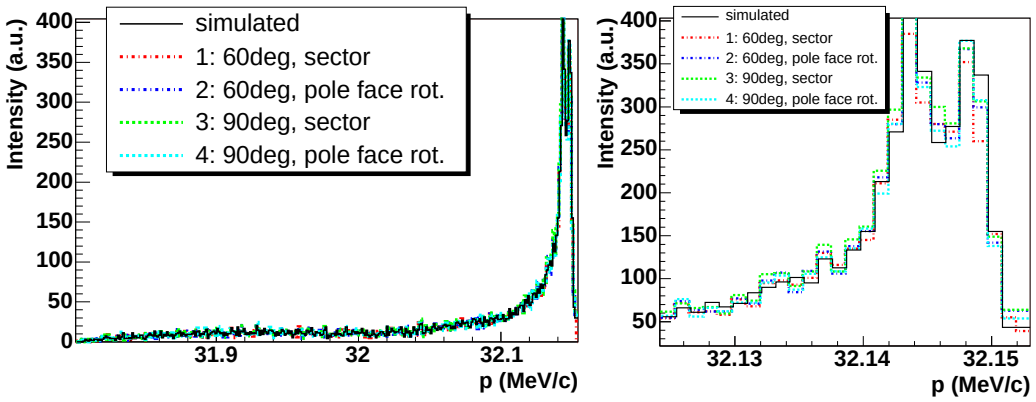

Figure 4.37: *Comparison of simulated momentum distributions with those reproduced (by applying the matrix formalism) by the different spectrometers using PST.Scr5 as a reference screen. The left figure shows the whole distribution, in the right one the high energetic spike is shown in more detail.*

distributions on the screen in the dispersive section for the four magnets using PST.Scr5 as a reference screen. The agreement between the expected momentum measurement and the original simulated momentum distribution is very good for all candidates. Table 4.6 shows the deviation of the reproduced distributions after tracing trough the dipole. This includes only effects of initial beam size (in reality these values would be much larger due to effects of optics and camera). These values give an upper limit of the reachable resolution, since fringe field effects are completely neglected.

The mean momentum of the distribution in figure 4.37 was determined to be 32.08 MeV/c, and the relative error of the mean momentum measurement due to the initial beam size can be found in the column labeled with $\frac{\delta<p>}{<p>}$ of table 4.6. The initial momentum spread of the distribution is 89.54 keV/c, and $\frac{\delta p_{rms}}{p_{rms}}$ is the relative error of the momentum spread measurement. These values are extremely good for all candidates. In reality such a resolution is hardly reachable since field inhomogeneities and fringe fields are neglected in the calculation. More demanding are the requirements of the measurement of the longitudinal phase space distribution. Figure 4.38 shows the expected reproduced longitudinal phase space distribution by RF deflector measurement compared to the simulated one for the 60° sector magnet using PST.Scr5 as a reference screen. The influence of the resolution of the RF deflector was limited to the initial beam size, since this has an impact to the magnet design which should be discussed here. The color coding is the same as in the momentum distribution (Fig. 4.37). The curves seem to agree rather well, and only at the head and the tail of the bunch small differences

screen	nr.	$\frac{\delta<p>}{<p>}$	$\frac{\delta p_{rms}}{p_{rms}}$	$\frac{\delta p^{min}_{slice\,rms}}{p^{min}_{slice\,rms}}$
PST.Scr5	1	$-9.5 \cdot 10^{-7}$	$4.33 \cdot 10^{-5}$	0.32
PST.Scr5	2	$-3.6 \cdot 10^{-7}$	$2.23 \cdot 10^{-5}$	0.19
PST.Scr5	3	$-9.5 \cdot 10^{-7}$	$2.94 \cdot 10^{-5}$	0.24
PST.Scr5	4	$-2.4 \cdot 10^{-7}$	$0.94 \cdot 10^{-5}$	0.12
EMSY3	1	$5.9 \cdot 10^{-7}$	$14.71 \cdot 10^{-5}$	0.94
EMSY3	2	$1.2 \cdot 10^{-7}$	$8.21 \cdot 10^{-5}$	0.55
EMSY3	3	$1.2 \cdot 10^{-7}$	$7.13 \cdot 10^{-5}$	0.59
EMSY3	4	$11.9 \cdot 10^{-7}$	$3.30 \cdot 10^{-5}$	0.27
HIGH2.Scr2	1	$8.8 \cdot 10^{-6}$	$7.41 \cdot 10^{-4}$	4.61
HIGH2.Scr2	2	$10.0 \cdot 10^{-6}$	$9.72 \cdot 10^{-4}$	4.46
HIGH2.Scr2	3	$6.8 \cdot 10^{-6}$	$2.65 \cdot 10^{-4}$	2.97
HIGH2.Scr2	4	$6.4 \cdot 10^{-6}$	$4.80 \cdot 10^{-4}$	4.01

Table 4.6: *Expected deviations in the mean momentum ($\frac{\delta<p>}{<p>}$), momentum spread ($\frac{\delta p_{rms}}{p_{rms}}$) and slice momentum spread ($\frac{\delta p^{min}_{slice\,rms}}{p^{min}_{slice\,rms}}$) measurements compared to the values of the initial distribution due to the initial beam size, determined by matrix formalism, for the spectrometers introduced in table 4.5.*

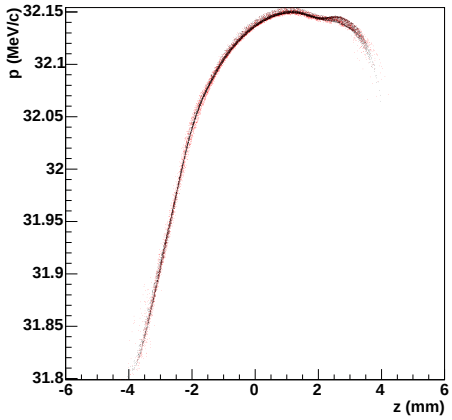

Figure 4.38: *Expected reproduced longitudinal phase space distribution of the bunch by RF deflector measurements (red) compared to the simulated one (black) for the 60° sector magnet (nr.: 1) using PST.Scr5 as a reference screen.*

appear. To determine the difference in detail, the reproducibility of slice momentum spread for the different spectrometers is shown in figure 4.39.

The reproduced slice momentum spread fits reasonably well in the center

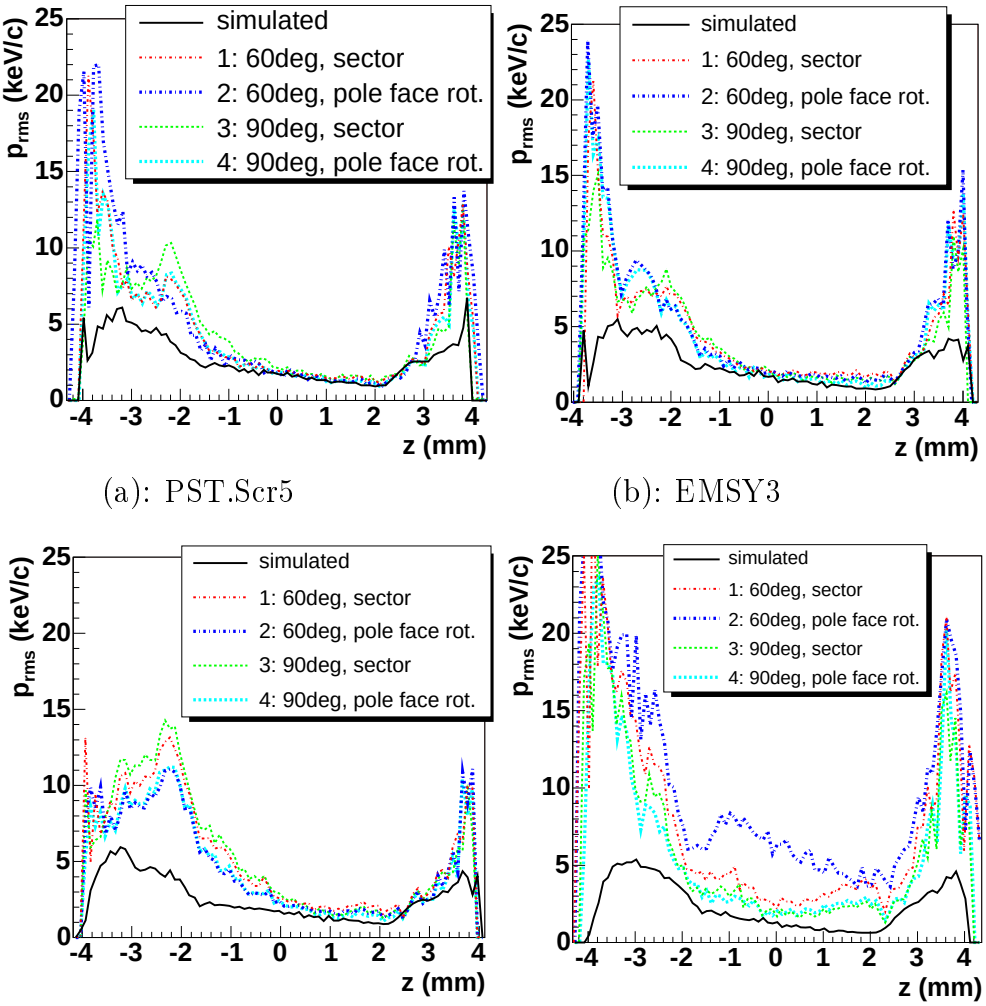

(a): PST.Scr5 (b): EMSY3

(c): EMSY3 (d): HIGH2.Scr2

Figure 4.39: *Expected measurement results of the slice momentum spread by RF deflector measurements compared to the simulated one for PST.Scr5 (a), for EMSY3 using different focussing (b, c) and HIGH2.Scr2 (d).*

of the bunch, which contains a major part of the charge, but there is a strong discrepancy in the head and the tail. This is due to the focussing properties of the quadrupole, as only a certain energy (32.12-32.15 MeV/c) is focused at the required position. The deviation of the slice momentum spread for the slice at z=2.2 mm (in the minimum) is shown in the last column ($\frac{\delta p^{min}_{slice\,rms}}{p^{min}_{slice\,rms}}$) of table 4.6. The results in the table agree with the expectation from the ratio $|\frac{R_{16}}{R_{11}}|$ (see table 4.5): 90° deflecting angle (nr.: 3,4) performs

better than 60° (nr.: 1,2) and magnets with pole face rotation perform better than sector magnets. But actually the performance does not differ that strongly, especially in the tail. For EMSY as a reference screen two slightly different quadrupole fields were applied (figure 4.39(b),(c)), to test whether the resolution in the head and tails can be improved.

Since for the usage of HIGH2.Scr2 as a reference screen (figure 4.39(d)) both transverse directions are focussed at one point the reached projected beam size is not as small as for separate focussing. This degrades the resolution. The resolution of the slice emittance is worse for the 90° magnet (case: nr. 4) using HIGH2.Scr2 as a reference screen than for the 90° magnet (case: nr. 3) using EMSY (see table 4.6 and figure 4.39) although the ratio $|\frac{R_{16}}{R_{11}}|$ of both is similar (see table 4.5).

The resolution is higher for the screens upstream the dipole than downstream. The best results are reached for a focussing at PST.Scr5. For the 90° deflection angle the space along the drift section is very limited, therefore the 60° magnets are preferred. Since the slice momentum spread resolution along the bunch shown in figure 4.39(a) does not differ strongly between the sector magnet and the magnet using large pole face rotation, the sector magnet is preferred. For this spectrometer (60° sector magnet using PST.Scr5 as a reference screen) the possibility of the usage of a Cherenkov radiator or OTR screen observed by a streak camera for the measurement of the longitudinal phase space distribution is investigated. This measurement is mainly interesting by methodical reasons, since the RF deflector features a high-resolution measurement of the longitudinal phase space distribution.

For the reproduced longitudinal phase space distribution that will be used by the streak measurements shown in figure 4.40 (a) only effects of the dipole magnet are included (the resolution of radiator, the optical system and the streak have not been taken into account) because the optimization of the dipole magnet is studied here. Since the spectrometer was optimized for measurements of the longitudinal phase space distribution using RF deflector, the influence of R_{51} and R_{52} have not been taken into account during the optimization process, and thus the resolution for the streak measurement for focussing on the reference screen is low. By changing the focussing the temporal resolution could be improved, but the momentum resolution would become worse and the resulting resolution of the longitudinal phase space distribution cannot be improved. A slit could help to improve the resolution because the slit could be used to reach the high momentum resolution and the quadrupoles could be adjusted to reach a high temporal resolution. The resolution reached with a slit (of 0.1 mm) is presented in figure 4.40 (b), which would be sufficient for streak measurement since other contributions will deteriorate the resolution. The only problem is that the number of

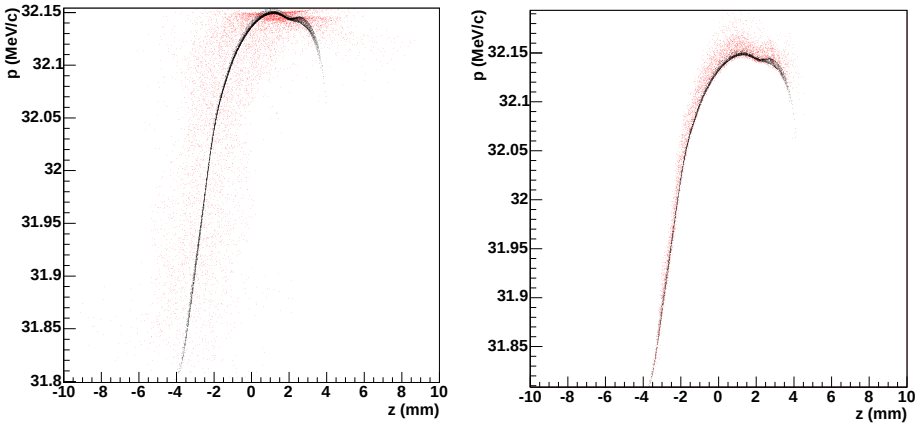

(a) (b)

Figure 4.40: *Expected reproduced distribution of the bunch in the longitudinal phase space after tracing the bunch through the spectrometer dipole magnet, that will be used by the streak measurements (red) compared to the simulated one (black) for the* 60° *sector magnet using PST.Scr5 as a reference screen (presented in table 4.5), without (a) and with (b) applying a slit at PST.Scr5. For the reproduced measurement only effects of the dipole magnet are included.*

electrons passing the slit will be reduced, but in LEDA it was shown that the number of produced photons using a slit is still sufficient for measurements.

4.4 Optical transmission line

4.4.1 Description of the current optical transmission line

The light pulses produced by the radiators of the different screen stations for measurements of the temporal and longitudinal phase space distribution are transported to the streak camera by an optical transmission line with a length of about 30 m, consisting of several lenses and plane mirrors [Bae03]. Figure 4.41 gives an overview of the current state of the transmission line. The optical system consists of several branches of input optics, a commonly used optical system with a magnification of 1 and a demagnifying system. The system is modular and can easily be extended. The light distribution has to be imaged onto the entrance slit of the streak camera. The typical dimensions of the streak camera slit are 6 mm times 0.01 - 0.1 mm. The light transport in the transmission line for the bunch length measurement has to

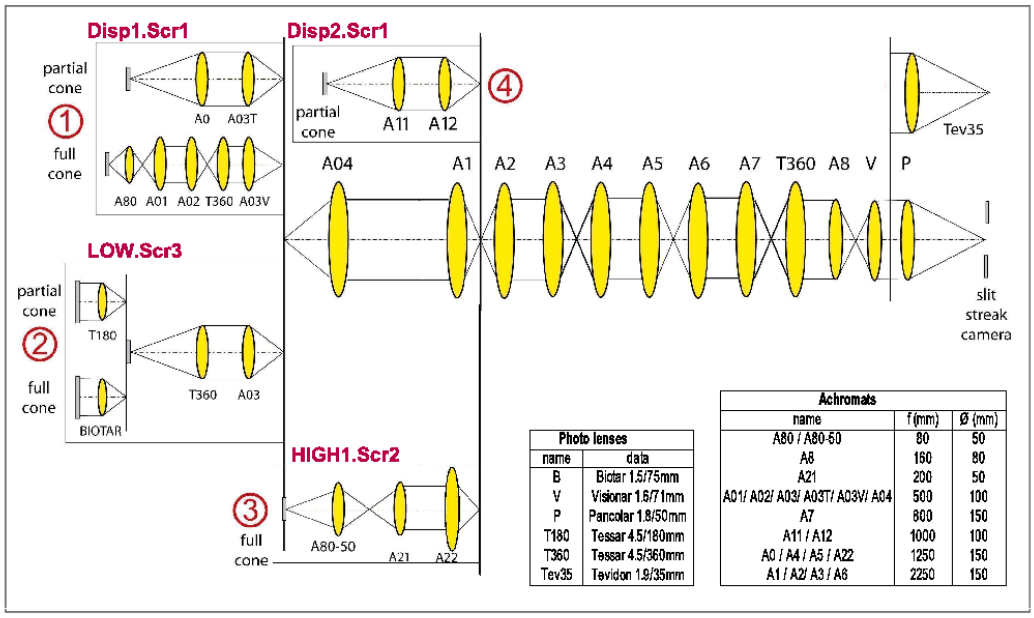

Figure 4.41: *Schematic overview of the current optical transmission line from different screen stations to the streak camera.*

conserve the temporal distribution of the light. For the measurement of the complete longitudinal phase space distribution the spatial distribution must also be conserved, thus an appropriate magnification and spatial resolution is required. But also for the bunch length measurement an imaging system is important in order to collect and transport all the emitted light in order to measure it. Therefore, for each screen station a suitable overall magnification has to be realized. Further demands to the optical imaging are a high light collection and transmission efficiency and especially a minimum time dispersion of the light passing the optical transport line.

The main part of the optical system consists of achromatic lenses[10] of large focal length forming telescopes with 4-f geometry[11] (see figure 4.42), to image the extended object distribution over a large distance. These lenses

[10] Achromatic lenses are corrected to focus two different wavelengths (typically red and blue light) into the same plane, to correct chromatic aberration.

[11] The light emitted by an object point located in the focal point of a lens is transformed into a parallel bundle by the lens. For an object point with an offset from the optical axis, this bundle is not parallel to the optical axis. The second lens of the telescope is placed in a distance equal to the sum of the focal lengths (f) of both lenses and the object is imaged into the focal point of the second lens, in a distance of four focal lengths to the object point (4-f geometry). This distance is optimized for minimal light losses.

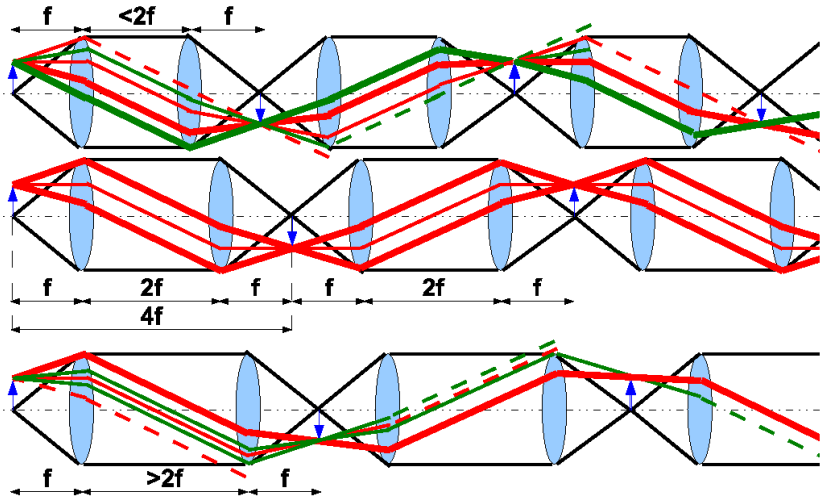

Figure 4.42: *Schematic of the imaging of an off-axis point with an optical system with 4-f geometry (center) and two systems (top, bottom) which violate the 4-f condition. When a couple of telecopes are used, which does not fullfil the 4-f condition, strong losses (doted lines) appear.*

(A1 - A6) have a rather large f-number[12]. Therefore the aperture of the light coming from the light collection system has to be matched to the lenses by magnification. The input optics for full cone measurement is initiated by magnifying imaging with lenses of a very small f-number (Biotar: $f_N = 1.5$, A80: $f_N = 1.6$), to collect the whole Cherenkov cone. The matching system at the end of the beam line (A7 - Pancolar/Tevidon) de-magnifies the images of the beam distribution such that the image fit to the streak camera slit dimensions, and its aperture matches to the aperture of the internal optics of the streak camera. An image rotating box is used to turn the image of the low energy dispersive arm by 60° to fit the momentum distribution to the streak camera slit orientation.

4.4.2 Characterization of the optical system

The optical transmission line causes a time dispersion, principally due to chromatic effects of the lenses, which leads to an overestimation of the bunch length, a bunch of 20 - 30 ps bunch duration being elongated to 50 - 60 ps. Figure 4.43 (a) shows the measured light pulse duration depending on the

[12]The f-number of an optical system $f_N = \frac{f}{D}$, where f is the focal length and D is the diameter of the entrance pupil. The greater the f-number, the smaller the acceptance angle.

number of lenses in the optical transmission line. As a rough estimation about 2 ps elongation (of the FWHM) of the pulse length per lens can be assumed. This effect can be reduced by using a spectral transmission filter with a

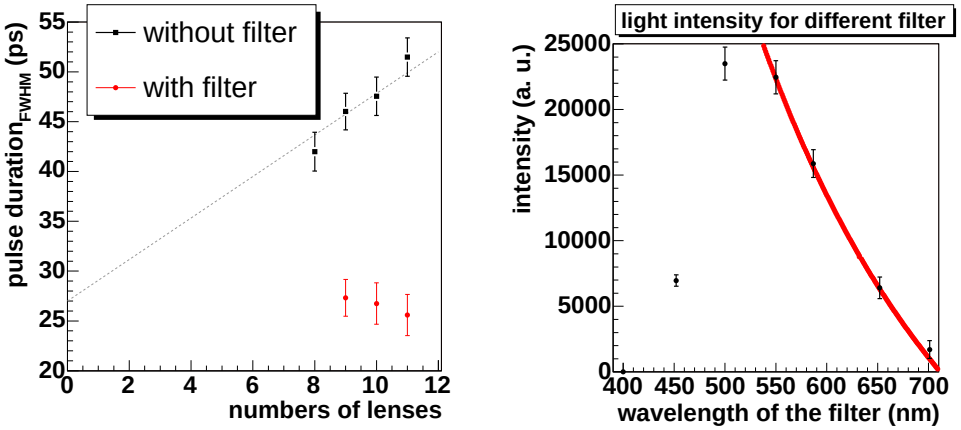

Figure 4.43: *Measured light pulse duration, with and without optical transmission filter for different numbers of lenses in the optical transmission line between the Cherenkov radiator and the streak camera (a). Measured light intensity using optical transmission filters with different central transmission wavelengths, a bandwidth of 10 nm and a transmission of 60%, for LOW.Scr.3 (b).*

small bandwidth. In figure 4.43(a) the bunch durration was defined using the spectral transmission filter with 27±2 ps. An elongation of the curve of the bunch durration as a function of the lens number down to zero lenses leads to about the same result. The maximum light intensity is typically reached for 500 to 550 nm, as figure 4.43 (b) shows. Therefore this wavelength range is preferred for the measurement. The expected number of emitted photons (equation 4.15) was matched to the measured light intensity. For wavelengths smaller than 550 nm the transmission of the lenses decays and the number of photons reaching the streak camera is reduced.

Beside the dispersion the sensitivity of the glass lenses to radiation damage is another disadvantage. In 2007, when gun 3.1 (see Appendix B) was conditioned and characterized the level of dark current was very high and the optics (close to the gun) turned brown, which made measurements impossible in the low energetic region. The transmission of some lenses decayed to less than 1% from the initial value at a wavelength of 500 nm. A recovery of most lenses to about 90% of the initial value could be reached by baking the lenses at temperatures up to 200°C.

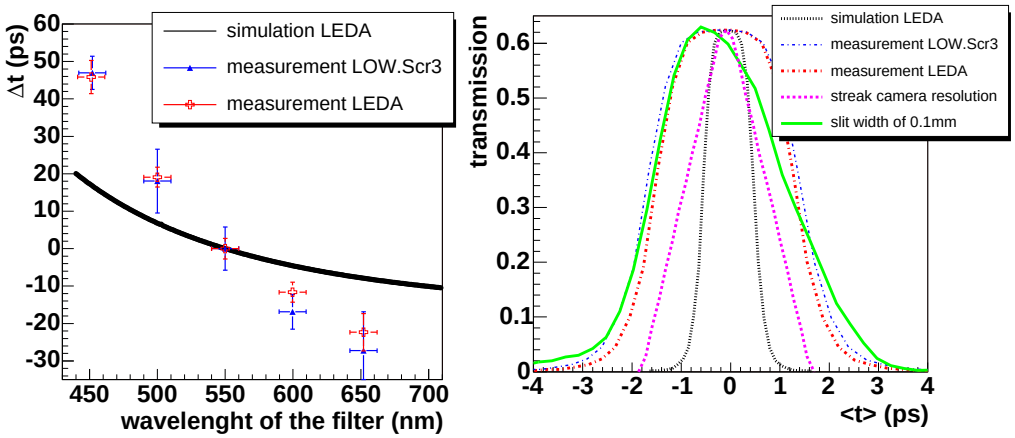

(a) (b)

Figure 4.44: *Measured and simulated variation of arrival time of the photons of the Cherenkov light at the streak camera $\Delta t(\lambda)$ using different spectral transmission filters (a) and the resulting temporal resolution by using 10 nm bandwidth filter compared to the streak camera resolution (b).*

Figure 4.44 (a) shows two examples (for LOW.Scr3 and LEDA) for the arrival time measured by the streak camera using different spectral transmission filters with a bandwidth of 10 nm. For a wavelength of 550nm the arrival time was defined as 0, thus the arrival time of a photon of a certain wavelength is plotted as the difference in travelling time of this wavelength to 550 nm $\Delta t(\lambda)$: $\Delta t(\lambda) = t(\lambda) - t(550\,nm)$. For one example (LEDA) it is compared to simulations using optical ray tracing. The measured time dispersion is larger than the simulated one. The simulated arrival time matches rather well to the simple estimation of a ray traveling on the optical axis, which can be determined by: $t(\lambda) = \frac{1}{c}\int n(\lambda)dl$, with $\frac{c}{n(\lambda)} = v(\lambda)$ being the different velocity of light for different wavelengths. l is the traveling distance. The influence of the angle of incidence is small and cannot explain the difference between the measurement and the simulation. In the simulation the dispersion in air [Edl66, BD93, BD94] and the exit windows of the screen stations is not included, but these effects are in the order of 1-2 ps. Also the dispersion in the aerogel is small. The thicknesses of a sample of lenses were measured and compared to the catalogue values and the difference is less than 1%. Also a misalignment of optical elements cannot explain such a difference. The optical transmission filters used for the measurement are made from unknown material and are not taken into account for the simulations, but from the measurement without filter presented in figure 4.43 one can ex-

clude the optical transmission filter as the reason for the difference between measurements and simulations, so that the deviation between measurement and simulation is still not explained.

Figure 4.43 shows that the main part of the light is emitted within the wavelength range from about 480 nm to 600 nm, which is mainly responsible for the elongation of the bunch. This corresponds to the measured difference in the arrival time of these two wavelengths of about 40 ps, which is about the elongation of the bunch. In figure 4.44 (b) the results from (a) are applied to the transmission curve of the 550 nm filter in order to determine the resolution of the transmission line when the filter is used. For the measured curve the resolution was determined as $\delta t_{rms} = 1.15\,\text{ps}$ for LOW.Scr3 and as $\delta t_{rms} = 1.04\,\text{ps}$ for the screen station in LEDA. From the simulation the resolution of the optical transmission line itself, when using the 550 nm filter with a bandwidth of 10nm, is estimated to be $\delta t_{rms} \approx 0.4\,\text{ps}$ for the screen station in LEDA.

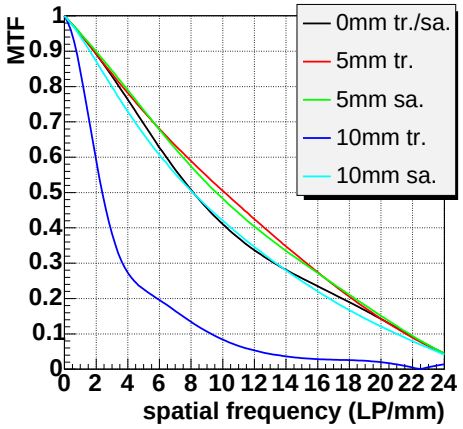

Figure 4.45: *Simulated* M*odulation* T*ransfer* F*unction (MTF) for the screen station in LEDA, different conditions for the range of 545-555 nm, offset from optical axis in mm, sa: sagittal, tr: transversal.*

Beside the temporal resolution also the spatial resolution was analysed. For the screen station in LEDA the simulated *M*odulation *T*ransfer *F*unction (MTF)[13] is shown in figure 4.45. Spatial frequencies with an MTF larger than 10% are expected to be resolvable. The figure shows a spatial resolution of 9 Lp/mm (line pairs per mm) for a 10 mm off-axis point. For on-axis points the resolution is above 20 Lp/mm. The transverse resolution of the system

[13]The modulation transfer function is the spatial frequency response of an imaging system, it describes the contrast of the image relative to the object at a given spatial frequency.

was measured to be 3 Lp/mm, but the resolution was limited by the pixel size of the used CCD-camera and thus a measurement of higher values was impossible.

The usage of apochromatic lenses[14] instead of achromatic lenses was investigated. The spatial resolution can be improved but the temporal resolution is comparable. Singlets are typically thinner than achromats, thus the difference in the traveling time on the optical axis can be reduced, but in this case the temporal resolution is dependent on the aperture and two effects start to mix. Additionally, the transverse resolution of singlets is much worse than for achromats.

4.4.3 Design considerations for an optical transmission line consisting of reflective optics

The goal of the design of the optical system is to reach a temporal resolution of the whole system which is smaller or at least comparable to the temporal resolution of the streak camera, i.e. about $\delta t_{FWHM} = 2\,\text{ps}$. The restriction of the spectral bandwidth results in a large loss of light. To improve the situation significantly, refractive elements must be exchanged by reflective elements that do not cause any chromatic effects. Different types of mirror telescopes with an 1:1 imaging, which are shown in figure 4.46, were analysed for PITZ in [Ros08]. An overview of the results for different systems with comparable dimensions is shown table 4.7. In addition, a telescope of achromatic lenses with similar dimensions is added to the table, to judge the quality. For the achromats a wavelength range of $550 \pm 25\,\text{nm}$ was taken into account. The following properties were analysed:

- the length efficiency (Σ_{length}), which is the ratio of the distance from the object to the image point, also called effective optical path length ($\frac{\Delta t}{l_{eff}}$) and the optical path length passed by the photons,
- the temporal resolution (the complete width of the distribution is taken into account) per effective optical path length ($\frac{\Delta t}{l_{eff}}$),
- the transverse resolution on the optical axis (trRes_{0mm}) and 5 mm offset (trRes_{5mm}),
- the area with a relative light transfer efficiency larger than 50% ($\Sigma_{il-50\%}$),

[14] Apochromatic lenses are corrected to focus three different wavelengths (typically red, blue and green light) in the same plane. They provide a better correction of chromatic aberration than achromats.

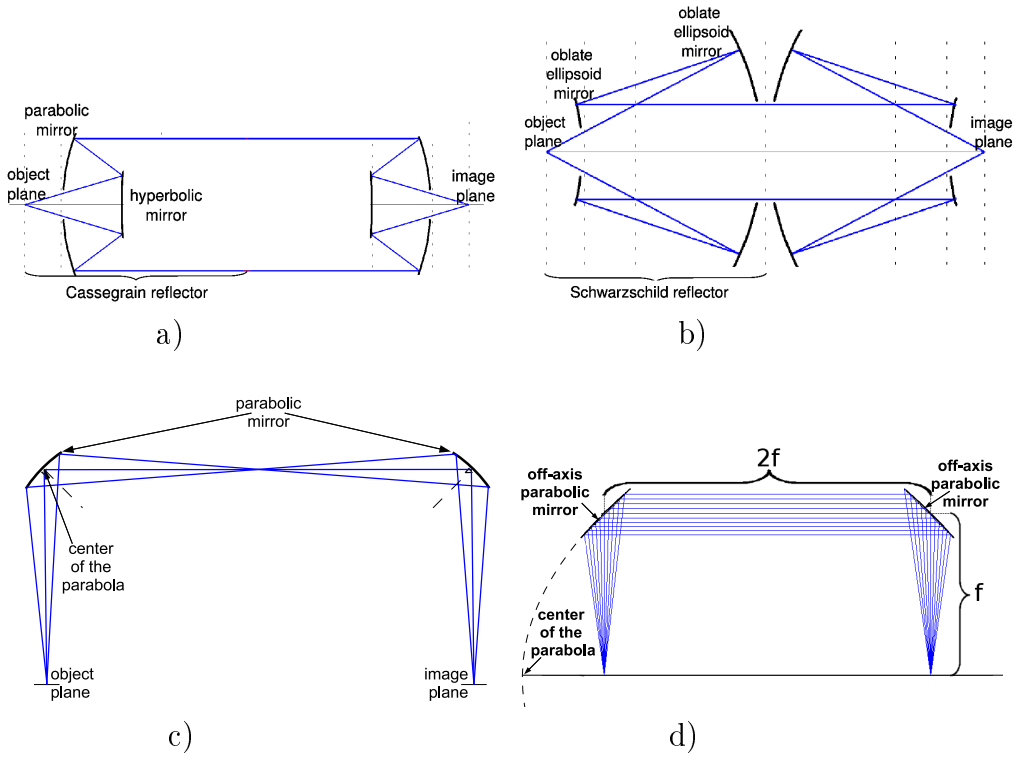

Figure 4.46: *Layout of different mirror telescopes (Cassegrain telescope (a), Schwarzschild telescope (b), telescope based on on-axis parabolic mirrors (c) and telescope based on off-axis parabolic mirrors (d)) with a 1:1 magnification.*

- the light collection efficiency for an object of 2 mm × 2 mm ($\Sigma_{coll-2x2\,mm^2}$) and
- the angular acceptance ($\Delta\varphi$).

The Cassegrain telescope (figure 4.46 a) consists of two oppositely oriented Cassegrain reflectors. The Cassegrain reflector consists of a hyperbolic and a parabolic mirror. The light emitted by the object passes a hole in the parabolic mirror before it is reflected by the hyperbolic mirror towards the parabolic mirror. The light reflected by the parabolic mirror passes around the hyperbolic mirror. It becomes clear that the angular acceptance of this system is limited by the design [Ros08]. This effect already occurs for an object point on the optical axis. For an extended object it becomes even more critical. It delivers a very high temporal and transverse resolution and an acceptable length efficiency.

properties	Achro-mats	Cassegrain telescope	Schwarz-schild telescope	On-axis parabolic mirrors	Off-axis parabolic mirrors
$\frac{\Delta t}{l_{eff}}$ $(\frac{fs}{m})$	340	0.2	970	140	1.8
trRes_{0mm} $(\frac{LP}{mm})$	170	145	400	30*	135
trRes_{5mm} $(\frac{LP}{mm})$	170	100	150	30	135
$\Sigma_{il-50\%}$ (mm^2)	31x31	8.4x8.4	3.2x3.2	14x52	40x52
$\Sigma_{coll-2x2\,mm^2}$	98.9%	57%	25%	98%	100%
Σ_{length}	99%	63%	38%	95%	81%
$\Delta\varphi$	0-3.4°	1.7-2.6°	5.6-8.1°	0-2.3°	0-2.7°

Table 4.7: *Summary of the simulation results of different mirror telescopes with a 1:1 magnification [Ros] compared to a telescope of achromats, which is part of the current optical transmission line. The properties of the systems are describes by:* $\frac{\Delta t}{l_{eff}}$*: the temporal resolution per effective path length,* $trRes_{0mm/5mm}$*: the transverse resolution for an object point on the optical axis (0 mm) and an object point with 5 mm offset from the optical axis,* $\Sigma_{il-50\%}$*: the area with a light transfer efficiency larger than 50%,* $\Sigma_{coll-2x2\,mm^2}$*: the light collection efficiency (object: 2 mm × 2 mm),* Σ_{length}*: the length efficiency and* $\Delta\varphi$*: the angular acceptance.*

The Schwarzschild telescope (figure 4.46 b) is free of spherical aberration, astigmatism, field curvature and coma, thus it delivers a tremendous spatial resolution on the optical axis. Unfortunately the object size that can be imaged is very limited, the length efficiency is low and the temporal resolution is unacceptable [Ros08].

The telescope based on on-axis parabolic mirrors (figure 4.46 c) features a high collection and length efficiency, but it delivers an insufficient temporal resolution and the worst transverse resolution, since it is highly astigmatic. Since its elements are commercially available, this system was tested as a first step, in order to prove the simulation results. The transverse resolution reached in simulations corresponds to the experimental results [Bae07].

The telescope based on off-axis parabolic mirrors (figure 4.46 d) seems to meet best the requirements of the optical system at PITZ that have a magnification of 1 and it is foreseen to test the applicability experimentally. For a magnification unequal 1, which is required for the initial magnification and the final demagnification of the image, the effect of coma cannot be compensated using parabolic mirrors and the resolution becomes worse [Ros].

4.5 The properties of the streak camera used at PITZ

Several effects influence the resolution of the streak camera (HAMAMATSU, C5680 [Ham04]). The electrons produced by the photo cathode of the streak camera have a momentum distribution. Therefore the electrons need different times to reach the streak tube. The contribution to the temporal resolution is [Lip04]: $\delta t_1[\mu\text{s}] = 2.34 \cdot \frac{\sqrt{\delta E[\text{eV}]}}{E_k[\text{V/m}]}$, where the energy spread of the electrons produced by the photo cathode of the streak camera is δE and the accelerating gradient on the photo cathode is E_k. For the model C5680 the value is: $E_k = 1.5 \cdot 10^6\,\text{V/m}$. The energy spread of the electrons depends on the cathode material and the wavelength of the light pulse to be measured. For a wavelength of $\lambda = 800\,\text{nm}$ δt_1 (FWHM) is less than 0.4 ps and for $\lambda = 250\,\text{nm}$ δt_1 (FWHM) is about 2.2 ps [Ham08].

Also the temporal spread of the photoelectrons produced in the streak camera (δt_2) influences the total temporal resolution of the streak camera.

As a third point the spatial spread (δt_3) of the initial distribution contributes to the total temporal resolution of the streak camera. The streak camera slit width smears the signal, this causes an error in the temporal distribution. An additional smearing is produced by space charge forces of the photo electrons for a high photon density. The slit width should be small to reduce the error due to the slit width and space charge, but big enough to have a sufficient signal intensity in comparison to the noise. A typical slit width for the measurement of the laser signal is $<$ 5-20 μm, for the Cherenkov light 50 to 100 μm. The influence can be estimated by measuring the signal without RF field on the streak tube and convert it to the used time scale. In figure 4.44(b) the green curve shows such a measurement for a slit width of 0.1 mm. In figure 4.47 the FWHM of the distribution of the CHerenkov light measured in this way was determined as a function of the slit width for a Cherenkov signal measured with and without filter. The signal without filter is 25 times stronger. Since both curves show about the same results one can conclude that the measurement was not done in the space charge dominated regime.

Additionally to the internal error sources phase jitter of the streak camera and its subcomponents as well as the signal to be measured can influence the temporal resolution.

The total error of the HAMAMATSU C5680 streak camera is about 1.7 ps for a wavelength of 800 nm and 2.7 ps for a wavelength of 250 nm [Ham08].

A correction of the smeared signal requires a deconvolution from the response function. For the measurement of the bunch length it is sufficient

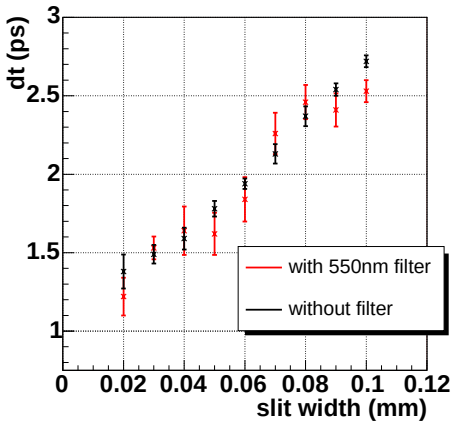

Figure 4.47: *Influence of streak camera slit width on the temporal resolution (FWHM) of the camera for the streak field with the highest resolution. It was measured for a Cherenkov pulse with and without spectral transmission filter.*

to deconvolute only the temporal projection. The measured longitudinal phase space distribution has to be deconvoluted for every momentum value.

Additionally the influence of the streak camera internal noise and the signal background have to be subtracted. The streak camera shows a horizontal sensitivity inhomogeneity which, especially for the measurement of longitudinal phase space distribution, has to be corrected. Additionally a curvature along the horizonal axis is visible. It seems to be caused by the RF field slightly varying in the horizontal direction, which causes a delay of non-central electrons. Both effects can be corrected by applying quadratic functions [Rön05].

Chapter 5

Measurements and simulations of the bunch distribution in the longitudinal phase space at PITZ

5.1 Influence of the gun launch phase

The synchronization between the laser and the RF system is of high importance. The RF launch phase, ϕ (defined in equation 2.12) is a major optimization parameter. Figure 5.1 shows the measurements and the simulations of mean momentum and momentum spread as a function of the RF launch phase of the gun. For the simulation a gradient of 55 MV/m at the cathode has been used and the longitudinal distribution of the drive laser as determined with the streak camera was applied. The error bars of the momentum spread measurement result from statistical and systematic errors. The systematic errors of the momentum spread measurement mainly arise from the initial transverse beam size and the divergence of the bunch (see equation 4.5). For the mean momentum measurement, systematical errors which apply to all phases used in this momentum measurement, like the uncertainty of the deflection angle and the alignment, have not been taken into account, since the gradient of 55 MV/m used in the simulation was not obtained from measurements, but fitted to match the momentum measurement. The mean momentum of the electron bunch is mainly determined by the RF field, and the influence of space-charge to the mean momentum is rather small, as will be shown in section 5.3. A maximum mean momentum of 6.38 MeV/c was reached at a phase of about 43° in this measurement, which corresponds to an accelerating gradient of about 55 MV/m for a field balance (FB) of 1.03 (the field balance was determined during the tuning

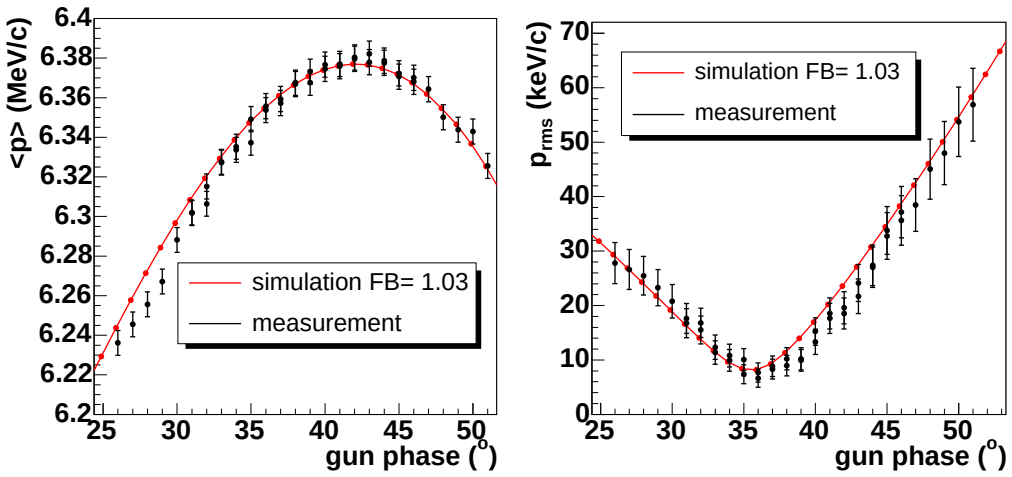

(a) (b)

Figure 5.1: *Measured and simulated mean momentum (a) and momentum spread (b) as a function of the RF gun phase. The measurement was performed for gun prototype 3.2 using a solenoid field adjusted for a high resolution momentum measurement (about 275 mT), 1 nC, for a transverse and longitudinal flat top laser distribution with 2 mm aperture diameter and a pulse duration of 20 ps FWHM with about 7 ps rise and fall time.*

of the gun and is listed in Appendix B for each gun). Figure 5.2 shows the simulated mean momentum of the electron bunch (for same the conditions as in figure 5.1) and the mean energy gain of the bunch per unit length along the longitudinal distance z of the bunch center to the cathode surface, for bunches with different emission phases. The electrons leaving the Cs_2Te cathode, produced by the 262 nm laser beam, have in absence of an electric field according to the band gap model an average kinetic energy of 0.55 eV. Up to now this value could not be confirmed in measurements done at PITZ, applying gradients up to 43.2 MV/m at the cathode during the emission.

For the emission, at a launch phase of $\phi = 90°$ (shown in blue in figure 5.2) the accelerating field will change its polarity before the non-relativistic electron bunch has reached the end of the half cell, and the electron bunch is thus slightly decelerated before it reaches the full cell. When the beam has reached the center of the full cell, where the standing wave has its maximum, the field has already strongly declined, and the bunch will be decelerated again at the end of the full cell. For an RF phase of about 63° (shown in magenta in figure 5.2) the field changes the polarity exactly when the beam passes the iris, but the highest energy is reached for an RF phase of $\phi = 43°$

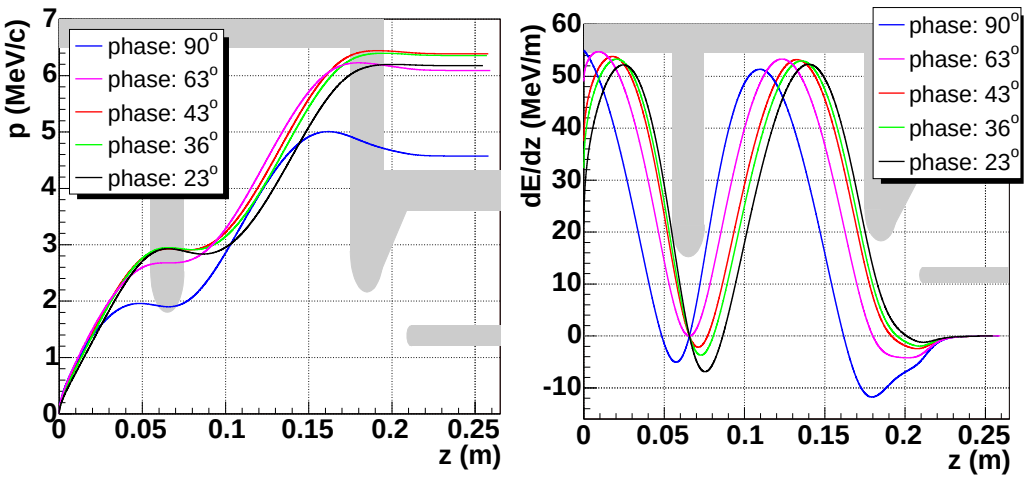

(a) (b)

Figure 5.2: *Simulated mean momentum (a) and the mean energy gain of the bunch per unit length (b) exposed to the electron bunch along the longitudinal position within the gun for different emission phases. In the background of the figure the geometry of the gun cavity is displayed.*

(shown in red in figure 5.2), since for $\phi = 43°$ the momentum gain in the half cell is higher than for $\phi = 63°$, while the momentum gain and losses in the full cell are comparable. For $\phi = 36°$ (shown in green in figure 5.2), the RF launch phase of minimum momentum spread, the momentum gain in the half cell is comparable with 43°, but the total energy gain in the full cell is reduced. The difference in the mean momentum between the phase of maximum momentum gain and the phase of minimum momentum spread is only about 20 keV/c, but the difference in momentum spread is about a factor of 2.

In figure 5.3 (a) the development of the energy spread along the gun cavity is shown (for the same conditions as in figure 5.1). On the abscissa the longitudinal distance z of the bunch center to the cathode surface is given. The solid lines presents the results from the simulations already considered in figure 5.2 for the same emission phases. The dotted lines show the simulated rms energy spread not taking into account space-charge forces to distinguish between effects of RF and space-charge forces. In this plot the particles in the tail of the bunch are a shorter time exposed to the RF field then the particles in the head, but nevertheless they interact with each other. For all presented phases, the energy spread increases after emission up to a longitudinal position of about $z = 20$ mm downstream the cathode. This

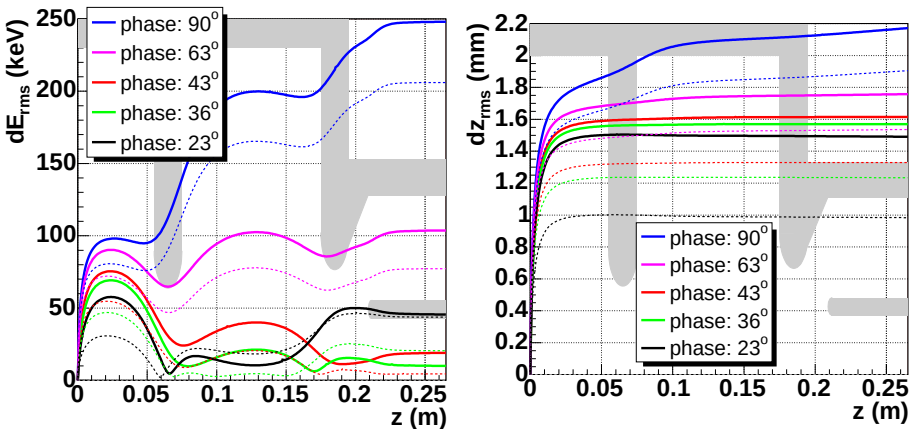

(a) (b)

Figure 5.3: *Development of energy spread (a) and bunch length (b) in the RF gun for different RF phases. The solid lines show the simulations taking space-charge into account, and the dotted line presents the results excluding space-charge forces. The ASTRA simulation was performed for 1 nC, for a transverse and longitudinal flat top laser distribution with 2 mm aperture diameter and a pulse duration of 20 ps FWHM with about 7 ps rise and fall time.*

increase results from a combination of the changing RF field and the strong space-charge forces, especially in the first few millimeters due to the non-relativistic beam energy. In a bunch with the mean position at $z = 20\,\mathrm{mm}$, the particles in the head of the bunch are longer exposed to the accelerating field and gain a higher energy than those in the tail. Moving closer to the cavity iris, the particles in the tail gain higher energies than the ones in the head and the momentum spread decreases. This process recurs in the full cell. For a phase of $\phi = 23°$ the particles in the tail are emitted later, but also at phases with higher momentum gain than the electrons in the head of the bunch.

At the entrance of the full cell the electrons in the tail of the bunch, which are accelerated stronger in the half cell and are decelerated less at the entrance of the full cell, have reached a higher momentum than the head particles, thus at about $z = 65\,\mathrm{mm}$ the momentum spread has reached its minimum. During the acceleration in the full cell a tiny compression of the bunch can be observed, due to the fact that the tail particle contain the higher momentum, but due to the small energy spread the reduction of the bunch length is negligible. For $z > 150\,\mathrm{mm}$ the energy spread increases again due to the fact that the head particles leave the full cell earlier and the tail

particles are exposed to a higher field. It is interesting to see that for a phase of 36° the bunch simulated including space charge forces shows a smaller energy spread than the one without at the exit of the gun cavity.

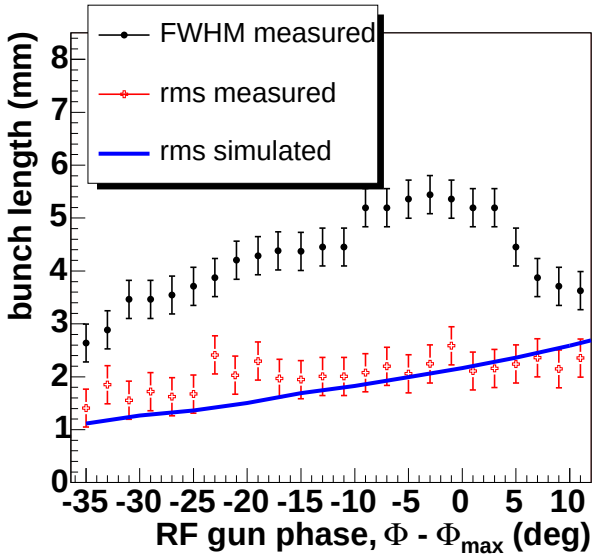

Figure 5.4: *Bunch length measurements as a function of the gun phase (gun prototype 3.2) and simulations at $z = 5\,m$ without accelerating field in the booster cavity. The phase is given with respect to the phase of maximum mean momentum gain. A laser pulse with a flat-top transverse laser distribution with an aperture diameter of 2 mm and a flat-top longitudinal distribution with a duration of about 20 ps (FWHM) and rise times of about 7 ps was used. The solenoid field was about 170 mT and the accelerating gradient at the cathode was about 55 MV/m.*

Figure 5.3 (b) shows the development of the bunch length (rms value) within the gun. For the phases $\phi = 23°$, 36°, 43° and 63° the bunch length is already rather stable before the bunch enters the full cell where the bunch length varies only slightly. For $\phi = 90°$ the energy spread is large and since the bunch is still not fully relativistic the particles in the bunch-tail with a lower energy fall behind and the bunch length increases. The simulation shows an increase of the rms bunch length with the emission phase. This was also observed in the measurements presented in figure 5.4. The measurement was performed at HIGH1.Scr2, the booster was turned off.

Figure 5.5 shows measurements (a) of the longitudinal phase space distribution of the electron bunch for different phases compared to simulations (b). This measurement was performed in the dispersive arm of the PITZ-1 setup

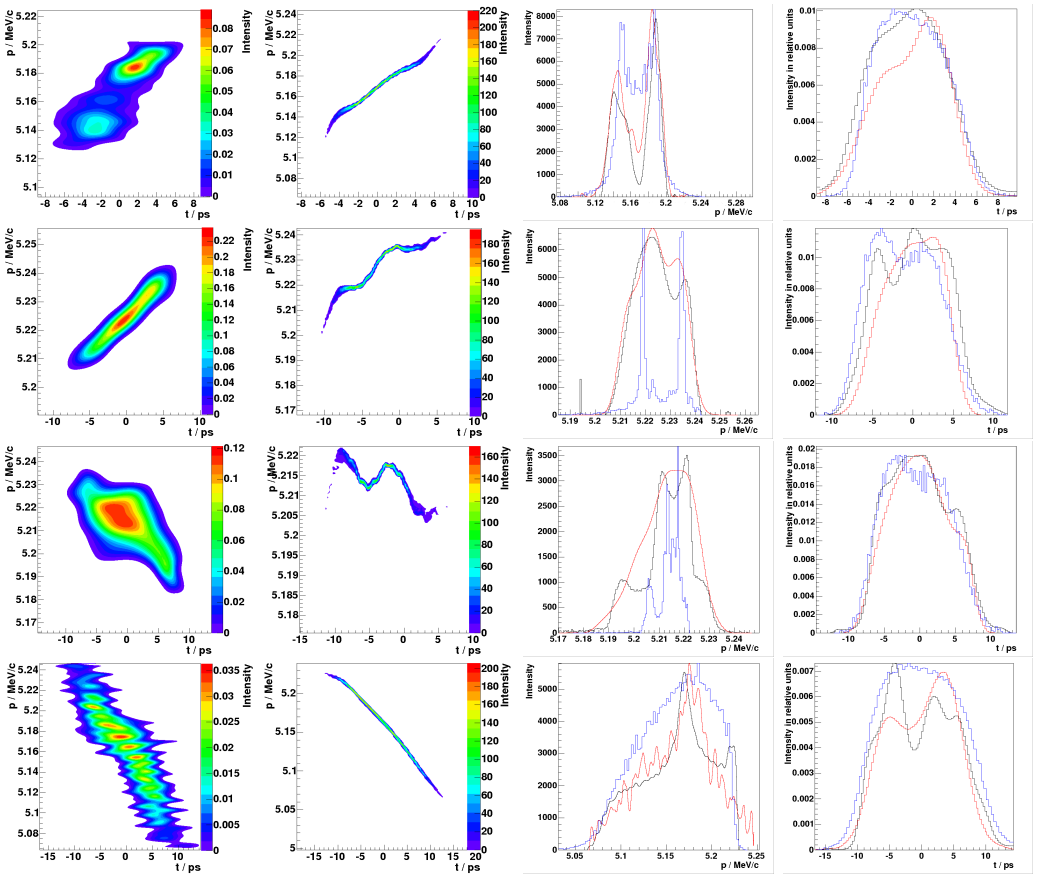

Figure 5.5: *Measurements (a) and simulations (b) of the longitudinal phase space distribution of the bunch and its projections (momentum (c) and longitudinal (d) distribution) for different RF launch phases (from top to bottom: 24°, 35°, 40° (phase of maximum momentum gain) and 49°). In (c) and (d) the projections of the measured longitudinal phase space distribution (red) were compared to the direct measurements (black) and the simulations (blue). Measurements were taken for a gradient of 45 MV/m at the cathode, about 30 pC bunch charge, flat-top longitudinal (FWHM ≈ 20 ps, rise time ≈ 7 ps) and transverse laser distribution (2 mm diameter).*

(see figure 2.2) using silica aerogel with $n = 1.05$ as Cherenkov radiator, for gun prototype 1, using a maximum field at the cathode of about 45 MV/m. The measurement on top was done for the phase of 24°, followed by 35°, 40° the phase of maximum mean momentum gain and the phase of 49°. The momentum distribution (c) measured on the YAG screen in the dispersive

arm (black) is compared to the projection of the measured longitudinal phase space distribution (red) and the simulations (blue). Also, the longitudinal distribution (d) measured directly, in the straight section (black) is compared to the projection of the measured longitudinal phase space distribution (red) and the simulations (blue).

The head of the bunch is located at $t < 0$, and for phases smaller than optimum phase (phase of maximum mean momentum gain) it contains the electrons of lowest momentum. For phases larger than optimum phase the electrons with highest momentum are located in the head. For optimum phase the highest momentum is expected in the center of the bunch, but the space-charge forces within the bunch increase the momentum of the head particle and decrease the momentum of those in the tail. In chapter 5.3 the influence of the space-charge force on the bunch is analysed in more detail.

The projections of the longitudinal phase space distribution of the electron bunch agree roughly in shape and width with the direct measured distributions (means: momentum measurement gain from the YAG screen and bunch length measurement in the straight section) and the simulations. The measured and simulated longitudinal phase space distributions show similar shapes and the orientation of the slopes are recognizable in all examples, but the measured longitudinal phase space distributions are much wider along the time and momentum axes than the simulated ones. This is commonly observed for all used operation conditions. The discrepancies are mainly caused by the limited resolution of the measurement system. The influence of the initial beam size ($R_{11}x_0 + R_{12}x'_0$ and $R_{51}x_0 + R_{52}x'_0$) to the longitudinal phase space measurement has been corrected by deconvolution. The response were determined from simulations. The beam size and divergence vary along the bunch, therefore every longitudinal slice should be corrected by the transverse position and divergence distribution of this slice, but the identicalness between measured and simulated slice is difficult to ensure and impossible for the direct measurement. The resulting distribution was too noisy to apply a further deconvolution, correcting for the influence of the optical transmission line and the streak camera. To estimate the impact of the resolution of the streak camera the simulated longitudinal phase space distribution (shown in figure 5.6 (b)) was convoluted with the resolution function of the streak camera [Ham04]. In figure 5.6 (c) the convoluted distribution is shown. It bears a better resemblance to the measured one (shown in figure 5.6 (a)), but there is still a discrepancy due to jitter (since 100 pulse trains containing 20 pulses have been added up to reach an adequate signal-to-noise ratio), noise, and the fact that for the correction of the effects in the dipole only simulated distributions were used. For the measurement of the temporal distribution (bunch duration), the resolution of the streak camera of 2 ps is sufficient, but

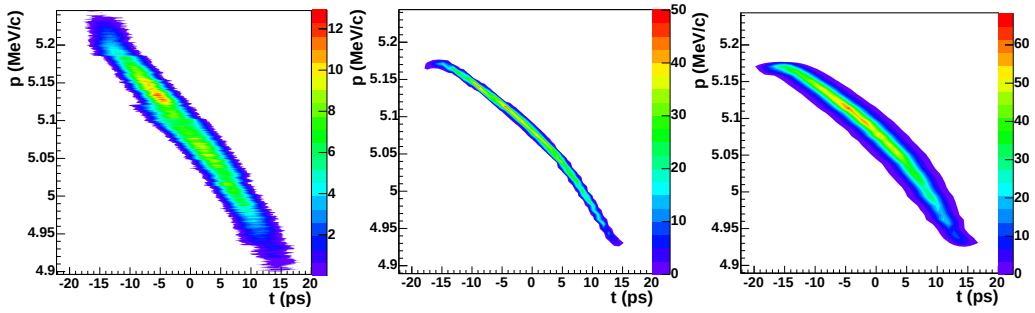

Figure 5.6: *Measured longitudinal phase space (a) and corresponding simulation (b) for a launch phase of 45° (the phase of maximum momentum gain is at 35°), flat-top laser distribution (duration: 20 ps, rise time 7 ps), a maximum gradient of about 45 MV/m at the cathode and 1 nC bunch charge. In graph (c) the simulation was convoluted with the resolution function of the streak camera (shown in figure 4.44 (b)).*

for measurements of the longitudinal phase space distribution a smearing of the distribution by 2 ps strongly impacts the measurement. Therefore, the measured values of longitudinal emittance exceed the simulated ones.

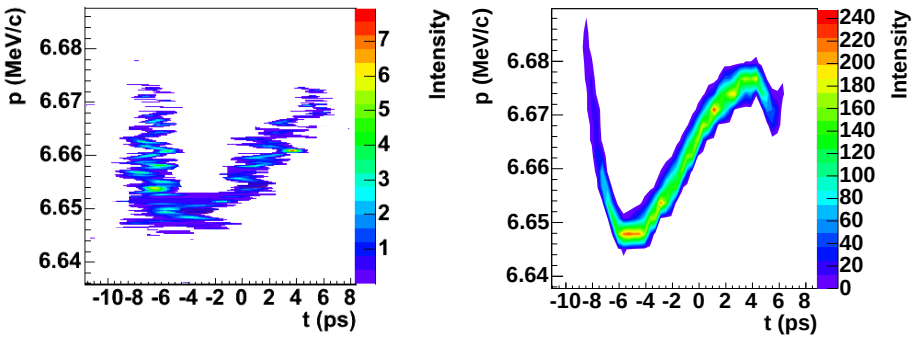

Figure 5.7: *Distribution of the bunch in the longitudinal phase space measured with gun 4.2, by the modified LEDA spectrometer(a) and corresponding simulation (b) for a phase of 36° (43° is the phase of maximum momentum gain), a gradient of about 60 MV/m at the cathode, Gaussian laser distribution of 2 ps FWHM and 1 nC bunch charge.*

Figure 5.7 shows a first measurement using the modified low energy dispersive arm combined with the 0.1 mm slit upstream the dipole magnet. The

longitudinal phase space distribution was measured for the phase of 36°, with 43° the phase of maximum momentum gain). A Gaussian laser distribution of 2 ps FWHM[1] and 1 nC bunch charge was used. A gradient of about 60 MV/m was applied at the cathode. The momentum spread $\Delta p_{rms\,/\,sim.} = 10.4\,\mathrm{keV/c}$ and the bunch duration $\Delta t_{FWHM\,/\,sim.} = 12.7\,\mathrm{ps}$ using the short Gaussian pulse is very small, comparable to the case of about 30 pC with a flat-top laser distribution of 20 ps FWHM (shown in figure 5.5). Using the modified spectrometer LEDA combined with the slit allows to resolve smaller structures compared to the results presented in figure 5.5, but the signal-to-noise ratio is very low. This small signal-to-noise ratio causes strong fluctuations when the deconvolution for the correction of the optical transmission line is applied. This shows that an improvement of the optical transmission line as discussed in chapter 4.4.3 is strongly required.

5.2 Influence of the booster launch phase

Figure 5.8 (a) shows the measurement of the mean momentum as a function of gun and booster phase, and in (b) the measured mean momentum as a function of the booster phase is compared to simulations for the gun phase with maximum energy gain downstream the gun cavity, which is labeled as 0°. In figure 5.9, as in figure 5.8, the rms momentum spread is shown in (a) as a function of gun and booster phase, and in (b) as a function of booster phase compared to simulations for a gun phase of maximum momentum gain.

The measurement was done at 1 nC beam charge and a flat-top transverse and longitudinal laser distribution. The booster phase of maximum mean momentum gain (labeled as 0°) and minimum momentum spread differs by about 5°. Simulation and measurement of the mean momentum agree within a large range of the booster phase. The measurement of the momentum spread shows a jump in the values at -13° and around 3°. Due to the strong increase of the momentum spread with the booster phase it was necessary to change the number of pulses during the measurement. For a large momentum spread, 10 electron bunches have been used to reach a sufficient signal to noise ratio, while for a small momentum spread a single pulse has been used in order to stay below the saturation of the camera.

Figure 5.10(a) shows the measurement of the mean momentum downstream the booster of a single bunch for different possible bunch positions within the range of a full bunch train. This means the bunch was shifted along the RF pulse. The first bunch of a train should not be placed before the

[1] A laser pulse duration of 2 ps FWHM can be reached by removing the pulse shaper in the new laser system, see section 2.2.1

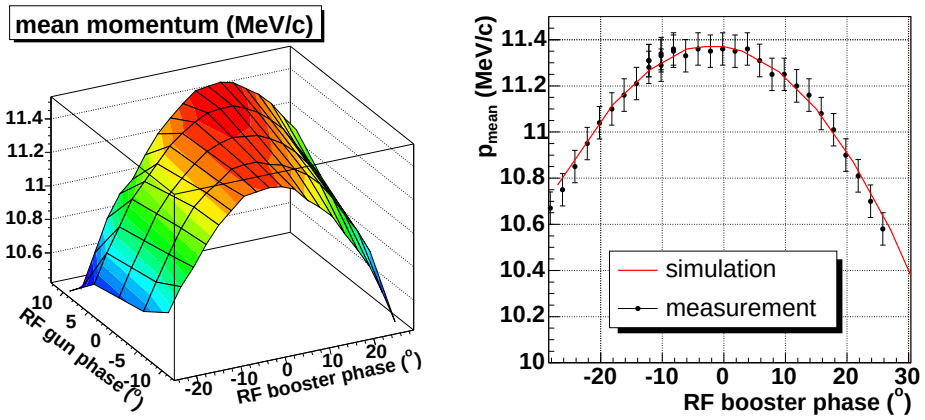

(a) (b)

Figure 5.8: *Mean momentum downstream the booster measured for different gun and booster phases(a) and for different booster phases at a gun phase with maximum energy gain downstream the gun cavity (b). The solid line in (b) presents the results from ASTRA simulations. Measurement was done with gun prototype 1 applying a gradient of about 40 MV/m at the cathode, for a flat-top longitudinal laser distribution with a duration of the bunch of about 20 ps and 7 ps rise time. The gradient of the nine-cell TESLA booster was 12.5 MV/m.*

position defined as 0, where the filling time is completed. From 0 to about 20 μs the mean momentum is rather stable, afterwards it starts slightly to decrease. The reason of the difference in the mean momentum of the bunches along the RF pulse is that there is no regulation of the RF power and phase along the pulse by a feedback system. This inhomogeneity in the RF power was the reasons for the jump in the momentum spread measurement of figure 5.9 discussed above. In figure 5.10(b) the measured distributions for $t = 17\,\mu$s and $t = 67\,\mu$s are displayed to get an idea about the blurring of the momentum distribution and change in the momentum spread.

Figure 5.11 shows measurements (at HIGH1.Scr2) and simulations of the bunch duration as a function of the booster phase. The measurement has been taken for a momentum of 6.3 MeV/c at the gun using the gun phase of maximum mean momentum gain and 15.5 MeV/c at the booster for the phase of maximum mean momentum gain, defined as 0° in figure 5.11. The temporal laser distribution with a flat-top laser shape had a duration of about 20 ps and rise and fall times of 7 ps and a transverse diameter of 1.8 mm. The measurement covers a large phase range (120°). The rms bunch duration stays almost constant over a large range around the phase with the maximum

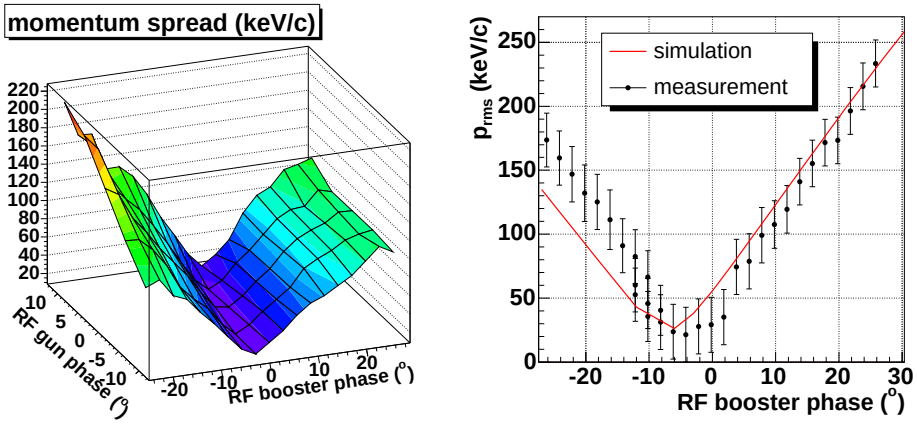

Figure 5.9: *Momentum spread downstream the booster measured for different gun and booster phases(a) and for different booster phases at a gun phase with maximum energy gain(b). The solid line in (b) presents the results from ASTRA simulations. Measurement was done with gun prototype 1 applying a gradient of about 40 MV/m at the cathode, for a flat-top longitudinal laser distribution with a duration of the bunch of 20 ps and 7 ps rise time. The gradient of the nine-cell TESLA booster was 12.5 MV/m.*

momentum gain ($\varphi = 0°$). For an off-crest phase, the bunch duration changes more strongly.

5.2.1 Velocity bunching

Figure 5.12 shows the development of the longitudinal parameters (mean energy, energy spread and bunch length) along the beamline up to the point of measurement (at $z = 5$ m). The booster cavity extends from about 2.3 to 3.6 m downstream the cathode. For a phase of -90° the momentum gain of the booster cavity is almost 0 MeV/c while the momentum spread becomes very large, since the first derivative of the field is maximal at about this phase, just opposite to the phase of maximum mean momentum gain. The facts that for a phase of - 90°, which is about zero crossing, the energy spread is large, the electrons in the tail have a larger energy than those in the head of the bunch and the bunch energy is still low, are the basis for the so-called velocity bunching (or ballistic bunching). Figure 5.13 shows the development of bunch length and longitudinal phase space distribution along the direction of motion for the phase of -90° up to the screen station for bunch length measurements, located 5 m downstream the cathode. Upstream the booster

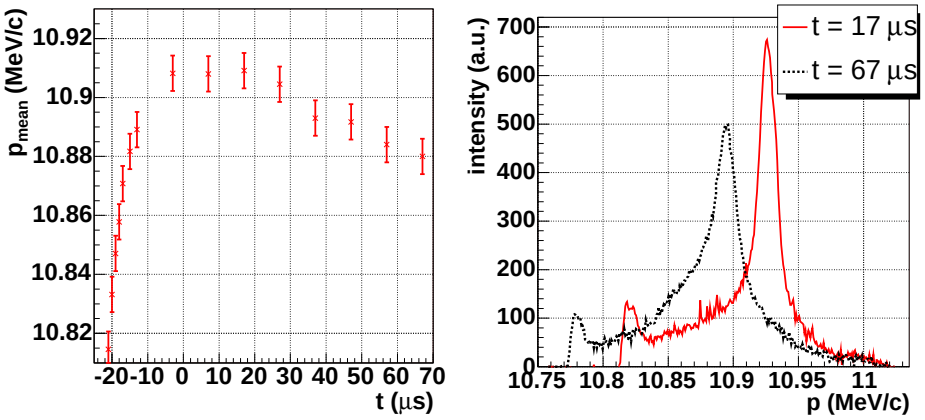

(a) (b)

Figure 5.10: *Mean momentum measurements downstream the booster of a single bunch for different laser emission times (a), this means different positions of the laser pulse within the RF pulse. Measured momentum distributions for laser pulses emitted at $t = 17\,\mu s$ and $t = 67\,\mu s$ (b). The Measurements were done under the same conditions as figure 5.9.*

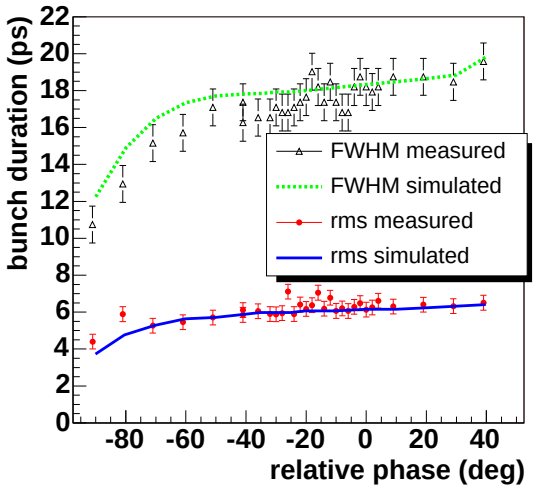

Figure 5.11: *Bunch duration measurements and simulations downstream the booster cavity as a function of the booster phase.*

the electrons in the head of the bunch have a slightly higher momentum than those in the tail and thus the bunch length increases slightly within the drift length from the gun to the booster cavity. For a phase of -90° the particles in the head are losing energy in the booster while the particle in the tail gain

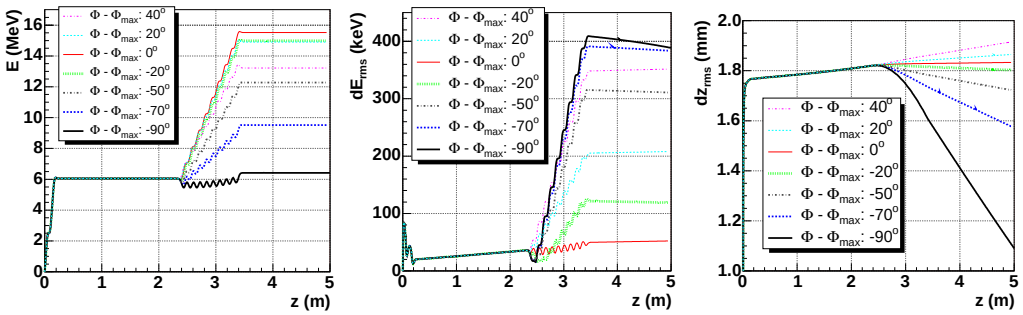

(a) (b) (c)

Figure 5.12: *Development of mean energy (a), energy spread (b) and bunch length (c) along the beamline for different booster phases. 0° is the phase of maximum mean momentum gain.*

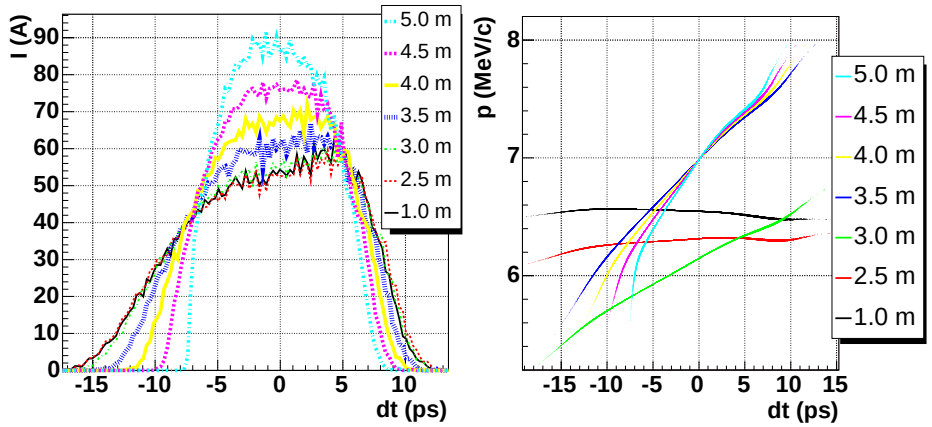

(a) (b)

Figure 5.13: *Simulations of the development of the longitudinal distribution (a) and the longitudinal phase space distribution (b) downstream the gun cavity up to the screen station for bunch length measurements for -90°. The head of the bunch is at t<0.*

energy. The resulting bunching is visible as a shearing of the longitudinal phase space distribution of the bunch. The screen station for longitudinal phase measurement (HIGH1.Scr2, $z = 5\,\mathrm{m}$) is situated at a position where the bunch still has not reached its full compression. Simulations show (figure 5.14 (a)) that a minimum bunch length is expected about 8.5 m downstream the gun (about 6 m downstream the entrance of the booster cavity). A high peak current of about 1 kA and a bunch duration of $\Delta t_{FWHM} \leq 1\,\mathrm{ps}$ are expected

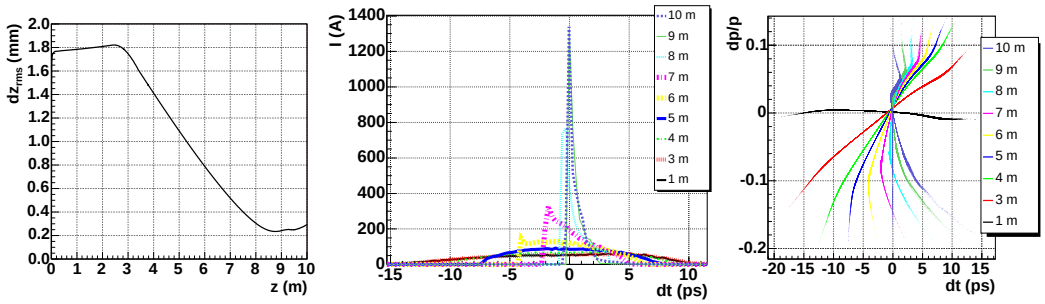

(a) (b) (c)

Figure 5.14: *Simulations of the development of the bunch length as a function of the distance to the cathode (a). Simulations of the longitudinal distribution (b) and the longitudinal phase space distribution (c) for different positions downstream the gun cavity for a booster phase of -90°. The head of the bunch is at t<0.*

from the simulation for the compressed bunch (figure 5.14 (b)). Since the bunch length for a certain momentum is very small, non-linearities in the initial longitudinal phase space distribution (figure 5.14 (c)) mainly define the reachable length of the entire bunch. These settings produce, along with the large energy spread, a degradation of the projected transverse emittance. In the PITZ2 setup, the RF deflector is planned to be situated about 8 m downstream the entrance of the booster cavity. At that position the velocity bunching is fully developed and the deflector is a proper device to measure this small bunch length.

The measurement of the bunch length as a function of the RF booster phase showed a very small change of the bunch length with the phase, since the used screen station (HIGH1.Scr2) is close to the booster cavity. This changes after a longer drift, since the strong change of the momentum spread with the RF booster phase (that has been shown in figure 5.9) causes a change in the bunch length and peak current during the drift. An extreme example has been discussed in detail. Generally the velocity bunching is an interesting method to increase the peak current without a bunch compressor, where coherent synchrotron radiation can cause instabilities. Furthermore could a high current, short electron bunch be interesting for methodical studies. Since this methode works at a strong off-crest phase its main disadvantage is the large transverse emittance.

5.3 Influence of the electron bunch charge

As seen in section 5.1, space charge forces have a major impact on the development of the longitudinal parameters. Thus the influence of the bunch charge to the longitudinal phase space distribution of the bunch is investigated in this section. Figure 5.15 shows the measured mean momentum

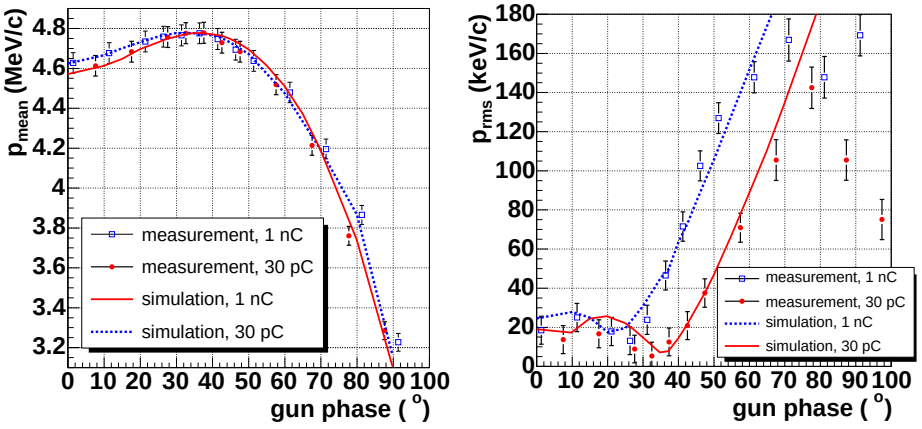

(a) (b)

Figure 5.15: *Measurements (gun prototyp 1) and simulations of the mean momentum (a) and the momentum spread (b) as a function of the gun phase for different charges (30 and 1000 pC) at a gradient of about 40 MV/m, with a flat-top longitudinal ($\Delta t_{FWHM} \approx 20 ps$, $t_{rise} \approx 7 ps$) and transverse laser distribution ($\sigma_{x/y} = 0.45$ mm).*

(a) and the momentum spread (b) as a function of the gun phase (for gun prototyp 1) compared to simulations for 0.03 and 1 nC bunch charge. The highest mean momentum of about 4.8 MeV/c was reached at a gun phase of about 35°, independent of the bunch charge. In the case of 1 nC, a minimum momentum spread of 13 keV/c was reached at a gun phase of about 25° (phase difference of 10° between phase of maximum momentum gain nd phase of minimum momentum spread), while for 30 pC, the minimum momentum spread of 5 keV/c was reached at about the phase of maximum momentum gain. An agreement of the phase of maximum mean momentum gain and minimum momentum spread is expected when space charge is not taken into account since the first derivative of the momentum ($\frac{\delta <p>}{\delta \phi}$) is minimal at that phase. For phases close to zero crossing the momentum spread decreases again due to the fact that the charge decreases. The curves of mean momentum are similar for both high and low charge regimes. There is a small difference in the mean momentum for the phase close to zero-crossing.

For the phase of maximum momentum gain the momentum spread is about 45 keV/c higher for the 1 nC case compared to 30 pC, and for higher phases the difference in momentum spread is about 60 keV/c. For high phases the measured values of the momentum spread are conspicuously smaller than the simulated ones. In the broad momentum distribution, different momenta are focused differently and thus parts of the distribution (at the high energetic and low energetic edge) were cut, which leads to an underestimation of the momentum spread.

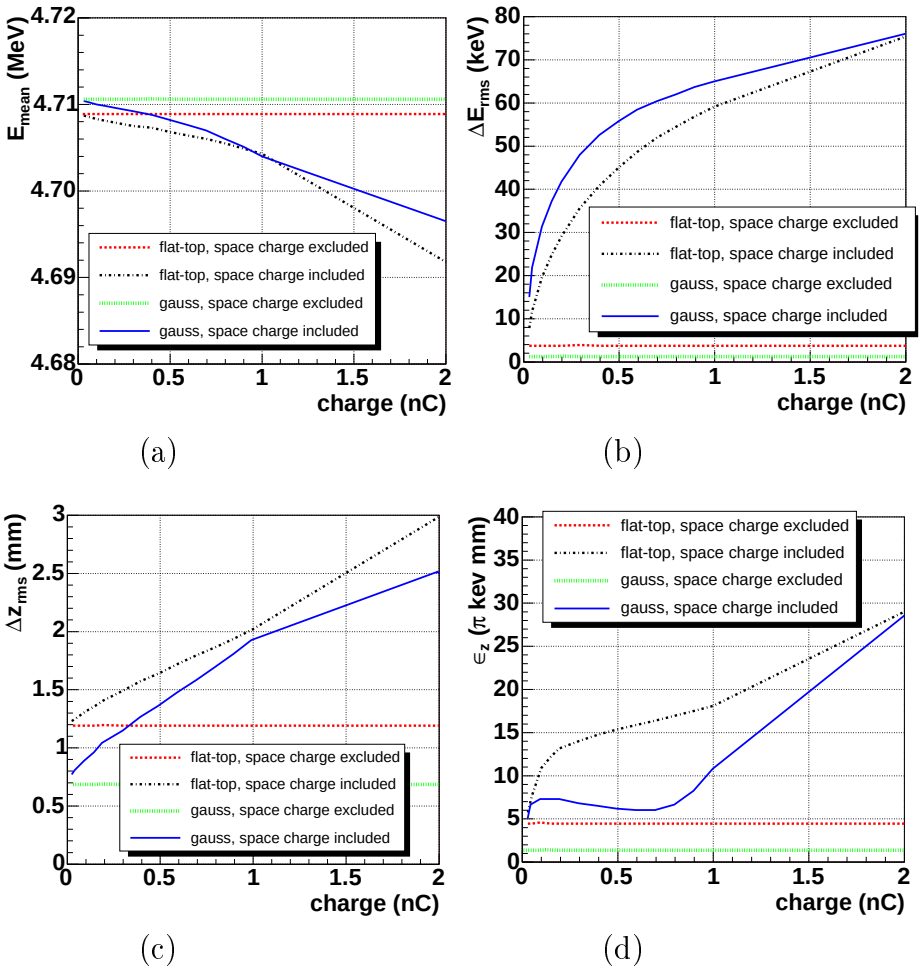

Figure 5.16: *Simulations of the mean bunch energy (a), the energy spread (b), the bunch length (c) and the longitudinal emittance (d) as a function of the bunch charge, for the phase of maximum mean momentum gain using the longitudinal laser distributions shown in figure 5.17.*

Figure 5.16 shows simulations of the longitudinal parameters (the mean

longitudinal bunch energy, the energy spread, the bunch length and the longitudinal emittance) downstream the gun as a function of the bunch charge for the gun phase of maximum momentum gain. For these simulations typical longitudinal laser distributions measured at PITZ (shown in figure 5.17) have been used. Taking the space-charge force into account for the simula-

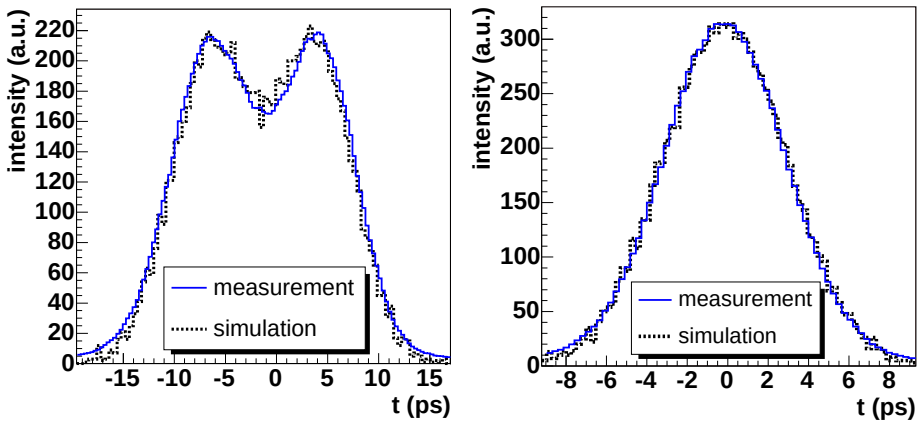

(a) (b)

Figure 5.17: *Typical longitudinal laser distributions measured at PITZ (a: flat-top (with a density modulation), b: Gaussian)*

tion, an increase of the charge causes an increase of the space-charge-forces and impacts the momentum spread in the first instance, but also the bunch length, and consequently the longitudinal emittance. The mean longitudinal momentum is decreased. The simulations have been done for the phase of maximum momentum gain, this means about the center of the electron bunch is emitted at the phase, where the maximum momentum can be reached. An increase of the bunch length and the momentum spread means necessarily that more particles are accelerated at phases further away from the phase of maximum momentum gain and thus the mean longitudinal momentum decreases.

In figure 5.18 the simulated dependence of the bunch length on the charge has been verified for a flat-top longitudinal and transverse laser distribution, using an accelerating gradient of about 40 MV/m at the cathode. The tendency of increasing bunch length with the charge is also in the measurement observable, but the resolution of the measurement is limited. The enlarged momentum spread and bunch length changes the acceleration conditions slightly and causes a small change of the mean longitudinal momentum (see figure 5.16) with the charge. It decreases by about 1‰ for 1 nC bunch

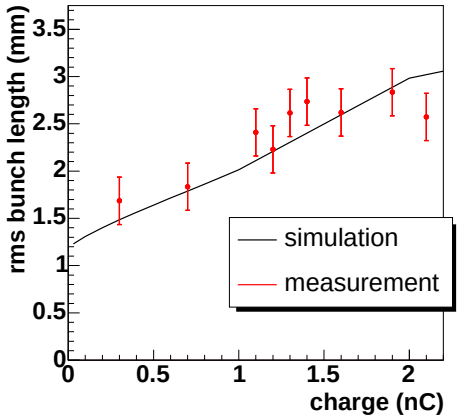

Figure 5.18: *Bunch length measured (with gun 3.1) for different charges compared to simulations, at a gradient of about 40 MV/m, for a flat-top longitudinal ($\Delta t_{FWHM} \approx 20ps$, $t_{rise} \approx 7ps$) and transverse flat-top laser distribution.*

charge due to the increased mean phase difference of the particles in the bunch to the phase of maximum momentum gain.

The longitudinal emittance ($\varepsilon_z = \sqrt{< l^2 >< \Delta E_z^2 > - < l\Delta E_z >^2}$) for a flat-top longitudinal laser distribution increases with the charge, especially for small charges there is a strong rise. The growth in longitudinal emittance is not as strong as the growth in momentum spread. For a charge of 1 nC the longitudinal emittance taking into account space-charge forces is about four times larger than not considering space-charge forces, while the momentum spread including space-charge forces in the simulations is 17 times larger than those without space-charge forces. For a Gaussian laser distribution, a minimum of the longitudinal emittance appears at about 0.65 nC. In practice, the solenoid current is optimized to focus the beam onto the screen in the dispersive arm. For all these simulations a solenoid current of 290 A has been used. For small charges the position of the focus is shifted towards the gun and the focusing leads to an increase of space-charge forces around that point.

Figure 5.19 shows the simulated longitudinal phase space distribution. For this simulation, space-charge forces have not been taken into account and the phase of maximum mean momentum gain has been used. The applied longitudinal laser distribution is comparable to the one shown in figure 5.17 (a). Under similar machine parameters settings the longitudinal phase space distribution of the electron bunch has been measured for different charges. The results are shown in figure 5.20. It shows the measured (a) and simulated (b) longitudinal phase space distributions of the bunches and

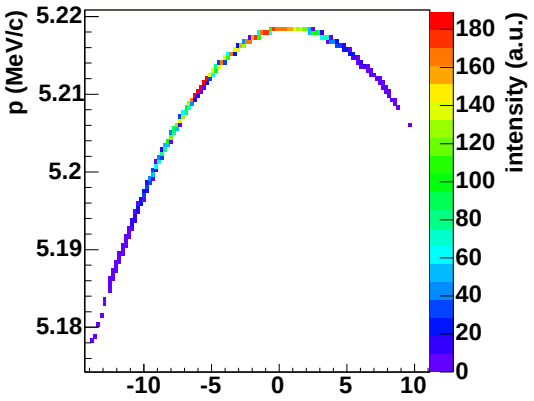

Figure 5.19: *Simulated longitudinal phase space distribution, not taking into account space-charge forces, for phase of maximum mean momentum gain with gradient of about 45 MV/m at the cathode and a longitudinal laser distribution comparable to figure 5.17 (a).*

their projections for different charges (38 pC, 100 pC, 200 pC, 500 pC, 1 nC), downstream the gun cavity. Applying a gradient of about 45 MV/m at the cathode a beam momentum of about 5.2 MeV/c was reached. In the longitudinal distribution determined from the projection of the longitudinal phase space distribution measured in the dispersive arm, for 1 nC, two minima can be found. These minima are caused by the assembling of different streak images and the deconvolution processes, which can cause modulations when the signal is noisy. Also the direct measurements of the temporal distribution show modulations caused by the deconvolution of the measured distribution with the resolution of the streak camera and the optical transmission line. The particles in the head of the bunch gain momentum and the ones in the tail lose momentum with increasing charge. For 38, 100 and 200 pC the momentum distribution 3.45 m downstream the photocathode shows two spikes and the distribution in the longitudinal phase space is non-monotonic. For higher charges the stronger space-charge forces of the particles in the higher energetic spike push the particles in front towards higher energies. It also has to be mentioned that for low charge more modulations are visible in the measurements than in the simulations, the source could be caused by the jitter of the beam, since several laser pulses have been accumulated for the measurement. This deformation of the longitudinal phase space distribution of the electron bunch (compared to the one not taking into account space-charge forces) does not only appear during the acceleration in the gun, but also in the drift space downstream the gun. Figure 5.21 shows the simulated

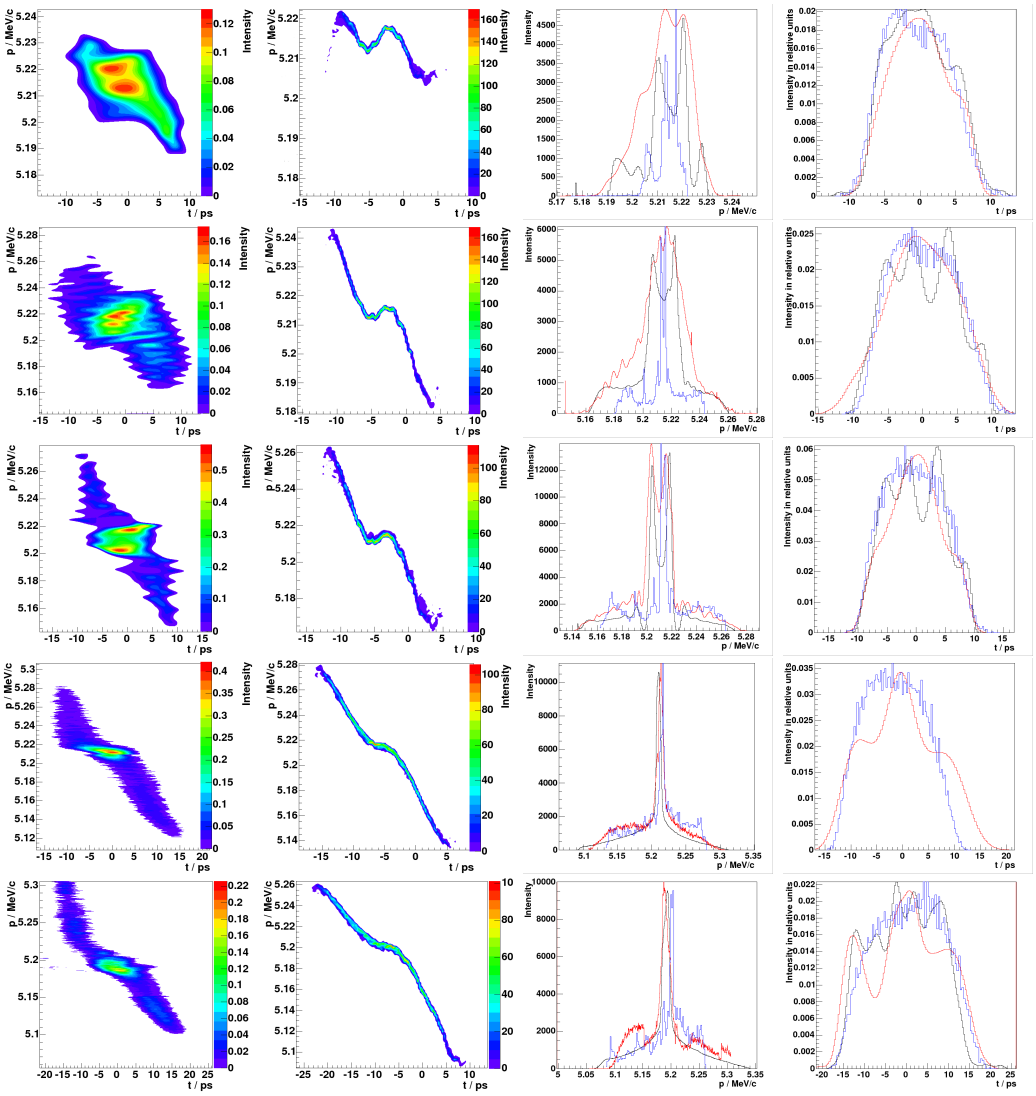

Figure 5.20: *Comparison of measurements (a) and simulations (b) of the longitudinal phase space distribution for different charges (from top to bottom: 38 pC, 0.1 nC, 0.2 nC, 0.5 nC, 1 nC) downstream the gun cavity for a flat-top temporal laser distribution ($\Delta t_{FWHM} = 20\,ps$, $t_{rise} = 7\,ps$) and a gradient of about 45 MV/m at the cathode. Also the simulated (blue) momentum (c) and temporal (d) distributions are compared to the direct measurements (black) and the projections of the measured longitudinal phase space distribution (red).*

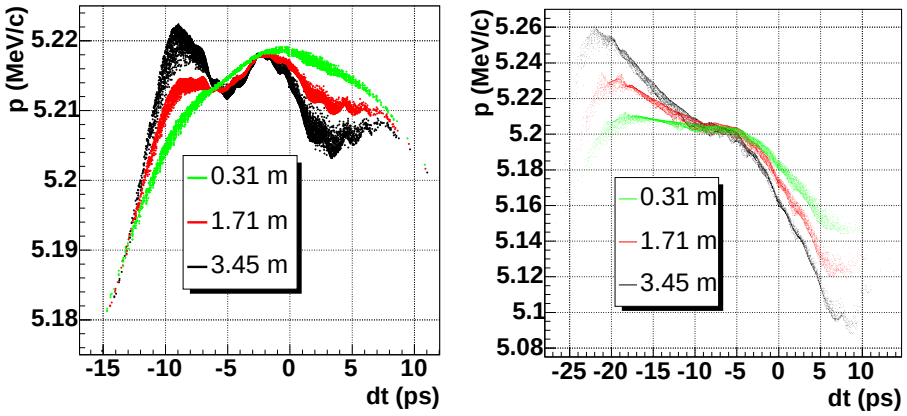

(a) (b)

Figure 5.21: *The simulated longitudinal phase space at 3 different longitudinal coordinates downstream the gun cavity for 38 pC (a) and 1 nC (b).*

longitudinal phase space distribution at three different longitudinal positions downstream the gun cavity for 38 pC (a) and 1 nC (b). For 38 pC the longitudinal phase space distribution 30 cm downstream the cathode is comparable to the phase space achieved from simulations not taking into account space-charge effects. Only along the following drift are the particles in the tail of the bunch slightly decelerated by the space charge forces and the electrons in the head of the bunch accelerated.

5.4 Influence of the longitudinal laser distribution

Figure 5.17 (a) showed a typical longitudinal laser distribution used up to 2007. It has rise and fall times of about 7 ps and a FWHM of 20 ps. The distribution shows a modulation on the flat-top. The influence of the longitudinal laser distribution on the longitudinal phase space distribution is analysed in this section.

5.4.1 Investigation of modulations in the longitudinal laser distribution

Figure 5.22 (a) shows four different initial laser longitudinal distributions, one without modulations (black) and three with differently distinctive mod-

ulations: ±40% (red), ±25% (green) and ±18% (blue). Figure 5.22 (b) shows

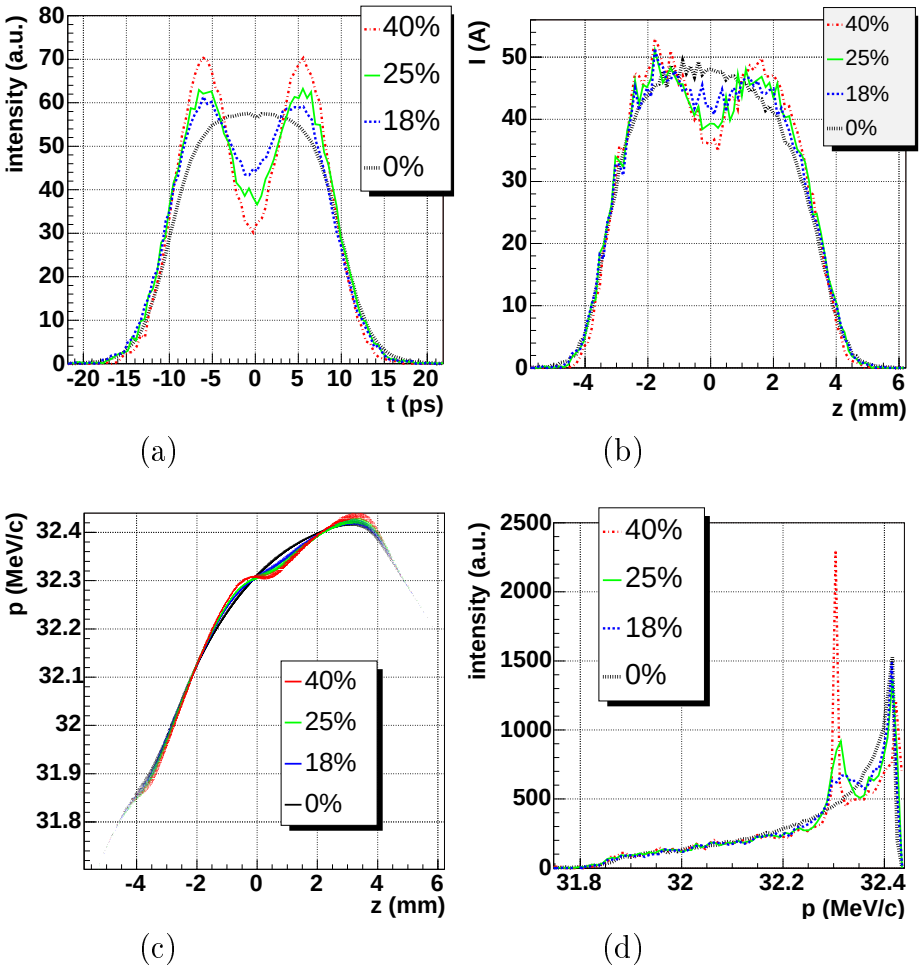

Figure 5.22: *Analysis of the influence of modulations in the longitudinal laser distribution (a) to the temporal current density (b), the longitudinal phase space distribution (c) and the momentum distribution (d) 8 m downstream the photocathode, for a charge of 1 nC, a maximum gradient of 60 MV/m at the cathode and 28.85 MV/m in the CDS booster cavity.*

the simulated resulting charge density distributions of the bunch. A conspicuous reduction of the current modulations compared to the modulations in the temporal laser distribution (by about a factor of 2) could be observed. This reduction of the modulations is observed directly after emission. The space-charge forces within the bunch directly after the emission are high, additionally the bunch induces a high positive mirror charge on the cathode, which smears out local density variations directly after the cathode. Figure

5.22 (c) presents the simulated longitudinal phase space distributions. The largest discrepancy in the mean slice momentum between longitudinal phase space produced by the modulated and modulation-free longitudinal laser distributions appears at the positions where the slope of the distribution differs at most. 5.22 (d) presents the resulting momentum distributions. Notably the momentum distribution for the laser distribution with ±40% modulation contains an additional spike compared to that one without modulations at $p = 32.3\,\mathrm{MeV/c}$. This spike arises from a constant momentum around the slice correlated with the local minimum in the temporal cathode laser distribution, due to the fact that after the emission the mirror-charge forces combined with space-charge forces strongly affect the beam. Since the space-charge forces act strongest at the maximum charge density, the longitudinal bunch distribution becomes more homogenous than the longitudinal laser distribution. The change in the charge density also causes a change in the mirror charge, which acts against the acceleration. Therefore the strongest changes in the momentum between modulated and non-modulated longitudinal laser distribution appear at the position of the strongest difference in slope. Thus, an initially modulated density distribution of the laser beam leads to energy modulations and a distortion of the longitudinal phase space distribution.

Also for the results presented in figure 5.20, the initial longitudinal laser distribution contained some modulations, especially for low charges where two maxima in the momentum distribution appeared. With the increase of the electron beam charge they are shifting towards each other due to the space-charge forces.

The momentum distributions generated by different longitudinal laser distributions have been analysed. Figure 5.23 (a) shows the used longitudinal laser distributions and (b) the resulting momentum measurements. The measurements have been done for the phase of maximum mean momentum gain and a bunch charge of 1 nC. Generally one can see that the momentum width becomes larger as the bunch becomes shorter. From this it follows that the momentum spread for the phase of maximum mean momentum gain is mainly determined by space-charge forces. The measurements show two maxima in the momentum distributions for all longitudinal laser distributions that contain two maxima.

Figure 5.24 shows for one example the comparison of the measurement with the simulation in order to understand the shape of the momentum distribution. The structure of the simulated and measured momentum distribution agree in general, but some differences are noticeable. The differences are presumably caused by the imprecision of the measurement of the temporal laser distribution by the streak camera (see section 4.5) and the influence of

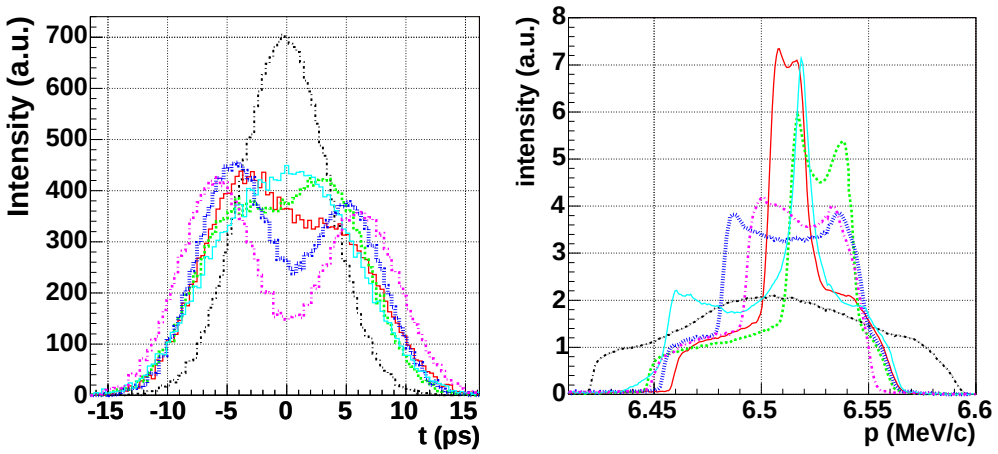

(a) (b)

Figure 5.23: *Different longitudinal laser distributions (a) have been applied for momentum measurements (b) for the phase of maximum mean momentum gain and for a bunch charge of 1 nC.*

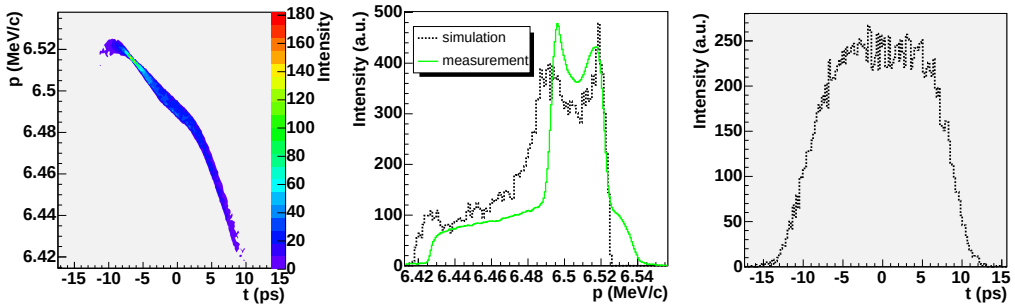

(a) (b) (c)

Figure 5.24: *The simulated longitudinal phase space distribution (a) and its projections (b/c) for the green longitudinal laser distribution shown in figure 5.23 (a). The measured momentum distribution (b) (green) was compared to the simulated one (black).*

the initial beam size and divergence to the momentum measurement. The same is true also for the other distributions. The longitudinal distributions do not show the initial modulations, but in the longitudinal phase space distribution the two parts have a different slope, as shown already in figure 5.21 (b) directly downstream the gun.

5.4.2 A Gaussian longitudinal laser distribution

Figure 5.25 show measurements of the longitudinal phase space distribution

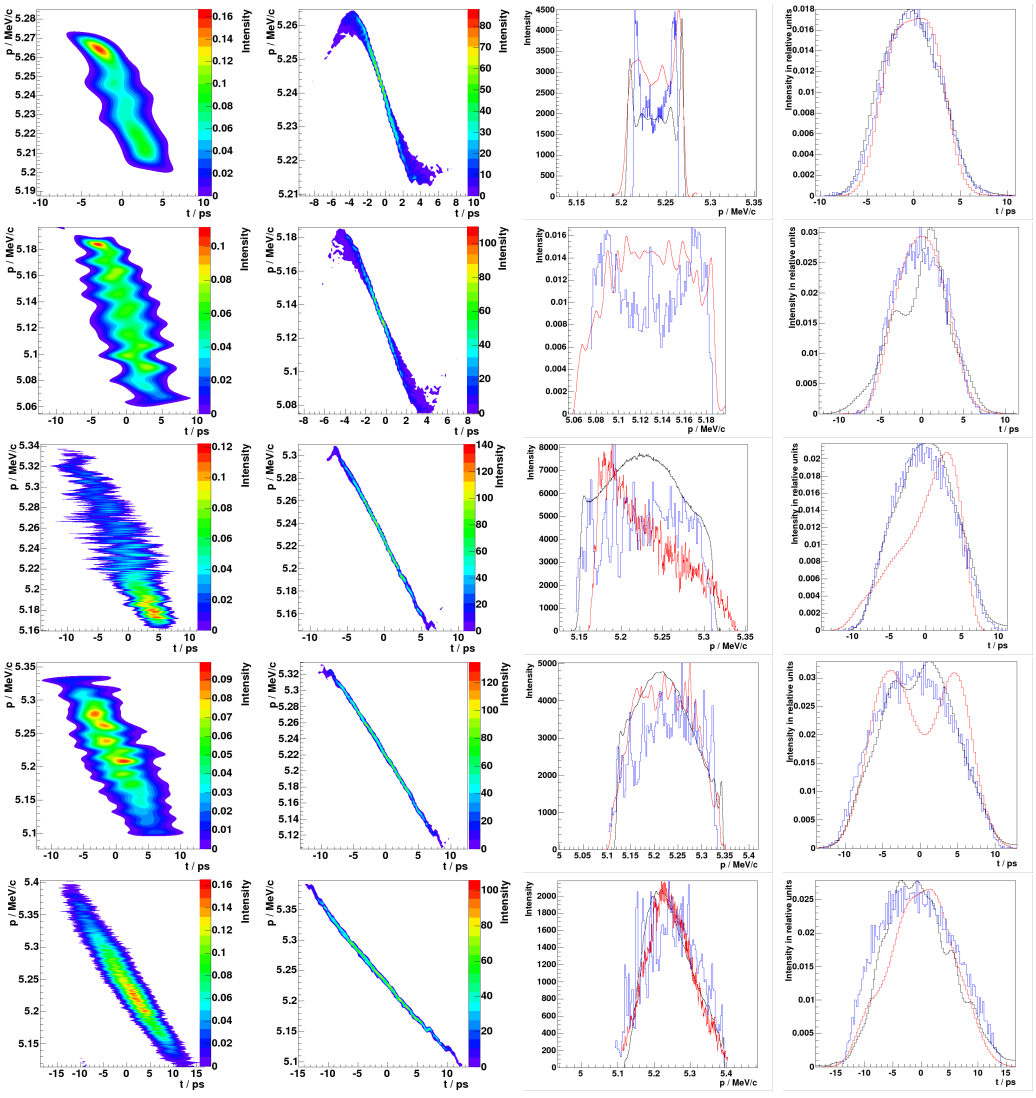

Figure 5.25: *Comparison of measured (a) and simulated (b) longitudinal phase space for different charges (from top to bottom: 38 pC, 100 pC, 200 pC, 500 pC, 1 nC). Also the simulated (blue) momentum (c) and longitudinal (d) distribution were compared to the direct measurements (black) and the projections of the longitudinal phase space distribution (red). Unlike the results presented in figure 5.20, the initial longitudinal laser distribution is Gaussian with a FWHM of 10 ps.*

of the bunch measured under the same conditions as the results presented in figure 5.20 (RF launch phase of maximum mean momentum gain, 1 nC bunch charge), but for Gaussian longitudinal laser distribution (FWHM = 10 ps). For this case the error resulting from the assembling of different streak images was reduced, and there are less modulations due to the deconvolution in the longitudinal distribution visible as in figure 5.20. For a longitudinal Gaussian distribution the influence of the space-charge force is higher than for flat-top, because the charge density in the bunch is higher, due to the shorter laser pulse length in the inhomogeneous charge distribution. This leads to a strong increase of the momentum spread and an almost linear longitudinal phase space distribution of the bunch, with high energetic electrons in the head and lower energetic electrons in the tail.

5.5 Influence of the gun gradient

In the PITZ-1 setup a gradient of about 40 MV/m at the cathode has been reached using a 5 MW klystron. One of the goals of the second stage of PITZ is the application of a higher gradient in the gun cavity, in order to reduce the space-charge forces. A 10 MW multi-beam klystron had been used to reach this higher gradient. Figure 5.26 shows the simulated and measured mean momentum for the phase of maximum mean momentum gain for different gradients. In the measurement (done with gun 4.2) the RF power (P) in the gun was determined instead of the gradient. The accelerating gradient at the cathode (E) was calculated by: $E = K\sqrt{P}$. The common scale factor K was determined, by the least square fit method to the simulation, with $K = 2.25 \cdot 10^4 \frac{V}{m\sqrt{W}}$. Statistical errors of the momentum and the power measurement are included in the graph, but the error bars are too small to be visible. The measurements at a gradient of about 61 MV/m have been taken on different days. The results differ by about 0.3 MeV/c. A possible reason for this discrepancy is that the gun was not fully conditioned during the measurement and the quality of the cavity improved during the operation. When the gun is fully conditioned the measurement should be repeated. It also has to be taken into account that especially at the limit of the klystron (at high power) subharmonics can occur which influence the power measurement.

In order to estimate the influence of the gradient on the space charge forces, the reciprocal of the square of the simulated Lorentz factor downstream the gun cavity (1 m downstream the photocathode, for a field balance of FB = 1.05) is drawn as a function of the gradient in figure 5.27(a). For an increasing gradient from 40 to 60 MV/m a decrease of the space-charge force

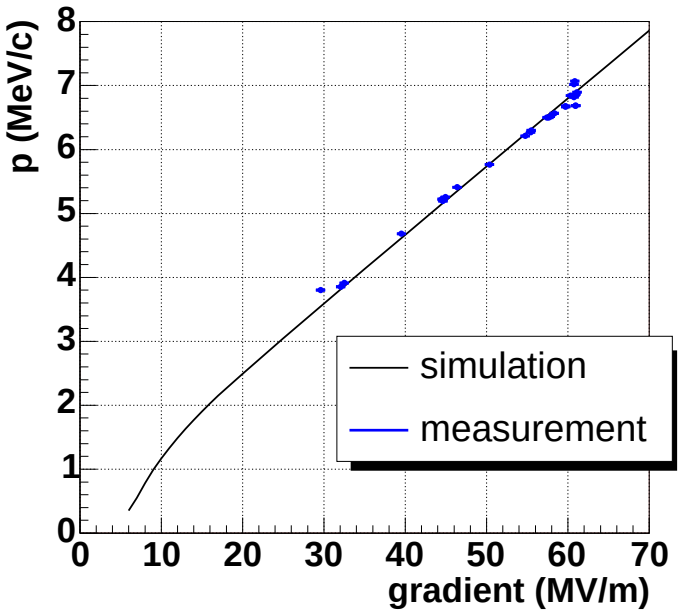

Figure 5.26: *Simulated and measured maximum mean momentum as a function of the maximum field at the cathode. For the simulations a field balance (FB) of 1.05 was assumed.*

($F_{SC} \sim \frac{1}{\gamma^2}$) by about a factor of two can be observed.

Figure 5.27(b) shows the phase of maximum mean momentum gain and minimum momentum spread. Excluding space-charge force (scf) from the simulation the phase of maximum mean momentum gain and minimum momentum spread agree. When space-charge forces are considered in the simulation a difference between phase of maximum mean momentum gain and minimum momentum spread (green line) occurs. With increasing gradient the phase of minimum momentum converges towards the the phase of maximum mean momentum gain. For 40 MV/m the difference is $7.6 \pm 0.2\,^\circ$ and $3.6 \pm 0.1\,^\circ$ for 60 MV/m. The maximum mean momentum in figure 5.26 scales linear with the gradients starting from about 20 MV/m. The non-linearity for gradients smaller than about 20 MV/m can be explained using figure 5.27: In the simulations of the mean momentum as a function of the gradient the mean momentum was always determined for the phase of maximum mean momentum gain. With decreasing accelerating gradient at the cathode also the phase of maximum momentum gain decreases. At about 20 MV/m the phase of maximum momentum gain becomes 0°. For smaller launch phases the emitted particles are forced backward into the cathode directly after emission, therefore the phase of maximum mean momentum gain is 0° for all

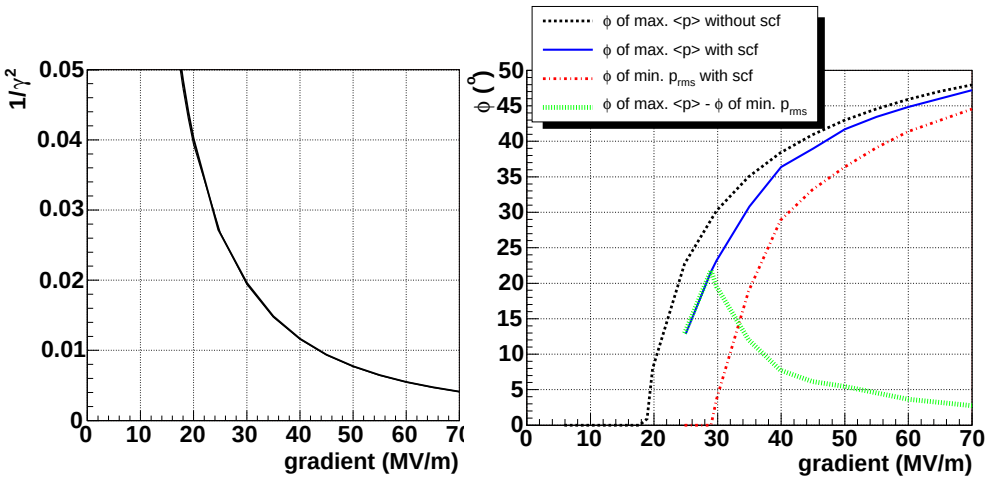

(a) (b)

Figure 5.27: *Simulated reciprocal of the square of the Lorentz factor reached at the exit of the gun cavity (a) and the phase of maximum mean momentum gain (neglecting and taking into account space-charge forces (scf)) and minimum momentum spread (b) are displayed as a function of the maximum field at the cathode. The green curve presents the difference of the phases for maximum mean momentum and minimum momentum spread. For the simulations a field balance (FB) of 1.05, a transverse rms laser size of 0.58 mm and temporal flat-top laser distribution with a FWHM of 20 ps and 2 ps rise and fall time were assumed.*

gradients smaller than about 20 MV/m. The smaller the gradient gets the later the particles arrive at the end of the cavity half cell and thus the higher are the energy losses. Therefore the linear relationship between gradient and the maximum momentum is not fulfilled at very low gradient. For a phase 0° a part of the emitted electrons is lost directly at the cathode. This is thus not a useful operating phase.

Figure 5.28 shows the simulated longitudinal phase space distribution (c) and its projections (momentum distribution (a) and longitudinal bunch distribution(b)) for the RF phase with the highest energy gain, about half a meter downstream the cathode for a gradient of 40 and 60 MV/m at the cathode, using a longitudinal drive laser distribution of 20 ps FWHM with different rise times. Applying a higher gradient decreases the momentum spread and the bunch length. For example, for a laser pulse rise time of 7 ps the momentum spread decreased from 28.1 to 22.1 keV/c, and the rms bunch length from 2.29 to 1.94 mm. The smaller bunch length at 60 MV/m results

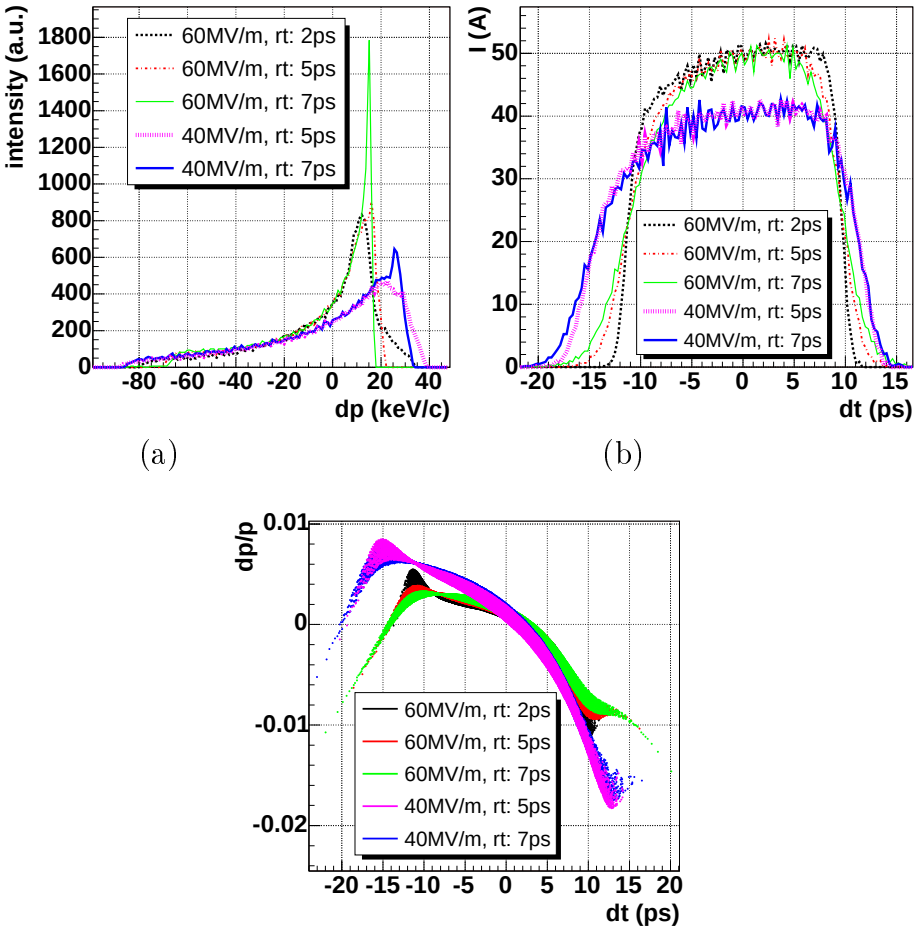

Figure 5.28: *Simulated momentum distribution (a), temporal distribution of the charge density (b) and longitudinal phase space distribution (c) for 40 and 60 MV/m at the cathode, using a longitudinal drive laser distribution of 20 ps FWHM with different rise times (rt).*

in a 20% higher peak current. The longitudinal rise and fall time of the laser pulse can be retrieved in the longitudinal distribution of the bunch. For larger longitudinal laser pulse rise times the mono-energetic peak at higher energies is stronger developed.

5.5.1 Influence of the gradient dependent charge emission

As discussed in section 2.2.2 the quantum efficiency of the cathode and thus the emitted charge depend on the gradient at the cathode. Therefore the charge extraction increases within the phase range 0 90°. The typical length of the laser pulse used at PITZ is 20 ps FWHM, for a frequency of 1.3 GHz this corresponds to a phase difference of 9.4° and thus the increase of the quantum efficiency has to be taken into account for the simulation of the longitudinal distribution. To be able to determine the factors from equation 2.1 the charge as a function of phase has to be known.

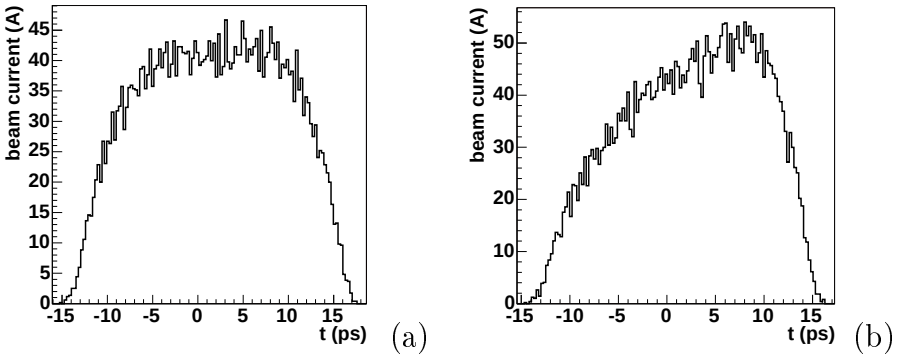

Figure 5.29: *Simulated longitudinal distribution, for the pure photo-effect (a) and for an emission assuming the increase of the charge with the gradient (b). In both cases the total charge is 1 nC.*

Figure 5.29 shows the simulated longitudinal distribution, for the phase of maximum mean momentum gain, for the pure photo-effect (a) and for an emission taking into account the increase of the charge with the gradient. In both cases the total charge is 1 nC. The charge distribution shown in figure 5.32 had been used for the case of phase dependent charge emission. The initial laser distribution has a length of 18 ps (FWHM). The increase of the bunch length for both cases results from spaces charge force and mirror image forces. The inhomogeneous charge distribution leads to an increase of space charge forces in the tail of the bunch.

5.6 Influence of the booster gradient

The difference of the momentum up- and downstream the booster cavity was measured as a function of the power in the booster cavity. Figure 5.30 shows

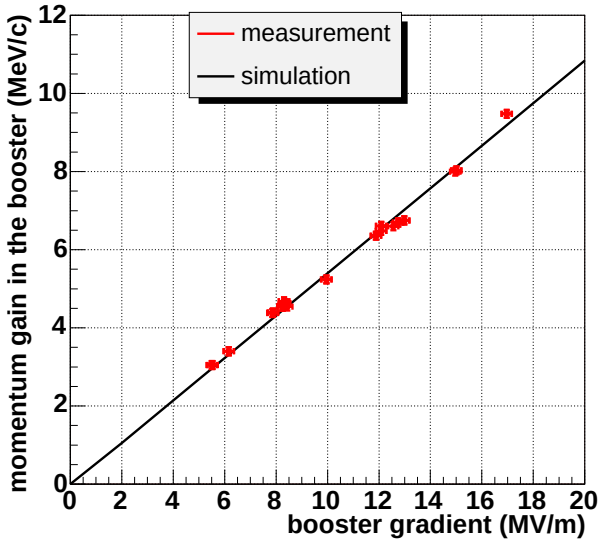

Figure 5.30: *Simulated and measured maximum mean momentum gain in the booster as a function of the booster gradient.*

the maximum momentum gain in the booster as a function of the accelerating gradient. The measured power (P) of the booster was converted to the accelerating gradient by $E = K\frac{V}{m\sqrt{W}}\sqrt{P}$, with $K = 1.086{\cdot}10^4$, achieved from fitting the measurement to the simulation results. The TESLA booster is operable up to a power of 3 MW. This corresponds to a gradient of 18.8 MV/m and a maximum possible momentum gain of 10.2 MeV/c for the booster phase with maximum momentum gain. Since during the measurements in 2007 the gun (gun 3.2) was operated at maximum possible gradient (which corresponds to a momentum of about 6.5 MeV/c) and the used dipole spectrometer was limited to a maximum measurable momentum of 16 MeV/c, the booster had been used with a maximum momentum gain of 9.5 MeV/c.

5.7 Influence of the transverse laser diameter

According to the longitudinal laser distribution the transverse distribution has to be optimized in order to reach an electron beam with small transverse distribution. Its influence to the longitudinal parameters will be discussed in this section. Figure 5.31 shows the measured and simulated bunch length for a Gaussian longitudinal laser distribution with a duration of 2 ps FWHM, a peak field of the main solenoid of 210 mT and a bunch charge of 1 nC. Both measured and simulated bunch length increase with decreasing trans-

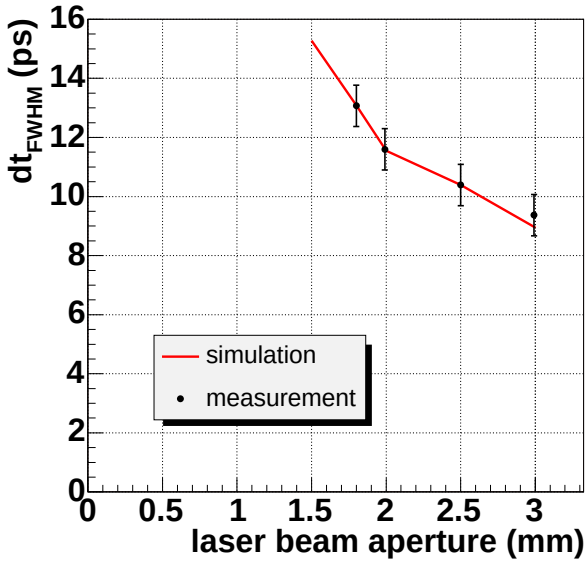

Figure 5.31: *Influence of the transverse laser beam size on the bunch length for a Gaussian laser pulse of 2 ps FWHM, a peak field of the main solenoid of 210 mT and a bunch charge of 1 nC.*

verse laser beam size, due to the increase of the charge density and thus the space-charge forces. This increase in the bunch length with decreasing transverse laser beam size results in a decrease of the peak current and reduces thus the transverse space-charge forces. This emphasizes the correlation of the transverse and longitudinal properties of the bunch in the space-charge dominated energy regime.

5.8 Momentum measurements for gun 3.2

The charge, mean momentum and momentum spread downstream the gun are parameters, which are measured regularly as a function of the emission phase. For gun 3.2 (see Appendix B) an irregularity has been observed during the measurement period in 2007.

Two examples of charge, mean momentum and momentum spread measurements as a function of the launch phase are shown in the figures 5.32 and 5.33. The measurements shown in figure 5.32 were taken in the beginning of the run period 2007 and the ones in figure 5.33 at the end. Since in the measurement only the relative phase is determined, the measured phase is adjusted to the simulated one by using the charge distribution. The momentum measurements as a function of phase were compared to the simulation.

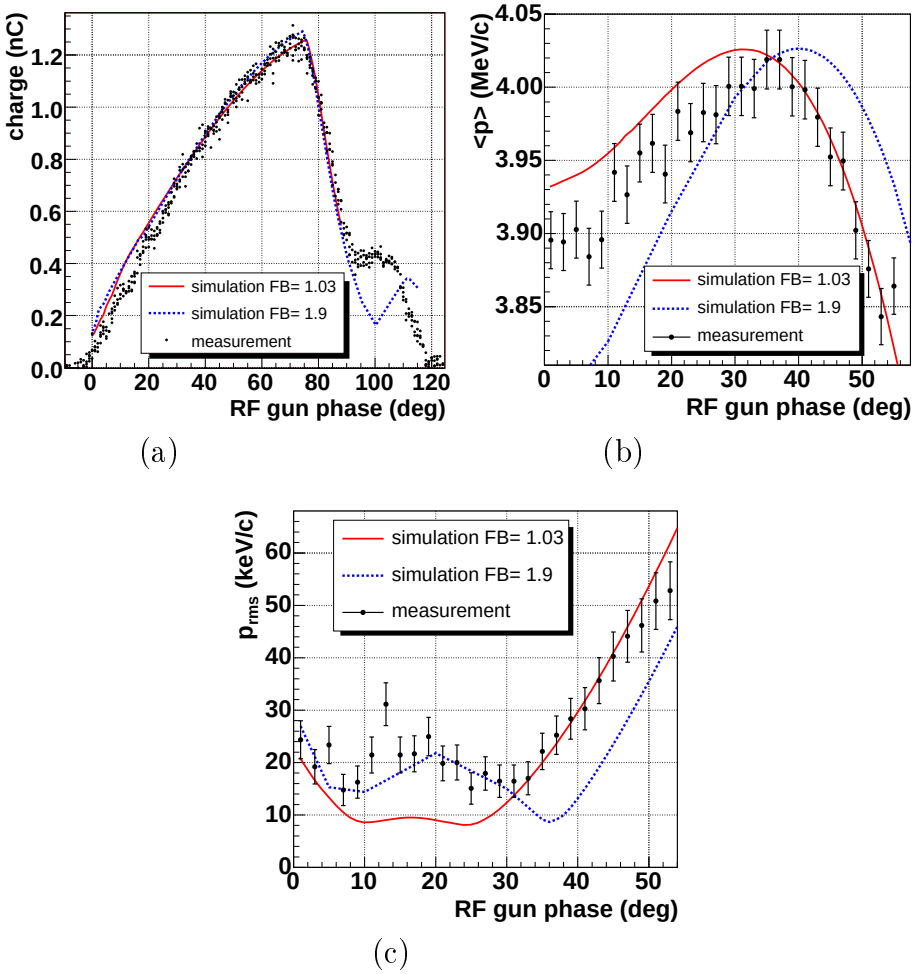

Figure 5.32: *An example for the measured and simulated charge (a), mean momentum (b) and momentum spread (c) as a function of the launch phase for gun 3.2 in the beginning of the run period (5th of June 2007).*

During the tuning of gun 3.2 the field balance was determined to be 1.03. While the first measurements fit well to the simulations for this field balance, this was not the case for later measurements. In the end of the run period the momentum measurements agree better to a simulation assuming a field balance of $FB = 1.9$. Such a strong change of the field balance is rather improbable. After the run period the field balance of the gun was remeasured and determined at 1.09 [Rim08]. The reason for the difference is not understood. A possible source could be some peculiarities of the field distribution, most probably within the cathode region of the gun cavity, that change the beam dynamics but not the field balance. For this gun a fabrication error in

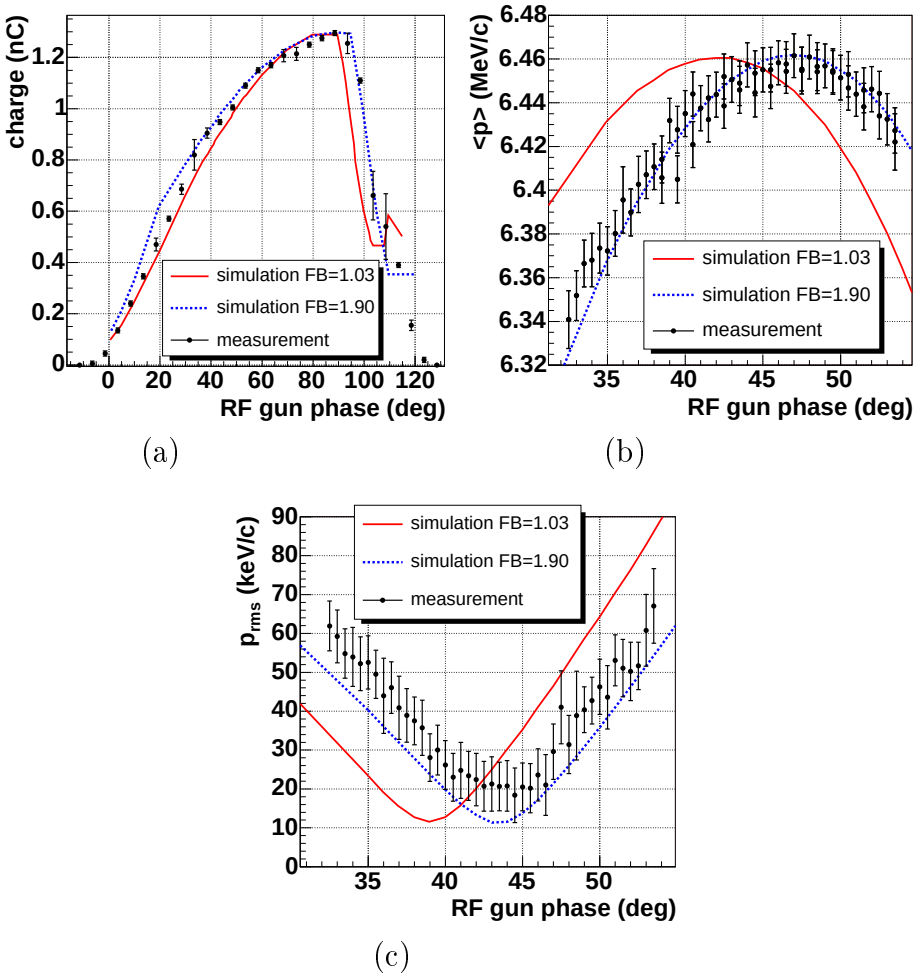

Figure 5.33: *An example for the measured and simulated charge (a), mean momentum (b) and momentum spread (c) as a function of the launch phase for gun 3.2 in the end of the run period 2007 (17th of August 2007).*

the area around the cathode plug was found, it was thought to be corrected, but it caused damages to the cathode surface [Rim07].

5.9 Summary of the measurements and simulations of the longitudinal phase space distribution of the bunch

The longitudinal properties of the electron bunches emitted by the laser driven RF electron source used at PITZ have been analysed in dependency of the major accelerator parameters like the launch phase, the strength of the accelerating field, the bunch charge and the cathode laser properties. The electrons emitted by the laser driven RF electron source achieve an energy of some MeV. The higher the reached beam energy becomes the smaller is the influence of space-charge forces and mirror charge forces, which results in a convergence of the phase of maximum momentum gain and the phase of minimum momentum spread. To reduce the influence of space-charge forces on the beam measurements also low charge bunches have been generated, but even for bunch charges of only about 40 pC a significant influence of the space-charge force could be determined by observing the electron bunch distribution in the longitudinal phase space downstream the electron source. Especially longitudinal modulations of the laser pulse distribution transform into sharp peaks in the momentum distribution due to non-linearities in the longitudinal phase space distribution, while the modulations in the longitudinal distribution of the bunch are strongly reduced compared to the laser pulse, due to mirror charge forces. Beside the longitudinal laser properties also the transverse laser beam size influences the longitudinal bunch distribution. A decrease of the laser beam size at constant charge causes an increase of the charge density and thus an increase of longitudinal space-charge forces, and an increase in bunch length can be observed. The electron bunch length depends mainly on the momentum spread of the bunch: depending on the slope (chirp) of the longitudinal phase space distribution of the electron bunch a large energy spread can increase or decrease the length of the electron bunch.

Chapter 6

Summary and outlook

For the first time the complete longitudinal phase space distribution of the electron bunches generated at the laser driven RF gun at PITZ was measured directly. The system for the measurement of the longitudinal phase space, the momentum and the temporal distribution of the electron bunch was designed for an accelerating gradient of 40 MV/m [Lip04]. Its subcomponents were analysed to understand sources of systematic uncertainties. The increase to higher energies due to the usage of higher accelerating gradients at the cathode in the gun cavity (60 MV/m) leads to an increase of the emission angle of the Cherenkov radiator used for bunch length measurements. In order to avoid losses the angle was reduced by decreasing the refractive index of the Cherenkov radiator. An extension of the facility demanded a widening of the distance of the pole shoes of the existing dipole spectrometer magnet. These improvements have been discussed and first measurements with the upgraded systems were presented. The extension of the facility by an additional accelerating cavity required the design of further longitudinal diagnostic systems for the analysis at higher momenta (up to 40 MeV/c). A system for bunch length measurements downstream the second accelerating cavity has been developed. Measurements using the system have been presented. The design of two high-energy spectrometers with different characteristics and the corresponding dispersive sections has been discussed. They are both configured to reach a high resolution in momentum and longitudinal phase space measurements. The existing optical system used for bunch and longitudinal phase space measurements has been analysed to determine its transverse and temporal resolution. Due to the limitation in resolution by the transmission line and the streak camera (Hamamatsu streak C5680), the measured values of longitudinal emittance are in general noticeably higher than the simulated values. Some approaches to replace the refractive optics by mirror lenses are presented [Ros08]. If an optical system consisting of

reflective optics would be realized the number of photons reaching the streak camera could be increased and single shot measurements could be done by a streak camera with a higher resolution. High resolution measurements of the longitudinal phase space distribution are expected in the PITZ-2 setup for an operation of the second high energetic dispersive arm together with a deflecting cavity. With this system detailed analysis of the slice energy spread, which is expect to be extremely small, will be possible.

Measurements of the longitudinal beam properties of the RF photoinjector for different machine parameters, like RF launch phase, charge, gradient and laser distribution were performed and compared to simulations. In the frame of the resolution of the measurement system a good agreement between measurement and siulations could be achieved. This means in general the longitudinal phase space distribution fulfils the expectations. A significant influence of the space charge force to the electron bunch distribution in the longitudinal phase space could be observed even for bunch charges as low as 40 pC in agreement with theoretical expectations and numerical simulation results. The shape of the longitudinal phase space distribution is strongly changing during the drift of the bunch at beam energies of a few MeV. In this energy range the development of the electron bunch length mainly depends on the energy spread of the bunch. A transformation of longitudinal modulations of the laser into momentum modulations has been observed experimentally and in simulations. The longitudinal modulations of the laser distribution cause non-linearities in the electron bunch distribution in the longitudinal phase space, these modulations are also preserved during acceleration towards higher energies and can cause major problems during the compression. These non-linearities in the distribution cause non-linear space charge forces. Thus a major request to the laser system used at FLASH and the XFEL is the homogeneity of the distribution. This means there are still detailed analysis of correlations between small modulations in the temporal laser distribution and the longitudinal phase space distribution of the bunch required in order to define the maximum acceptable depth of modulations for the XFEL. This requires a high-resolution diagnostics. A correlation of the transverse laser beam size and the longitudinal bunch properties could be observed in measurements and simulations caused by the coupling of longitudinal and transverse beam properties.

Appendix A

Different setups of the PITZ facility

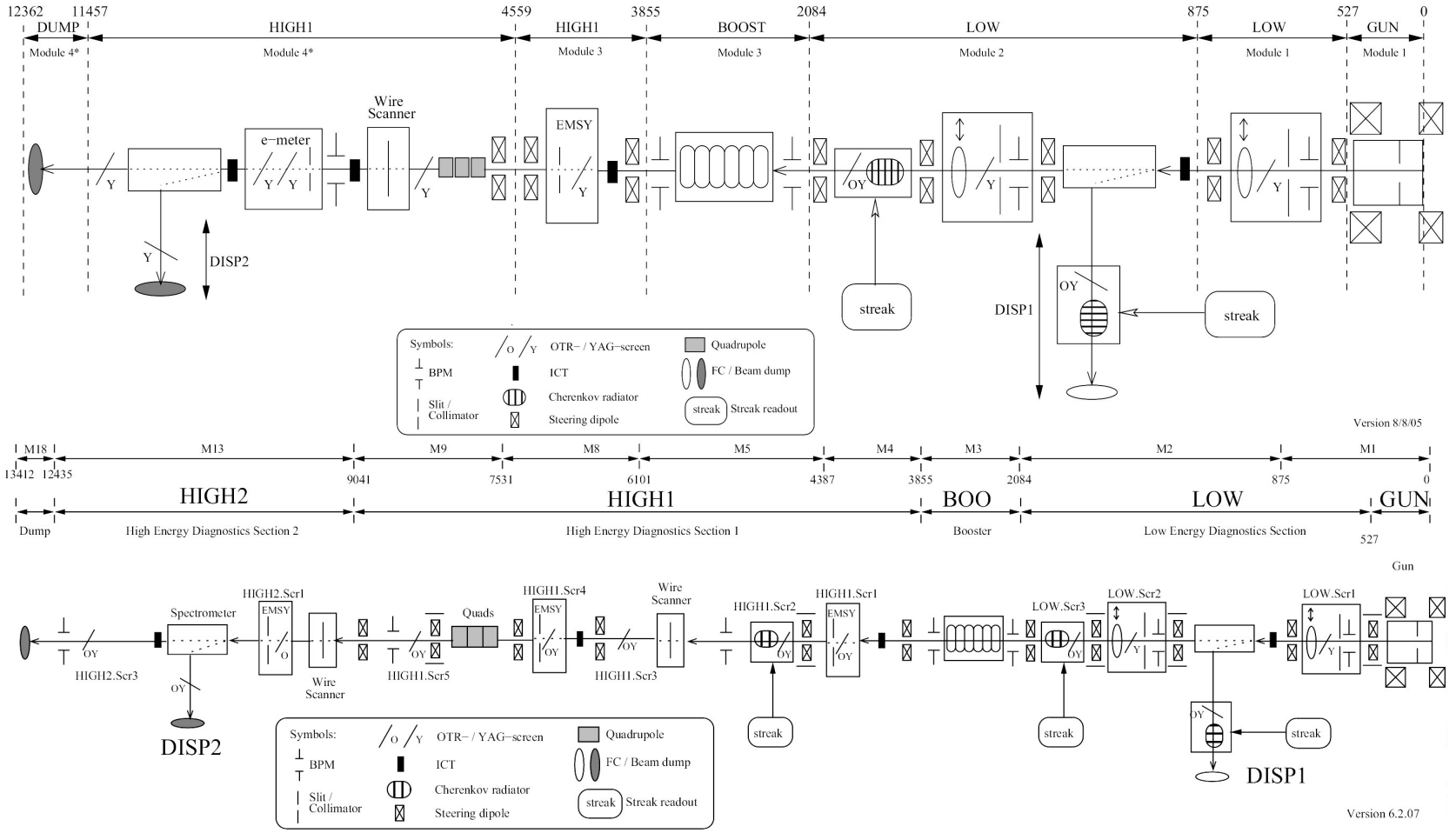

Figure A.1: *The PITZ 1.5 setup (top) displays the status of the facility starting from 2005 to 2006. In 2006 the PITZ 1.6 setup (bottom) was realized and used upto the end of 2007.*

Appendix B

Guns conditioned and characterized at PITZ

The measurements presented in chapter 5 were done with different RF guns at PITZ. Table B.1 gives an overview.

gun prototype	temporal period	maximum gradient (MV/m)	FB	comment
1	2004 / 2005	≈ 55	1.05	characterized at ≈ 43 MV/m broken during the conditioning
2	2002 / 2003	≈ 40	1.22	installed at FLASH in 2004
3.1	2006	≈ 43	1.08	spare gun for FLASH
3.2	2007	≈ 55	1.03	identical in construction to 3.1 higher dark current [PITZ08]
4.1	not yet used	-	1.08	improved cooling system
4.2	2007 - ..	≈ 60	1.05	identical in construction to 4.1
BESSY gun	2006	≈ 53		high power conditioning, av. power: 47 kW [Mar06]

Table B.1: *Overview of the guns conditioned and characterized at PITZ. The field balances (FBs) shown in the table were determined during the tuning process [Opp07].*

Appendix C

Diagnostics overview

C.1 Laser diagnostics

In order understand the relation between electron beam and laser beam, the laser pulses are analyzed or are planned to be analyzed by the devices listed in table C.1. The table also gives references.

property to be measured	device	comment	literature
transverse laser distribution and position	virtual cathode	CCD camera (+Ce:YAG plate)	[Hae07]
	quadrant diode	position sensitive photodiode	[Iva07] [Hae07]
longitudinal laser distribution	streak camera	photons converted to electrons, which are deflected by a RF field	section 4.5
	optical sampling system	based on cross-correlation	under development at MBI
laser energy	photomultiplier + energy meter	energy meter only used for calibration	[Hae07]

Table C.1: *Overview of laser diagnostics at PITZ. The virtual cathode and the quadrant diode have the same optical path length as to the photocathode. The optical sampling system is still under commisioning*

C.2 Electron beam diagnostics

Table C.2 shows a summary of current and future diagnostics at PITZ, the purpose of each and a reference where more details can be found. It should be pointed out that some components mentioned in the table are under design, but still not included in the PITZ setup, like the phase space tomography module or the RF deflector.

There are also kicker magnets foreseen to analyze single pulses within a train. They will be in combination with the phase space tomography module, the RF deflector or the dispersive arm.

Most of the diagnostics presented in the table are based on screens. Screen always means a combination of a YAG or OTR screen with corresponding optics and a CCD camera (see 2.2.6). Since the maximum expected beam momentum at PITZ is about 30 to 40 MeV/c and the screens used in the beamline have thicknesses of some 100 μm up to a few mm, the electron beam is disturbed by the screen. Therefore most of the diagnostics are destructive for PITZ. ICTs and BPMs are non-destructive diagnostics, also the wire scanner is almost non-destructive.

beam property	device	basic physical principle	literature
charge	ICT (integrating current transformer)	electromagnetic induction	[ber07]
	Faraday cup	charge deposition, current flow measurement	
transverse beam position size and shape	screen	fluorescence / optical transition radiation	section 4.2.2
	BPM (beam postion monitor)	four electro-magnetic pick-ups	
	wire scanner	scattered electron hits tube, shower detected by scintillation counters	[Cast05]
transverse phase space and projected emittance	slit mask + screen	beam size analysis about 1-2 m behind a slit	[Mil06]
	tomography module (screens + quadrupole)	rotating the phase space ellipse observe beam on different screens	[Aso07]
momentum	dipole magnet + screen	Lorentz force is momentum dependent	section 4.1.1
bunch length	radiator + streak camera	transformation of electron beam into light pulse	section 4.1.2
	RF deflecting cavity	time dependent transverse deflection	section 3.2.4
longitudinal phase space	dipole + radiator + streak camera	momentum measurement combined with bunch length measurement method	section 4.3
	RF deflector + dipole magnet + screen		section 4.3.3
transverse slice emittance	RF deflector + tomography module	convert temporal into transverse distribution, quadrupole scan	
	dipole magnet + slit + quadrupole + screen	run booster off-crest, cut momentum slice, quadrupole scan	[Kho06] [Iva07]
	quadrupole + aerogel + streak camera	quadrupole scan imaged onto a streak camera	[Gie99] [Spe08]

Table C.2: *Overview of existing and foreseen electron beam diagnostics methods at PITZ.*

Bibliography

[APS08] *APS Webpage*: http://www.aps.anl.gov (status: 2008/15/02)

[Aso07] G. Asova et al., *"Design Considerations for Phase Space Tomography Diagnostics at the PITZ Facility"*, Proc. of DIPAC 2007, Venice, Mestre, Italy

[Bae03] J. Bähr, D. Lipka, H. Lüdecke, *"Optical transmission line for streak camera measurements at PITZ"*, Proc. of DIPAC 2003, Mainz, Germany

[Bae07] J. Bähr, J. Rönsch, H. Lüdecke, *"Optical system for measuring the electron bunch length and longitudinal phase space at PITZ: Extention and methodical investigations*, Proc. of DIPAC 2007, Venice, Mestre, Italy

[ber07] , *Bergoz Webpage*: http://www.bergoz.com/products/ICT/ICT.html (status: 2007/14/11)

[BD93] K.P. Birch, M.J. Downs, *"An updated Edlen equation for the refractive index of air"*, Metrologia (1993), Bd 30: S. 155-162

[BD94] K.P. Birch, M.J. Downs, *"Correction to the updated Edlen equation for the refractive index of air"*,
Metrologia (1994), Bd 31: S. 315-316

[Bol05] A. Bolzmann, *"Investigation of the Longitudinal Charge Distribution of Electron Bunches at VUV-FEL Using the Transverse Deflecting Cavity LOLA"* Diploma Thesis 2005, Department of Physics of the Bayerische Julius-Maximilians Universität Würzburg

[Bor] M.D. Borland, *"A High-Brightness Thermionic Microwave Electron Gun"*, Thesis(Ph.D.)-Stanford University, 1991

[Bos07] M. Boscoloa et al., *"Generation of a Multipulse Comb Beam and a Relative Twin Pulse FEL"* Proc. of PAC07, Albuquerque, New Mexico, USA

[Bro92] Karl L. Brown„ *"A First- and Second-Order Matrix Therory for the Design of Beam Transport Systems and Charge Particle Spectrometers"*, Adv. Part. Phys., 1:71-134,1968.

[BR98] K.L.Brown and F. Rothacker, *"Third-Order TRANSPORT with MAD Input - A Computer Program for Designing Charged Particle Beam Transport Systems"*, SLAC-R-530 Fermilab-Pub-98-310, October 1998

[Car89] B.E. Carlsten, *"New Photoelectric Injector Design for the Los Alamos XUV FEL Accelerator"*, NIM A285, 313-319, 1989

[Casa05] S. Casalbuoni et. al., *"Numerical studies on the electro-optica sampling of relativistic electron bunches"*, Proc. PAC 2005, 3070-3072, Knoxville, Tennessee

[Cast05] P. Castro et al., , *"Wire Scanners in the Undulatorsection of the VUV-FEL at DESY"*, Proc. of Dipac 2005, 205-207, Lyon, France

[CERN94] E. Chevally et al., NIM A340, 146, 1994

[Che85] P. Chen et al., *"Acceleration of Electrons by the Interaction of a Bunched Electron Beam with a Plasma"*, Phys. Rev. Lett. 54, 693 - 696 (1985)

[Cia08] A. Cianchi et. al., *"High brightness electron beam emittance evolution measurements in an rf photoinjector"*, PHYSICAL REVIEW SPECIAL TOPICS - ACCELERATORS AND BEAMS 11, 032801 (2008)

[Cho07] S. Choroba, *"Design and Status of the XFEL RF System"*, PAC 2007 Albuquerque, New Mexico

[Del08] Hossein Delsim-Hashemi, *"Infrared Single Shot Diagnostics for the Longitudinal Profile of the Electron Bunches at FLASH"*, Dissertation, Hamburg University, Hamburg 2008

[Dow07] D. H. Dowell et. al., *"Commissioning Results of the LCLS Injector"*, Proc. of FEL 2007, Novosibirsk, Russia

[Dow] D. H. Dowell private communication

[ELBE08] *ELBE Webpage*: http://www.fzd.de/db/Cms?pNid=234 (status: 2008/12/08)

[Edl66] B. Edlén, *"The refractive index of air"*, Metrologia (1966), Bd 2: S. 71-80

[FEL08] *Webpage*: http://sbfel3.ucsb.edu/www/vl_fel.html (status: 2008/05/10)

[Fer01/1] M. Ferrario et al., *"Conceptual Design of the XFEL Photoinjector"*, TESLA-FEL Reports 2001-03, 2001

[Fer01/2] M. Ferrario, *"Low emittance photoinjector"*, NIM A 472 (2001) 303-308

[FLASH08] FLASH-Web-page: (status: 2008/24/11): http://flash.desy.de/

[Flo] Klaus Flöttmann, *ASTRA manual* http://www.desy.de/∼mpyflo/

[Fra86] J.S. Fraser et al. NIM A250,71-76,1986

[Fro05] L. Fröhlich, *"Bunch Length Measurements Using a Martin Puplett Interferometer at the VUV-FEL"*, Diploma Thesis, Hamurg University, 2005

[FS99] K.Floettmann, F.Stephan, *"Proposal for the BMBF "RF Photoinjectors as Sources for Electron Bunches of Extremely Short Length and Small Emittance"*, 1999

[Gie99] S.M. Gierman, *"Streak camera enhanced quadrupole scan technique"*, Los Angeles 1999, The physics of high brightness beams 511-526

[Gin46] V.L. Ginzburg and I.M. Frank, Sov. Phys. JETP 16 (1946), 15.

[Gra98] W. S. Graves, E. D. Johnson, and S. Ulc, , *"A High Resolution Electron Beam Profile Monitor and its Applications"*, AIP Conf. Proc. – December 10, 1998 – Volume 451, pp. 206-213, The eighth beam instrumentation workshop

[Gru99] F. Grüner et. al., *"Design considerations for table-top, laser-based VUV and X-ray free electron lasers"*, Applied Physics B-Lasers & Optics. 86(3):431-435, 2007 Feb.

[Hae07] M. Hänel et al., *"Photocathode Laser Pulse Diagnostics at PITZ"*, Proc. of FEL 2007, Novosibisk, Russia

[Haj07] R. Hajima, *"Development of a photocathode DC gun at JAEA-ERL"*, Asian Particle Accelerator Conference 2007, India

[Ham04] Hamamatsu, *"Universal Streak Camera C5680 Series (2004)"*

[Ham08] private comunicattion

[Her05] C. Hernandez-Garcia et al., *"A High Average Current DC GaAs Photocathode Gun for ERLs and FELs,"*, Proc. of PAC2005, Knoxville, Tennessee, USA

[Hon00] K. Honkavaara, *"Considerations of streak camera measurements for Photoinjector Test Facility (PITZ) in DESY Zeuthen"*, note, July 2000

[Iva07] Y. Ivanisenko et al., *"Photo injector cathode laser beam intensity and pointing position diagnostics and influence on electron beam emittance measurements"*, Proc. of DIPAC 2007, Venice, Mestre, Italy

[Jel58] J. V. Jelly, , *"Cherenkov Radiation and its Applications (1958)*, Pergamon Press

[Kho06] S. Khodyachykh et al., *"Design of Multipupose Dispersive Section at PITZ"*, Proc. of FEL 2006, Berlin, Germany

[Kim04] K.-J. Kim et al., *"Towards Advanced Electron Beam Brightness Enhancement and Conditioning"*, ANL/APS/LS-305, February 2004

[Kno99] J. Knobloch, *"Field Emission and Thermal Breakdown in Superconducting Niobium Cavities for Accelerators"*, IEEE Transactions on Applied Superconductivity 9 (2), 1016 (1999)

[Kor07] S. Korepanov et. al., *"An RF Deflector for the Longitudinal and Transverse Beam Phase Space Analysis at PITZ"*, Proc. of DIPAC 2007, Venice, Mestre, Italy

[KS80] Kondratenko, E.L.Saldin, Part. Acc. 10,207(1980)

[LB03] J. W. Lewellen and C. A. Braub, *"RF Photoelectric injectors using needle cathodes"*, Nuclear Instruments and Methods in Physics Research Section A: Accelerators, Spectrometers, Detectors and Associated Equipment Volume 507, Issues 1-2, 11 July 2003, Pages 323-326

[LBL09] *LOASIS Webpage*: http://loasis.lbl.gov (status: 2009/15/01)

[LCLS02] J. Arthur et al., *"Linac Coherent Light Source (LCLS) Conceptual Design Report"*, SLAC-R-593 April 2002 UC-414, April 2002

[LCLS04] R. Boyce, D.H. et a., *"Design Considerations for the LCLS RF Gun*, LCLS TN 04-4, April 2004

[Led07] S. Lederer et al., *"XPS studies of Cs2Te Photocathodes"*, Proc. FEL 2007, Novosibirsk, Russia

[Lee02] W.P. Leemans et al., Phys. Rev. Lett. 89, 174802 (2002)

[Lip03-1] D. Lipka et al., *"Measurement of the longitudinal phase space at PITZ"*, Proc. FEL 2003, Tsukuba, Ibaraki, Japan

[Lip03-2] D. Lipka et al., *"Measurement of the longitudinal phase space at the Photo Injector Test Facility DESY Zeuthen"*, Proc. DIPAC 2003, Mainz, Germany

[Lip04] Dirk Lipka, *"Untersuchungen zum longitudinalen Phasenraum an einem Photoinjektor für minimale Strahlemittanz"*, PhD thesis, Humboldt University Berlin, May 2004

[Lip05-1] D. Lipka, et al., *"Silica Aerogel Radiators for Bunch Length Measurements"*, Nuclear Instruments and Methods in Physics Research A 538 (2005) 597-607

[Lip05-2] Dirk Lipka, *"Spectrometer design for the SRF Gun"*, Note: SRFgun-BESSY-003-12-2004, 01/14/2005

[Loe06] F. Löhl et. al., *"Measurements of the transverse emittance at the FLASH injector at DESY"*, PHYSICAL REVIEW SPECIAL TOPICS - ACCELERATORS AND BEAMS 9, 092802 (2006)

[Los08] H. Loos et. al., , *"OBSERVATION OF COHERENT OPTICAL TRANSITION RADIATION IN THE LCLS LINAC"*, 30th International Free Electron Laser Conference, 2008, Gyeongju, Korea

[Mad70] J. Madey, J. Appl. Phys. 42, 1906, 1970

[Mar06] F. Marhauser et al., *"A High Average Power RF Photoinjector Gun Cavity Developed for the BESSY Soft X-Ray FEL"*, Proc. FEL 2006, Berlin, Germany

[MBI08] Max Born Institute *"Annual Report 2008"*

[Mil06] V. Miltchev, *"Investigations on the transverse phase space at a photo injector for minimized emittance"*, PhD Thesis 2006, Humboldt University

[Mur01] A. Murokh et al., *"Limitations on measuring a transverse profile of ultra-dense electron beams with scintillators"*, Proc. PAC 2001, Chicago, USA

[Opp07] A. Oppelt, *"RF measurements of guns and couplers"*, PITZ note 27.2.2007

[Pal05] L. Palumbo, *"Space Charge"*, CAS-Lecture 2005

[Park05] J. Park et al., *"Measurements of Transverse Emittance for RF Photocathode Gun at the PAL"*, Proc. of PAC 2005, Knoxville, Tennessee, USA

[PITZ08] F. Stephan et al., *"Detailed characterization of electron sources at PITZ yielding first demonstration of European XFEL beam quality"*, submitted to PRST-AB in 2008
to be published

[PSI08] *PSI Webpage*: http://fel.web.psi.ch/ (status: 2008/03/09)

[Rie05] S. Riemann, private communication (Nov. 2005)

[Rim07] S. Rimjaem et al., *"Status and Perspectives of the PITZ Facility Upgrade"*, Proc. FEL 2007, Novosibirsk, Russia, 2007

[Rim08] S. Rimjaem, private communication (Aug. 2008)

[Röh08] M. Röhrs, *"Investigation of the Phase Space Distribution of Electron Bunches at the FLASH-Linac Using a Transverse Deflecting Structure"*, PhD Thesis, Physics Department of Hamburg University, 2008

[Rön05] J. Rönsch, *"Selected studies of the longitudinal phase space at the photo injector test facility at DESY Zeuthen"*, Diploma thesis, 2004, Hamburg University

[Ros08] K. Rosbach, *"Reflektive Optik für Messungen des longitudinalen Phasenraums des niederenergetischen Elektronenstrahls"*,Diploma thesis, Humboldt-University, 2008

[Ros] K. Rosbach, private communication

[SSY] E.L. Saldin, E.A. Schneidmiller, M.V. Yurkov, *"Longitudinal Space Charge Driven Microbunching Instabilities in the TESLA Test Facility LINAC"*, Proc. FEL Conf. 2004

[SSY04] E.L. Saldin, E.A. Schneidmiller, M.V. Yurkov, Opt. Commun 235(2004)415

[Sch01] J.F. Schmerge et al., *"Transverse Emittance Measurements on an S-Band Photocathode RF Electron Gun"*, Proc. FEL Conf., Darmstadt, Germany, 2001

[Sch08] B. Schmidt et al., *"Longitudinal structure of electron bunches at the miccrometer scale from spectroscopy of coherent transition radiation"*, Proc. EPAC08, Genoa, Italy, 2008

[Sek07] J. Sekutowicz et al., *"Status of Nb-Pb superconducting RF-GUN cavities"*, PAC 2007 25-29 June 2007, Pages(s): 962-964

[Ser05] D. Sertore et al., *"Review of the Production Process of TTF and PITZ Photocathodes"*, PAC 2005. Proc. Page(s): 671 - 673

[Shi06] T. Shintake et al., *"First Lasing at SCSS"*, Proc. FEL 2006, BESSY, Berlin, Germany 2006

[Sp06] *"Sigmaphi Webpage*: http://www.sigmaphi.fr (status: 2006/10/03)

[Sta08] Lazar Staykov, *"Characterization of the Transverse Phase Space at the Photo-Injector Test Facility in Zeuthen"*, PhD Thesis Hambrg University, 2008

[Sta07] L. Staykov et al., *"Measurement of the Projected Normalized Transverse Emittance at PITZ"*, Proc. FEL 2007, Novosibirsk, Russia, 2007

[Ste07] B. Steffen, *"Electro-optic Methodes for Longitudinal Bunch diagnostic at FLASH"*, PhD thesis, hamburg University

[Spe07] R. Spesyvtsev, *"Transverse Beam Size Measurement Systems at Photo Injector Test Facility in Zeuthen"*, Diploma Thesis, Karazin Kharkiv National University, Ukraine, 2007

[Spe08] R. Spesyvtsev, *"A transverse Slice Emittance Measurement System Using Quadrupole Scan Technique and Streak Readout at PITZ"*, Proc. FEL2008, Gyeongiu, Korea

[TESLA01] R.Brinkmann et al., *"TESLA Technical Design report Part II The Accelerator"*, 2001

[Wil05] I. Will et al., *"The Upgrade Photocathode Laser of the TESLA Test Facility"*, NIM A 541 (2005) 467-477

[XFEL06] R. Abela et al., *"The European X-Ray Free-Electron Laser"*, Technical design report, DESY 2006-097, 2006

[XFEL07] *X-FEL Webpage*: http://xfel.desy.de/technical_information/electron_beam_parameter (status:2007/02/06)

[ZEM09] *ZEMAX Webpage*: http://www.zemax.com/

Acknowledgment

First of all, I would like to thank my advisor Prof. Dr. Jörg Roßbach for giving me the opportunity and the help to prepare this thesis and supporting my work. Further I thank you for the encouragement to visit other labs to broaden my mind.

My thanks go to Dr. Frank Stephan for the integration in the group, many useful hints and critical discussions.

My sincere thanks go to Dr. Jürgen Bähr for the support, the patience, encouragement, fruitful discussions, hints and support in case of problems.

Thanks to Dr. Dirk Lipka for introducing me to the measurement of longitudinal phase space at PITZ and always having time to answer my questions.

Many thanks to Dr. Mikhail Krasilnikov for the help to understand the beam dynamics and simulations.

Special thanks for proofreading this thesis to: Dr. Jürgen Bähr, Dr. Chase Boulware, Dr. Mikhail Krasilnikov, Dr. Frank Stephan. Thanks for the effort and all your comments.

I thank Dr. Sergiy Khodyachykh and Dr. Sakhorn Rimjaem for useful help and discussion on the dipole magnets. Kilian Rosbach for the work on the optics together and the fast help whenever it was necessary and Dr. Thorsten Kamps for useful discussions about the streak optics. Sakhorn and Kilian for not just shearing the office with me.

For the opportunity to visit LCLS I would like to thank Dr. Dave Dowell, Dr. Cecile Limbourg and Dr. Paul Emma. I am grateful for the effort for introducing the facility to me, many helpful discussions and introducing new ideas to me.

I also appreciate the helpful suggestions and criticism of Dr. Klaus Flöttmann and Dr. Sigfried Schreiber.

I thank all my colleagues at PITZ for the work together, the help in commissioning the components and many discussions, but also many colleagues from the technical groups contributed to the success of this work. Especially Hartmut Lüdecke spend a lot of effort to realize the streak optical system.

Nicht zuletzt möchte ich mich herzlichst bei meinen Freunden und meiner gesamten Familie für die Unterstützung, das Vertrauen und das Verständnis bedanken. Ganz besonder Dank gilt meinem Freund Dirk Schulenburg, meiner Mutter Gabriele Rönsch, meinem Bruder Marcus Rönsch, meiner Freundin Astrid Ende und meiner Patentante Monika Sobotta, dafür, daß Ihr immer für mich da wart, wenn es nötig war. Ohne Euch hätte ich es nicht geschafft.